Cell

Optogenetics-enabled discovery of integrated stress response modulators

Graphical abstract

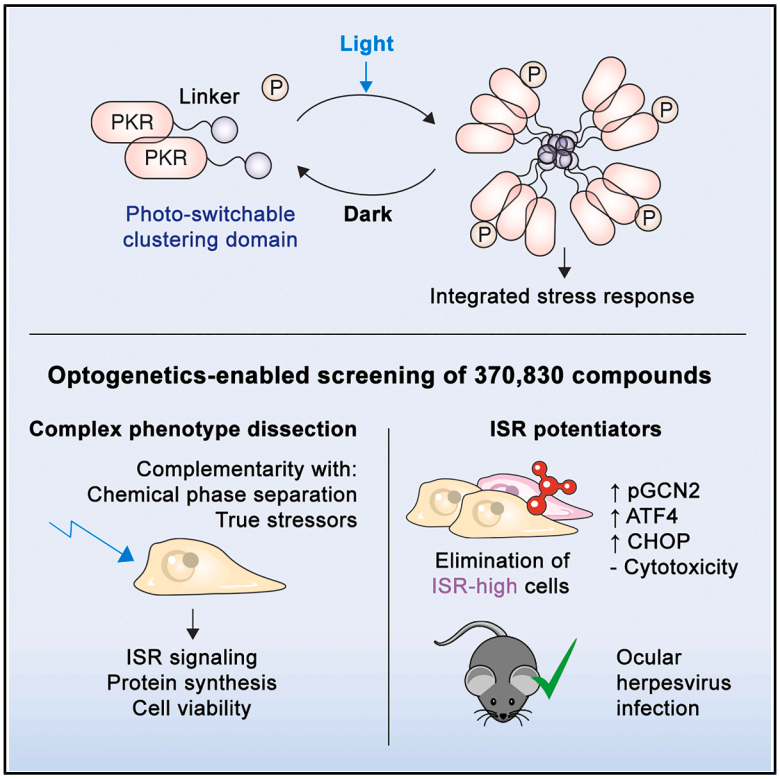

Highlights

- An optogenetics platform specifically induces the integrated stress response
- This platform enables a high-throughput screen of 370,830 compounds
- Identified compounds selectively eliminate ISR-high cells across diverse stressors
- These compounds demonstrate broad-spectrum antiviral activity *in vitro* and in mice

Authors

Felix Wong, Alicia Li, Satotaka Omori, ..., Hahn Kim, James J. Collins, Maxwell Z. Wilson

Correspondence

felix@integratedbiosciences.com (F.W.), jimjc@mit.edu (J.J.C.), max@integratedbiosciences.com (M.Z. W.)

In brief

An optogenetics-enabled drug screening platform facilitates targeting of the integrated stress response, leading to the identification of compounds that selectively potentiate ISR signaling across diverse stressors and exhibit broad-spectrum antiviral activity.

Wong et al., 2025, Cell *188*, 1–18
September 4, 2025
https://doi.org/10.1016/j.cell.2025.06.024

Cell

CellPress

Article

Optogenetics-enabled discovery of integrated stress response modulators

Felix Wong,[1,13,*] Alicia Li,[1,13] Satotaka Omori,[1,13] Ryan S. Lach,[1,13] Jose Nunez,[1] Yunke Ren,[1] Sean P. Brown,[1] Vipul Singhal,[1] Brent R. Lyda,[1] Taivan Batjargal,[1] Ethan Dickson,[2,3,4,5] Jose Roberto Rodrigues Reyes,[2,3,4,5] Juan Manual Uruena Vargas,[6] Shalaka Wahane,[7] Hahn Kim,[8,9] James J. Collins,[10,11,12,14,*] and Maxwell Z. Wilson[1,2,3,4,5,*]

[1]Integrated Biosciences, Redwood City, CA 94065, USA
[2]Center for BioEngineering, University of California, Santa Barbara, Santa Barbara, CA 93106, USA
[3]Biomolecular Science and Engineering Program, University of California, Santa Barbara, Santa Barbara, CA 93106, USA
[4]Department of Molecular, Cellular, and Developmental Biology, University of California, Santa Barbara, Santa Barbara, CA 93106, USA
[5]Neuroscience Research Institute, University of California, Santa Barbara, Santa Barbara, CA 93106, USA
[6]NSF BioPACIFIC Materials Innovation Platform, California NanoSystems Institute, University of California, Santa Barbara, Santa Barbara, CA 93106, USA
[7]Illumina Ventures, Foster City, CA 94404, USA
[8]Princeton University Small Molecule Screening Center, Princeton University, Princeton, NJ 08544, USA
[9]Department of Chemistry, Princeton University, Princeton, NJ 08544, USA
[10]Infectious Disease and Microbiome Program, Broad Institute of MIT and Harvard, Cambridge, MA 02142, USA
[11]Institute for Medical Engineering & Science and Department of Biological Engineering, Massachusetts Institute of Technology, Cambridge, MA 02139, USA
[12]Wyss Institute for Biologically Inspired Engineering, Harvard University, Boston, MA 02115, USA
[13]These authors contributed equally
[14]Lead contact
*Correspondence: felix@integratedbiosciences.com (F.W.), jimjc@mit.edu (J.J.C.), max@integratedbiosciences.com (M.Z.W.)
https://doi.org/10.1016/j.cell.2025.06.024

SUMMARY

The integrated stress response (ISR) is a conserved stress response that maintains homeostasis in eukaryotic cells. Modulating the ISR holds therapeutic potential for diseases including viral infection, cancer, and neurodegeneration, but few known compounds can do so without toxicity. Here, we present an optogenetic platform for the discovery of compounds that selectively modulate the ISR. Optogenetic clustering of PKR induces ISR-mediated cell death, enabling the high-throughput screening of 370,830 compounds. We identify compounds that potentiate cell death without cytotoxicity across diverse cell types and stressors. Mechanistic studies reveal that these compounds upregulate activating transcription factor 4 (ATF4), sensitizing cells to stress and apoptosis, and identify GCN2 as a molecular target. Additionally, these compounds exhibit antiviral activity, and one compound reduced viral titers in a mouse model of herpesvirus infection. Structure-activity and toxicology studies highlight opportunities to optimize therapeutic efficacy. This work demonstrates an optogenetic approach to drug discovery and introduces ISR potentiators with therapeutic potential.

INTRODUCTION

Cellular stress responses consist of diverse signaling cascades that regulate fundamental cellular processes, including proteostasis, metabolism, and cell division. As a central regulator of cellular homeostasis, the integrated stress response (ISR) is conserved across metazoan cells and responds to diverse stressors, including viral infection, endoplasmic reticulum (ER) stress, amino acid deprivation, oxidative stress, and heme deficiency.[1–3] These stressors are detected by four stress sensor kinases—HRI, PKR, PERK, and GCN2—that regulate translation through phosphorylation of eukaryotic translation initiation factor 2 subunit 1 (eIF2α), leading to downstream production of activating transcription factor 4 (ATF4) and other ISR components, including C/EBP homologous protein (CHOP) and protein phosphatase 1 regulatory subunit 15A (GADD34). Ultimately, the ISR results in either an adaptive response in which cells attenuate global protein synthesis to overcome the stressor or a terminal response in which apoptosis is induced (Figure 1A).

Dysregulation of the ISR and related stress responses, such as the unfolded protein response (UPR)[4]—in which PERK is also a sensor kinase—has been shown to contribute to the pathology of various diseases, including viral infection,[5,6] pulmonary fibrosis,[7,8] cognitive decline,[9,10] and prion disease.[11] Given the

Please cite this article in press as: Wong et al., Optogenetics-enabled discovery of integrated stress response modulators, Cell (2025), https://doi.org/10.1016/j.cell.2025.06.024

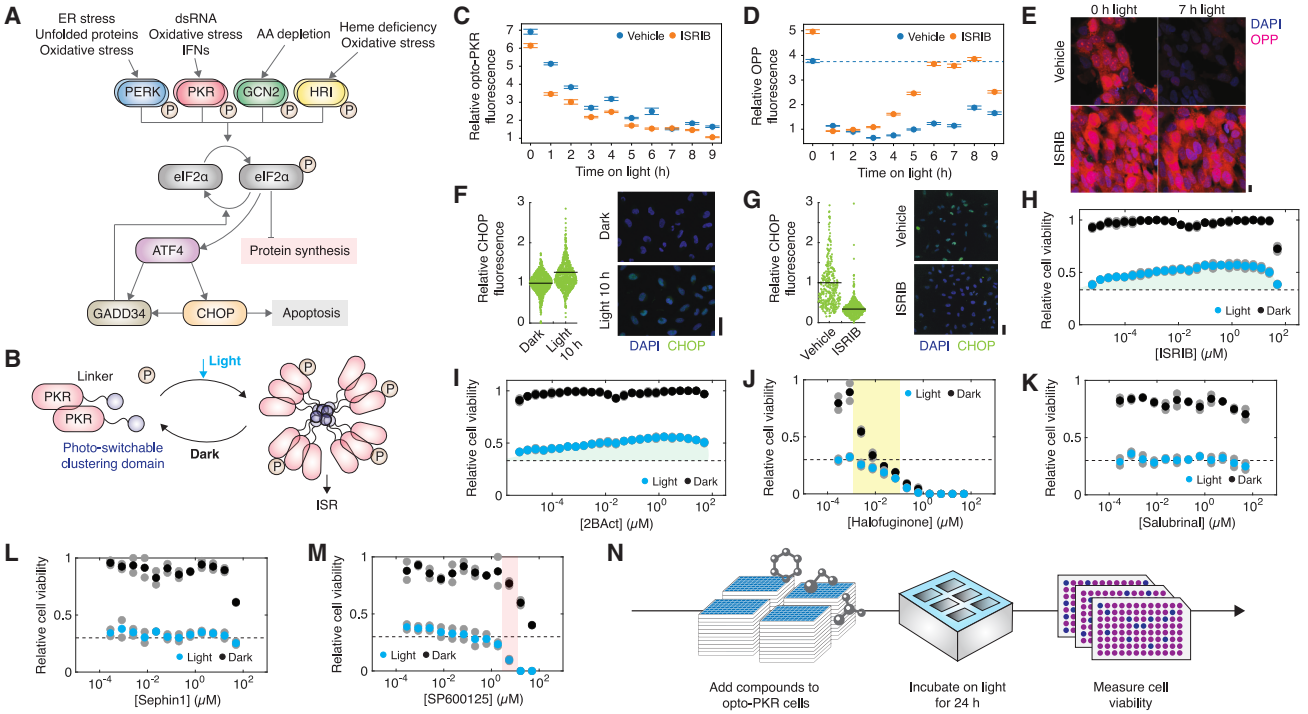

Figure 1. An optogenetics-based virtual stress platform for the chemical screening of ISR modulators

(A) Schematic of ISR signaling.

(B) Optogenetic clustering of PKR with the opto-PKR construct.

(C) Opto-PKR fluorescence intensity in single cells in response to optogenetic illumination. Cells were treated with either DMSO (0.5%) vehicle or 10 μM ISRIB at 0 h, and results are representative of two biological replicates. Points indicate mean values, and error bars indicate SEM. Cell counts for each time point: 1,683, 1,709, 1,383, 982, 616, 1,277, 1,160, 1,141, 965, and 1,274 for vehicle-treated 0–9 h; 1,635, 1,701, 1,702, 1,566, 1,826, 1,645, 1,399, 1,190, 1,556, and 1,424 for ISRIB-treated 0–9 h.

(D) Global protein synthesis, as measured by OPP fluorescence, in the same cells as in (C). Points indicate mean values, and error bars indicate SEM.

(E) Representative OPP staining images from the experiment shown in (D). Scale bar, 10 μm.

(F) (Left) Anti-CHOP fluorescence in single opto-PKR cells in response to optogenetic illumination. Results are representative of two biological replicates. Points indicate values for individual cells, and horizontal lines indicate mean values. Cell counts for each group, from left to right: 827 and 766. (Right) Representative anti-CHOP fluorescence images. Scale bar, 30 μm.

(G) (Left) Anti-CHOP fluorescence in single opto-PKR cells in response to compound treatment. Cells were treated with either DMSO (0.5%) vehicle or 10 μM ISRIB and incubated in light for 10 h, and results are representative of two biological replicates. Points indicate values for individual cells, and horizontal lines indicate mean values. Cell counts for each group, from left to right: 343 and 555. (Right) Representative anti-CHOP fluorescence images. Scale bar, 30 μm.

(H) Cell viability dose-response curves for opto-PKR cells treated with ISRIB for 24 h in light and in dark (cyan and black points, respectively). Colored points represent the means of two biological replicates (gray points). Values were normalized against those of DMSO (0.5%) vehicle-treated cells in dark, and the dashed line indicates the baseline cell viability value of vehicle-treated cells in light. Cell viability increases are highlighted in green.

(I–M) Similar to (H) but for other known ISR modulators. Decoupled cell viability decreases, in which cell viability decreases more in dark than in light for the same concentration of compound or vice-versa, are highlighted in yellow and red, respectively.

(N) Schematic of the screening approach.

See also Figure S1.

central role of the ISR in these diseases, previous efforts have aimed to identify and develop small-molecule modulators of the ISR as drug candidates. These efforts have resulted in the discovery and characterization of ISR activators, including guanabenz,[12,13] Sephin1,[14] PKR inhibitor C16,[15] and salubrinal,[16] as well as ISR inhibitors, including ISRIB[17] and 2BAct.[18] Nevertheless, the platforms used to discover these compounds have largely relied on screens against specific targets,[15] against specific disease presentations,[12] or using small-molecule stressors, such as tunicamycin,[16,17] that induce pleiotropic cytotoxic effects.[18] Furthermore, multiple ISR activators exhibit cytotoxic liabilities or adverse effects, and ISRIB and 2BAct are known to exhibit poor pharmacokinetic properties and cardiovascular toxicity, respectively.[19,20] Discovering ISR-modulating compounds without such limitations would facilitate the development of drug candidates capable of targeting diseases through their effects on cellular proteostasis.

Concurrent with these discovery efforts, advances in synthetic biology have enabled precise control of cellular stress responses,[21,22] facilitating phenotypic drug discovery approaches. We recently engineered an optogenetic system that triggers PKR phase separation upon exposure to blue light, mimicking PKR's natural activation and inducing the ISR without the off-pathway cytotoxicity associated with small-molecule stressors.[22] Given

the ability to activate the ISR in the absence of damage, we reasoned that our optogenetic tool could provide an efficient and on-pathway approach to detecting the effects of small-molecule modulators of the ISR. This screening approach would be phenotypic by design, enabling the rapid identification of compounds with potentially diverse mechanisms of action but necessitating downstream target deconvolution using complementary methods. Here, we tested this hypothesis by performing the largest optogenetic screen to date,[23] in which the ISR-modulating effect of each of 370,830 small molecules was quantified by co-treating engineered cells with blue (450 nm) light and compound.

RESULTS

Optogenetics-based analysis of ISR-modifying compounds

We first characterized a synthetic gene circuit enabling light-inducible clustering of PKR in the presence of known small-molecule modulators of the ISR. We have previously shown that physiological activation of PKR depends on its oligomerization[24–26] and can be mimicked by replacing PKR's double-stranded RNA (dsRNA) binding domains (dRBM1 and dRBM2) with Cry2Olig (E490G; Figure 1B). We thus transduced human H4 neuroglioma cells, chosen for their relative ease of expansion and neural epithelial origin, with a citrine-tagged Cry2Olig-PKR (hereafter referred to as opto-PKR), and isolated a pseudo-clonal population to reduce heterogeneity in the cellular response. We previously found that, in response to non-phototoxic levels of blue light, opto-PKR cells exhibited cytoplasmic condensates, elevated levels of phosphorylated eIF2α (peIF2α), and decreased puromycin incorporation in nascent peptides on a timescale of 1 h.[22] We reasoned that capturing the temporal dynamics of ISR activation would provide a precise quantitative baseline for assessing pharmacologic modulators. Accordingly, here we subjected opto-PKR cells to blue light for up to 10 h and quantified both the incorporation of o-propargyl-puromycin (OPP)[27]—a puromycin analog detectable using click chemistry—into nascent peptides and the expression of CHOP with immunofluorescence. Consistent with previous work,[22] we observed receptor-level negative feedback wherein opto-PKR fluorescence intensity decayed with activation time (Figure 1C). Compared with control opto-PKR cells maintained in the dark, cells illuminated for 3 h showed an average decrease of up to 4-fold in OPP levels (Figures 1D and 1E) and moderately (∼20%) increased levels of CHOP after 10 h of light (Figures 1F and 1G).

Upregulation of CHOP is known to induce a terminal apoptotic stress response,[1–3,28,29] and hence we hypothesized that longer-duration (>10 h) activation of opto-PKR would result in ISR-associated cell death. Consistent with this hypothesis, we found a substantial decrease in cell viability as measured using resazurin (a metabolic activity indicator), with ∼60% cell death occurring after 24 h of light—a time point chosen to integrate the effects of ISR signaling across earlier time points while providing a high dynamic range of cell viability decreases (Figures S1A and S1B). In the presence of light, ISRIB treatment increased cell viability, elevated OPP levels, and reduced CHOP levels, consistent with the hypothesis that extended ISR activation contributes to cell death and that pleiotropic, off-pathway effects of light exposure alone do not obfuscate detection of ISR modulation (Figures 1D–1H). ISRIB treatment at high concentrations (∼50 μM) did not completely rescue cells, whereas the effects of treatment at low concentrations (∼10 pM) could still be resolved. Although light pulsing experiments suggest that selective activation of the ISR occurs with minimal light dosing (Figure S1C), blue light phototoxicity or ISRIB's limiting cytotoxicity at high concentrations may contribute to ISR-independent decreases in cell viability. Nevertheless, experimental replicates suggest that our measurements of cell viability are robust, with typical coefficient of variation values < 10%, and can identify other ISR-specific inhibitors, including 2BAct (Figures 1I and S1B).

Although activators, including halofuginone, salubrinal, and Sephin1, have been shown to activate the ISR, treatment with these compounds did not substantially alter cell viability in light relative to dark (Figures 1J–1L and S1D). An exception is halofuginone, which exhibited selective cytotoxicity against cells in dark at concentrations of ∼100 nM: this effect was abrogated in cells pretreated with light for 24 h, suggesting that adaptive ISR activation might protect cells from treatment (Figure S1E). Overall, our observations indicate that the ISR-activating effects of these compounds are not additive with opto-PKR stimulation in the terminal cell fate decision. In fact, all compounds were cytotoxic to cells kept in the dark at higher concentrations, and some of these compounds may act on pathways other than the ISR, consistent with the results for salubrinal presented further below. Additionally, SP600125, an ATP-competitive inhibitor of c-Jun N-terminal kinase (JNK),[30] selectively decreased cell viability in light without being acutely cytotoxic to control cells at a dose of 12.5 μM, suggesting that it may further activate the ISR at a narrow range of concentrations (Figure 1M). Taken together, our results suggest that an optogenetic approach, using opto-PKR cells co-treated with light and a test compound, could enable screening for small-molecule modulators of the ISR by assessing cell viability after 24 h (Figures 1N and S1A).

Optogenetic screening of 370,830 compounds reveals putative ISR modulators

We assembled a small-molecule library of 370,830 compounds that, relative to known chemical modulators of the ISR, samples an expanded chemical space, as visualized through t-distributed stochastic neighborhood embedding (t-SNE) on the Morgan fingerprints of each chemical structure (Figure 2A; Data S1). This library included the Pharmakon library of clinically evaluated drugs, natural products, metabolites, and other smaller, previously described libraries.[31–33] We screened this library of compounds at a final concentration of 10 μM—a concentration informed by prior compound screens[32–34]—by scaling up the high-throughput approach outlined in Figure 1N and measuring the viability of opto-PKR cells after 24 h of light in the presence of each compound (Figure 2B).

As a counterscreen for cytotoxicity, we measured the viability of IMR-90 human lung fibroblasts—chosen to represent a non-cancerous cell type—after 3 days of compound treatment at a final concentration of 10 μM in ambient lighting (Figure 2C). As a starting point for defining putative ISR-modifying compounds, we shortlisted compounds for which treatment resulted in a

Please cite this article in press as: Wong et al., Optogenetics-enabled discovery of integrated stress response modulators, Cell (2025), https://doi.org/10.1016/j.cell.2025.06.024

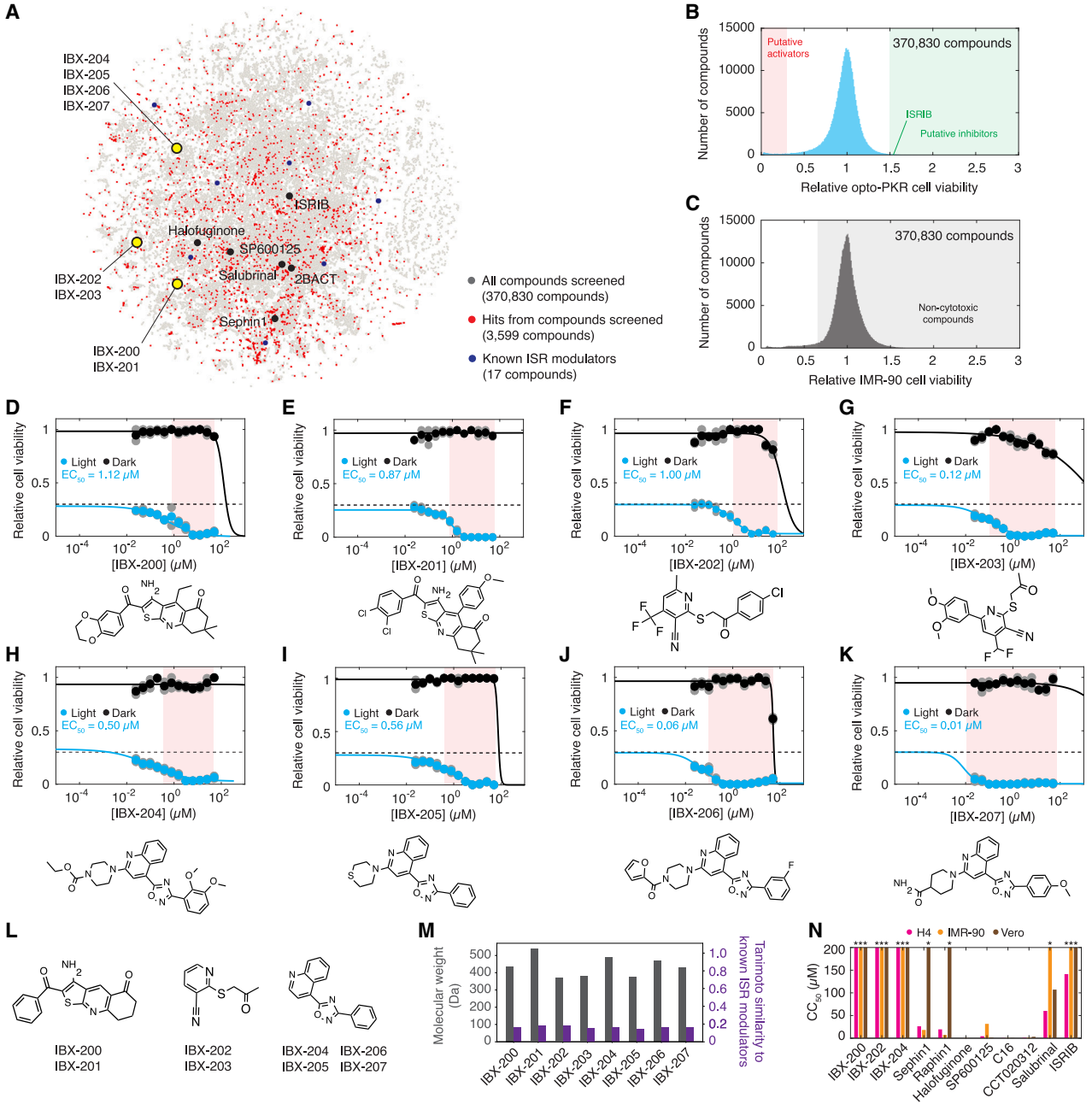

Figure 2. Optogenetics-driven discovery of compounds that selectively kill ISR-high cells

(A) t-SNE plot of the screening library of 370,830 compounds relative to known ISR-modulating compounds.

(B and C) Histograms of relative cell viability values obtained from screening the 370,830-compound library shown in (A) at a final concentration of 10 μM.

(D–K) Cell viability dose-response curves for opto-PKR cells treated with IBX-200 to IBX-207 for 24 h in light and in dark (cyan and black points, respectively). Colored points represent the means of two biological replicates (gray points). Values were normalized against those of DMSO (0.5%) vehicle-treated cells in dark, and the dashed line indicates the baseline cell viability value of vehicle-treated cells in light. Decoupled cell viability decreases are highlighted in red.

(L) Chemical scaffolds represented by IBX-200 to IBX-207.

(M) Molecular weights and Tanimoto similarity of IBX-200 to IBX-207 with respect to the known ISR modulators shown in (A).

(N) Half-maximal cytotoxic concentration (CC_{50}) values of IBX-200, IBX-202, IBX-204, and other ISR-modulating compounds against different cell types. Asterisks indicate values >200 μM, and values shown are from one biological replicate.

See also Figures S2 and S6.

relative opto-PKR cell viability < 0.3 or >1.5 and a relative IMR-90 cell viability > 0.7, leading to a set of 3,599 compounds with putative ISR-activating (relative opto-PKR cell viability < 0.3) or ISR-inhibiting (relative opto-PKR cell viability > 1.5) activity. We chose these thresholds to prioritize selective and non-cytotoxic compounds, given that typical coefficient of variation values in our cell viability measurements were <10%, and ISRIB, 2BAct, and SP600125 treatment at ~10 μM resulted in similar effect sizes (Figures 1H, 1I, 1M, and S1B). Repeating the experiment measuring cell viability in duplicate for each of the shortlisted compounds, we retained 306 compounds for which both replicates validated for further study.

Small molecules selectively increase cell death

To identify compounds with selective ISR-modulating activity, we compared cell viability dose-response experiments in light versus dark at concentrations ranging from 0.2 to 50 μM. Of the shortlisted compounds, we found that compounds that increased the viability of opto-PKR cells in light did so only at limited concentration ranges (~1–10 μM). However, 85 compounds (0.02% of all compounds screened) potently and selectively decreased the viability of opto-PKR cells in light, with selectivity windows—the ratio of the half-maximal effective concentration (EC_{50}) value in dark to that in light—greater than 10 (Data S1). Among these compounds, we focused on eight with the highest selectivity windows (Figures 2D–2K). These compounds—herein renamed from IBX-200 to IBX-207—were not acutely cytotoxic to opto-PKR cells in dark at concentrations up to 50 μM but exhibited EC_{50} values ~0.1 to ~1 μM in light, indicating strong selectivity. Notably, these compounds have not been previously characterized and share three distinct chemical scaffolds (Figure 2L). All eight compounds were Lipinski-conforming,[35] exhibited molecular weights between 370 and 550 Da, had calculated topological polar surface area (TPSA) values < 120 $Å^2$ and often <90 $Å^2$—suggesting that they likely penetrate the blood-brain barrier[36]—and displayed no pan-assay interference substructures (PAINS) or Brenk substructures,[37,38] which are associated with unfavorable pharmacokinetic properties (Figure 2M; Table S1). Furthermore, their Tanimoto similarity values were <0.2 with respect to any known ISR-modifying compound. Thus, these compounds represent chemical series of putative ISR-modulating small molecules with favorable drug-like properties.

Building on our characterization of these compounds in opto-PKR cells treated in dark, we investigated the cytotoxicity of these compounds against different cell types, including wild-type H4, IMR-90, and Vero (African green monkey kidney epithelial) cells. We selected one compound to represent each structural class—IBX-200, IBX-202, and IBX-204—and found that, across all three cell types, each compound exhibited half-maximal cytotoxic concentration (CC_{50}) values > 200 μM after 3 days of treatment, supporting that the discovered compounds are largely not cytotoxic (Figures 2N and S2A). In contrast, known ISR activators, including Sephin1, Raphin1, halofuginone, SP600125, C16, and CCT020312, exhibited CC_{50} values largely ≤50 μM, and often in the single-digit micromolar range, across most or all tested cell types, indicating that these compounds are cytotoxic. Salubrinal was also modestly cytotoxic to wild-type H4 and Vero cells, with CC_{50} values of ~70 and ~100 μM, respectively. Because compounds IBX-200 through IBX-207 are selective against opto-PKR cells in light and do not exhibit collateral cytotoxicity, to distinguish these compounds from ISR activators that have tonic activity, we hypothesized that they comprise a unique modality of ISR-modifying compounds—ISR potentiators.

Phenotypic characterization of compounds

To investigate whether these compounds indeed increase ISR activity in the presence of diverse ISR-related stressors—and not only in response to opto-PKR-induced activity—we first co-treated cells with compounds and ISR-activating poisons. Thapsigargin and sodium arsenite have been used to induce ER stress and oxidative stress, respectively: thapsigargin interferes with calcium homeostasis to deplete ER calcium and activate PERK, whereas sodium arsenite activates HRI.[17,39–42] We again focused on one compound representing each structural class—IBX-200, IBX-202, and IBX-204—and performed checkerboard cell viability measurements of wild-type H4 cells (not containing opto-PKR) co-treated with stressor for 24 h. We found that the compounds synergistically induced cell death with thapsigargin and sodium arsenite across a range of compound and stressor concentrations (Figures 3A–3F). Consistent with the observed cell death being ISR-associated, treatment with 20 μM ISRIB or 5 mM n-acetylcysteine, an antioxidant, largely rescued cells from thapsigargin and sodium arsenite, respectively. Notably, typical concentrations of IBX-200, IBX-202, and IBX-204, at which cell viability substantially decreased in the true stressor experiments (~10 μM), were higher than corresponding concentrations for opto-PKR cells (≤1 μM; Figures 2D–2K), suggesting that the ISR is more potently activated in opto-PKR cells. Salubrinal also potentiated thapsigargin and sodium arsenite against wild-type H4 cells, consistent with its known mechanism of ISR activation[16]; yet, underscoring salubrinal's single-agent cytotoxicity, we found cell viability decreases of ~20% at the lowest concentration tested (6.25 μM) in the absence of any stressor (Figure S2A), consistent with our dose-response experiments for opto-PKR cells in dark (Figure 1K). Thus, salubrinal treatment did not decrease cell viability selectively in these stressed cells.

Although our experiments have focused on H4 neuroglioma cells, the ISR is conserved across metazoan cells, and we anticipated that synergy with ISR-activating poisons would be recapitulated in diverse cell types and species. Consistent with this hypothesis, we found that our compounds were synergistic with thapsigargin against Vero cells (Figures S2B and S2C). Furthermore, in addition to optogenetically, clustering of PKR may be induced chemically.[43] To this end, we transduced H4 cells with a chemically inducible PKR construct, mCherry-DmrB-PKR, using an inducible homodimer system (hereafter referred to as chem-PKR cells; Figure 3G). Treating chem-PKR cells with B/B homodimerizer to induce PKR activation, we observed on-pathway increases in peIF2α, ATF4, and CHOP levels, as measured by immunofluorescence staining (Figures S2D–S2F). Consistent with increased ISR activation leading to cell death in chem-PKR cells, we measured decreases in cell viability after treatment with B/B homodimerizer for 24 h, and B/B homodimerizer treatment

Please cite this article in press as: Wong et al., Optogenetics-enabled discovery of integrated stress response modulators, Cell (2025), https://doi.org/10.1016/j.cell.2025.06.024

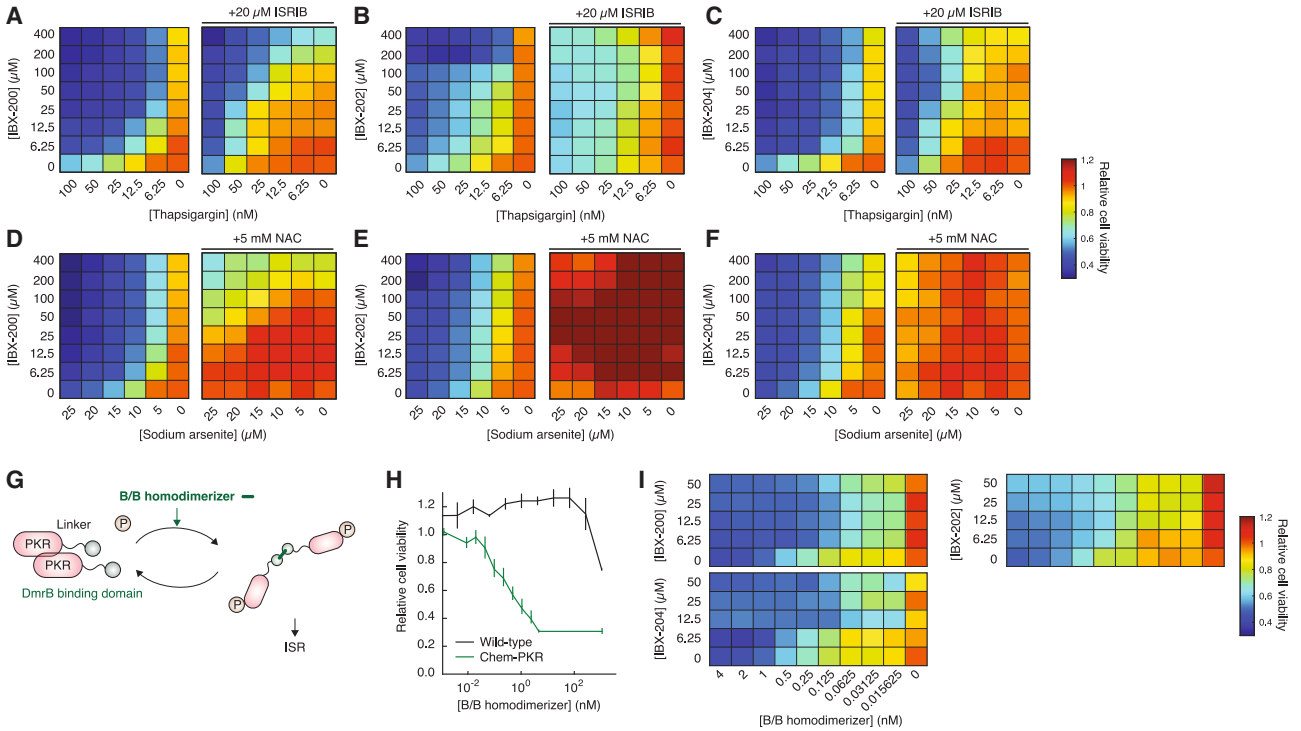

Figure 3. True stressor and chemically inducible PKR potentiation experiments

(A–C) Checkerboard cell viability measurements of wild-type H4 cells treated with IBX-200 (A), IBX-202 (B), and IBX-204 (C) in combination with thapsigargin for induction of ER stress. Values are normalized against those corresponding to vehicle treatment only (bottom-right value of each checkerboard). Results shown are representative of two biological replicates.

(D–F) Similar to (A)–(C) but for cells treated with IBX-200 (D), IBX-202 (E), and IBX-204 (F) in combination with sodium arsenite for induction of oxidative stress.

(G) Chemical dimerization of PKR with the chem-PKR construct.

(H) Cell viability measurements of wild-type and chem-PKR H4 cells treated with B/B homodimerizer. Values were normalized against those of DMSO (0.5%) vehicle-treated chem-PKR cells, and error bars show the range of values obtained from two biological replicates.

(I) Checkerboard cell viability measurements of chem-PKR H4 cells treated with IBX-200, IBX-202, and IBX-204 in combination with B/B heterodimerizer for ISR induction. Values are normalized against those corresponding to vehicle treatment only (bottom-right value of each checkerboard). Results shown are representative of two biological replicates.

See also Figure S2.

by itself was non-cytotoxic against wild-type H4 cells at concentrations below 500 nM (Figure 3H). Performing checkerboard cell viability assays as above with B/B homodimerizer combined with IBX-200, IBX-202, or IBX-204, we found that the compounds potentiated cell death across a range of homodimerizer and compound concentrations (Figure 3I). Altogether, these findings indicate that our discovered compounds selectively enhance cell death across different cell types and modes of ISR induction, including optogenetic clustering of PKR, chemical dimerization of PKR, and thapsigargin and sodium arsenite treatment.

Phenotypic mechanism of action

As IBX-200, IBX-202, and IBX-204 enhance cell death across different stressors, we aimed to further elucidate their mechanisms of action. We treated wild-type H4 cells with each of these compounds at 100 μM, a concentration chosen to exceed the levels required for observing cell-death-enhancing effects to result in ISR-related changes without additional stressors. Immunofluorescence imaging indicated that treatment with each compound increased ATF4 and, to a lesser extent, CHOP (Figures 4A–4C). Cells treated with IBX-200 and IBX-202 exhibited ~2- to 3-fold increases in anti-ATF4 fluorescence—larger than that resulting from treatment with salubrinal—and ~2-fold increases in anti-CHOP fluorescence (Figures 4A–4C). In contrast, cells treated with IBX-204 displayed less substantial fluorescence increases for both ATF4 and CHOP. These observations were qualitatively similar for opto-PKR H4 cells incubated in dark; additionally, we found that these observations were robust to varying the treatment time and concentration, as qualitatively similar changes in ATF4 and CHOP fluorescence occurred after treatment with these compounds at 10 or 100 μM for times between 1 and 30 h (Figures S3A and S3D). Additional immunofluorescence experiments labeling peIF2α and OPP in treated wild-type H4 cells indicate that IBX-200 and IBX-202 modulate these factors to a lesser extent than their effects on ATF4 and CHOP, with <1.6-fold increases in relative mean fluorescence values after 24 h (Figure S3B). The increased levels of peIF2α and OPP suggest that IBX-200 and IBX-202 may strengthen endogenous negative feedback from high ATF4 levels on the ISR and induce ATF4-associated increases in

Please cite this article in press as: Wong et al., Optogenetics-enabled discovery of integrated stress response modulators, Cell (2025), https://doi.org/10.1016/j.cell.2025.06.024

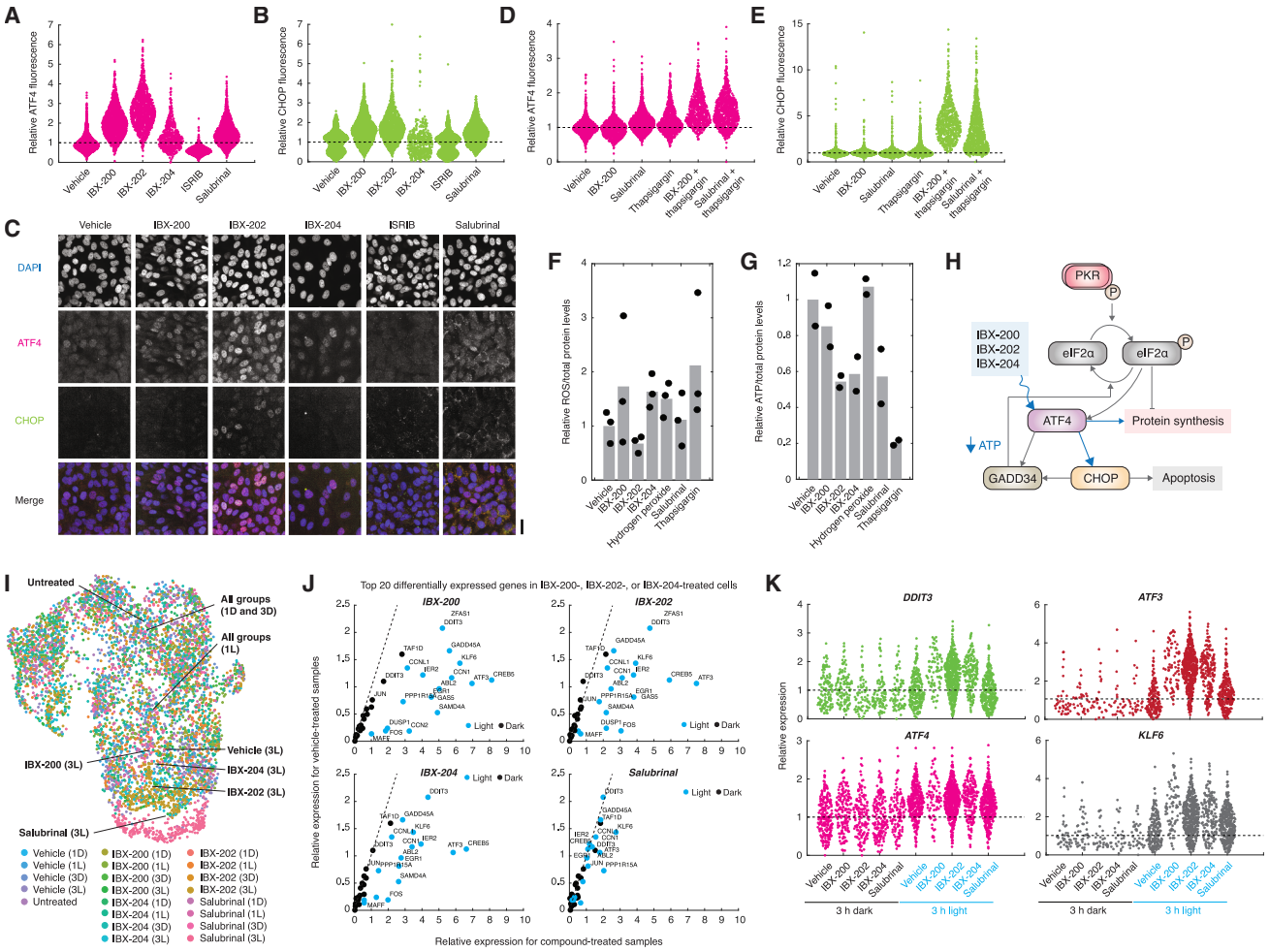

Figure 4. Phenotypic effects of compounds

(A and B) Anti-ATF4 and CHOP fluorescence in the same single wild-type H4 cells in response to compound treatment. Cells were treated with either DMSO (0.5%) vehicle or 100 μM of each indicated compound for 24 h, and results are representative of two biological replicates. Points indicate values for individual cells, and values are normalized to the mean value of cells treated with vehicle (dashed lines). Cell counts for each group, from left to right: 1,513, 1,535, 1,215, 549, 1,568, and 1,425.

(C) Representative anti-ATF4 and CHOP fluorescence images from the experiment shown in (A) and (B). Scale bar, 20 μm.

(D and E) Similar to (A) and (B) but for single opto-PKR cells treated with 10 μM of IBX-200 or salubrinal and 25 nM thapsigargin and incubated for 24 h in dark. Cell counts for each group, from left to right: 1,146, 820, 1,063, 831, 693, and 915.

(F and G) Relative ROS levels (F) and ATP levels (G) in bulk culture wild-type H4 cells treated with either DMSO (1%) vehicle or 100 μM of each indicated compound, with the exception of 50 nM of thapsigargin, for 24 h. Data are from three (F) or two (G) biological replicates (black points), and bars shown mean values.

(H) Proposed phenotypic mechanism of action of IBX-200, IBX-202, and IBX-204, with relevant components highlighted by blue arrows.

(I) Uniform manifold approximation and projection (UMAP) cellular transcriptomics plots for untreated opto-PKR cells and opto-PKR cells treated with DMSO vehicle, IBX-200, IBX-202, IBX-204, or salubrinal (10 μM of each compound) in the presence of light for 1 and 3 h (1L and 3L, respectively) and in dark for 1 and 3 h (1D and 3D, respectively). Pointers indicate centroids of all UMAP points for each population.

(J) Plots of relative mean expression for the top 20 differentially expressed genes in IBX-200-, IBX-202-, and IBX-204-treated cells for 3 h in light and 3 h in dark relative to vehicle-treated cells. For comparison, the same genes in salubrinal-treated cells are shown. Dashed lines indicate no relative enrichment compared with cells kept in dark.

(K) Plots of relative expression in single cells for four ISR-related genes in compound-treated cells for 3 h in light relative to 3 h in dark. Values are normalized to the mean value of cells treated with vehicle for 3 h in dark (dashed lines). Cell counts for each group, from left to right: *DDIT3*, 115, 111, 67, 88, 77, 232, 79, 458, 178, and 296; ATF4, 217, 158, 142, 167, 119, 317, 80, 497, 201, and 398; *ATF3*, 38, 33, 26, 26, 27, 161, 79, 493, 195, and 265; *KLF6*, 38, 40, 30, 29, 38, 187, 78, 435, 158, and 341.

See also Figure S3.

Please cite this article in press as: Wong et al., Optogenetics-enabled discovery of integrated stress response modulators, Cell (2025), https://doi.org/10.1016/j.cell.2025.06.024

protein production, consistent with prior work.[44] In contrast, IBX-204 treatment decreased mean peIF2α and OPP fluorescence after 24 h by 1.5- and ~3-fold, respectively, suggesting that it might act on ISR-related feedback differently than do IBX-200 and IBX-202 (Figure S3C).

Building on these results, we hypothesized that alterations in ATF4 homeostasis are associated with increased sensitivity to ISR stress. Focusing on IBX-200, we repeated our immunofluorescence experiments and treated cells with low but synergistic concentrations of IBX-200 (10 μM) and thapsigargin (25 nM) for 24 h. We found that anti-ATF4 and anti-CHOP fluorescence was only modestly (~10%) increased by treatment with either compound alone but, on average, increased >2-fold in the presence of both compounds, similar to treatment with the combination of salubrinal and thapsigargin (Figures 4D and 4E). These observations indicate that, in IBX-200-treated cells, increased expression of ATF4 is associated with increased cell death in the presence of a stressor. Prior work has shown that forced expression of ATF4 increases protein synthesis, causing oxidative stress and ATP depletion in mouse embryo fibroblasts (MEFs).[44] We additionally measured reactive oxygen species (ROS) and ATP levels in cells treated with each of IBX-200, IBX-202, and IBX-204 (Figures 4F and 4G). Dichlorofluoroscein staining suggested that wild-type H4 cells treated with IBX-200 and IBX-204 for 24 h exhibited increases in ROS levels; cells treated with IBX-202, in contrast, did not—similar to treatment with salubrinal. In contrast, quantification of ATP levels indicated that ATP was decreased in cells treated with IBX-200, IBX-202, and IBX-204, similar to treatment with salubrinal. Despite potential compound-specific variation in altering cellular phenotypes, these findings suggest that IBX-200, IBX-202, and IBX-204 increase ATF4 and CHOP expression, resulting in ATF4- and CHOP-mediated sensitivity to thapsigargin stress and ATP depletion as a hallmark of high ATF4 expression (Figure 4H).

To further investigate compound-induced phenotypes, we performed a single-cell transcriptomic analysis of opto-PKR cells treated with each of IBX-200, IBX-202, and IBX-204 at 10 μM in light and in dark (Figures 4I and S3E). Distinct alterations to population-averaged transcriptomes occurred in response to both light and compound treatment (Figure 4I), with *DDIT3* (CHOP) showing substantial (>2-fold) enrichment relative to DMSO in compound-treated cells in light—in contrast to salubrinal, for which no similar enrichment was observed (Figure 4J). Additionally, salubrinal-treated cells kept in dark overexpressed *SLC2A1*, *SLC7A5*, *SLC3A2*, *HERPUD1*, and *CYP1B1* (Figure S3E), whereas IBX-200-, IBX-202- and IBX-204-treated cells did not, consistent with salubrinal exhibiting a different mechanism of action from these compounds. Focusing on ISR-adjacent genes, we found that IBX-200-, IBX-202-, and IBX-204-treated cells in light also overexpressed *ATF4, ATF3*, and *KLF6*.[45] Consistent with the selectivity of these compounds against stressed cells, the compounds had little discernable effect on these transcripts in cells kept in dark (Figure 4K). Overall, these findings indicate that our compounds upregulate *ATF4* and *DDIT3* (CHOP), along with those of several ISR-adjacent genes, in an ISR-pathway-specific manner.

Molecular mechanism of action

Given that the compounds upregulate ATF4 and CHOP (Figures 4A–4C), we first examined upstream components of the ISR to identify potential binding targets. We found that IBX-200 and IBX-204 (but not IBX-202) selectively decreased GCN2's kinase activity, with half-maximal inhibitory concentration (IC_{50}) values ~50 μM (Figures 5A and S4A–S4D). IBX-202 did not reduce GCN2 kinase activity, and cellular thermal shift assays (CETSAs) identified no binding target for IBX-202 (Figure S4E). This contrasted with IBX-200 and IBX-204, for which two proteins (GPX4 and FECH) appeared as additional shared potential binding targets. However, follow-up assays—including differential scanning fluorimetry, enzymatic inhibition, and cell viability assays—indicated that these proteins were not involved in ISR potentiation (Figures S4F–S4H; STAR Methods). Further studies revealed that IBX-202 chemically converts into an IBX-200-family compound that may act on GCN2 similarly to IBX-200 (Figure S4I). We therefore investigated GCN2 to study a plausible mechanism of action of all the compounds.

Human GCN2 is a complex, ~190-kDa protein with multiple functional pseudokinase and kinase domains.[46–48] GCN2 kinase domain inhibitors, including GCN2iB and GCN2-IN-1, have previously been characterized.[49–51] Nevertheless, we found that GCN2iB and GCN2-IN-1 do not increase cell death in opto-PKR cells in the presence of light; neither do these compounds increase cell death in wild-type H4 cells in the presence of thapsigargin and sodium arsenite (Figures S4J and S4K). These divergent phenotypic results suggested that our compounds might act differently on GCN2 than do GCN2iB and GCN2-IN-1. We therefore performed surface plasmon resonance (SPR) measurements to further study this interaction, which indicated that IBX-200 and IBX-204 selectively bound GCN2 with K_d values of 25.2 and 3.2 μM, respectively (Figures 5B and S4L). In contrast, IBX-202 did not bind GCN2, and GCN2iB bound GCN2 with a lower K_d value of 1.7 μM. These findings were qualitatively consistent with our kinase activity measurements in that they indicated binding; nevertheless, the lower K_d values of IBX-200 and IBX-204 relative to their kinase inhibition IC_{50} values suggested that kinase inhibition might be auxiliary to compound binding. Additional molecular docking simulations using AutoDock Vina and AlphaFold3's prediction of GCN2's tertiary structure[52,53] suggested the specific hypothesis that binding occurs proximal to an activating C-lobe subdomain—resulting in phosphorylation at Thr899, a canonical active form of GCN2[54–56] (Figure 5C; STAR Methods).

As IBX-200 and IBX-204 might activate GCN2 to confer their phenotypic effects on stressed cells, we engineered a knockout (KO) of *EIF2AK4* (GCN2) in opto-PKR H4 cells for cell viability assays. We first validated decreases in GCN2 protein levels, finding an ~70% decrease in GCN2 levels in these cells (Figure 5D). Repeating our experiments using optogenetic activation of PKR, we found that cell viability was increased after treatment with IBX-200, IBX-202, and IBX-204 in GCN2-KO cells compared with cells bearing opto-PKR only (Figure 5E). These cells exhibited an ~20%–100% rescue of cell death across a range of compound concentrations. Intriguingly, although IBX-202 was not evidenced to target GCN2 in our experiments, decreasing GCN2 levels partially rescued opto-PKR cells from

Please cite this article in press as: Wong et al., Optogenetics-enabled discovery of integrated stress response modulators, Cell (2025), https://doi.org/10.1016/j.cell.2025.06.024

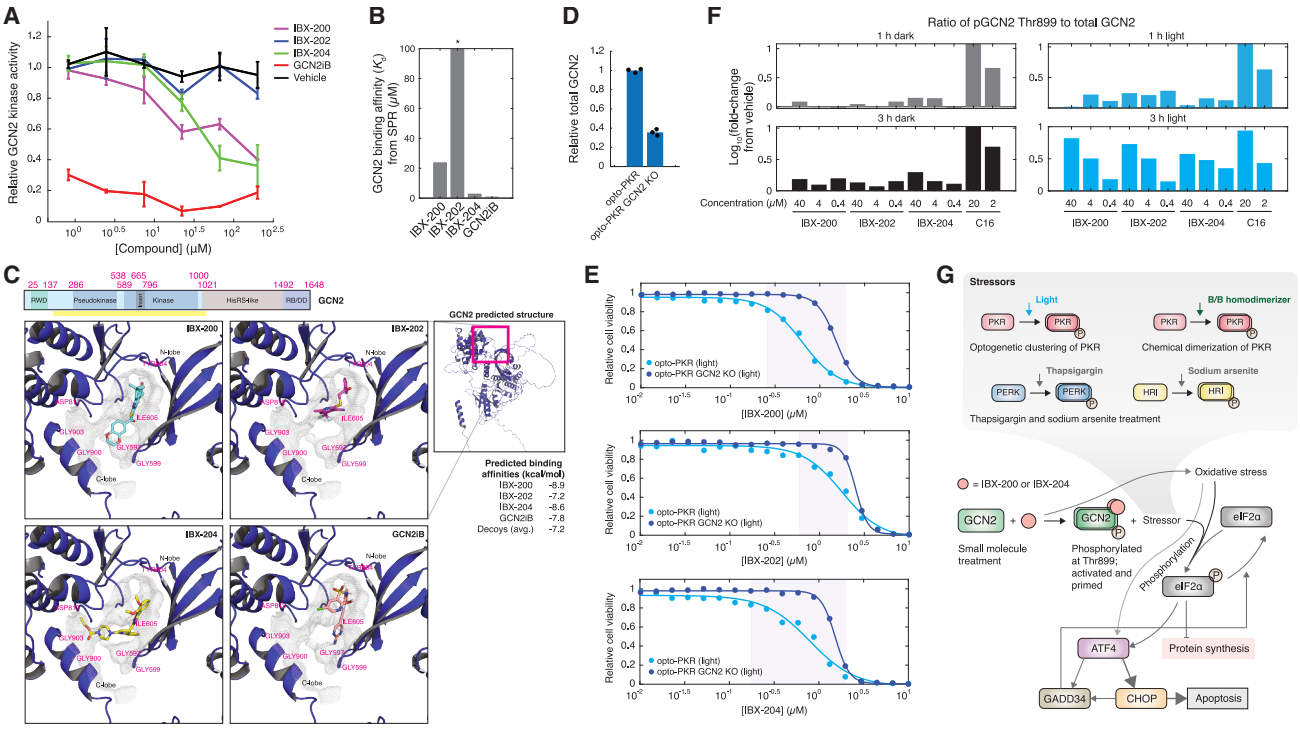

Figure 5. GCN2 targeting of compounds and proposed mechanism of action

(A) GCN2 kinase activity of reconstituted GCN2 treated with each of the indicated compounds at the indicated final concentrations. Shown are the mean of two biological replicates, and error bars indicate the full range of values measured.

(B) Binding affinity (K_d) values against GCN2 for each of the indicated compounds, as measured by SPR. Values are inferred from curve fitting to one biological replicate. Asterisks indicate a degenerate response curve (Figure S4L).

(C) Molecular docking poses for each of the indicated compounds and the predicted tertiary structure of GCN2. A schematic of various GCN2 domains is shown at top. Binding affinities were calculated from AutoDock Vina (see STAR Methods), and compounds are shown in different colors.

(D) GCN2 protein levels in baseline (opto-PKR) and GCN2-KO cells. Bars indicate the mean of three biological replicates, and error bars indicate the full range of values measured.

(E) Cell viability dose-response curves for opto-PKR and opto-PKR GCN2-KO cells treated with IBX-200, IBX-202, and IBX-204 for 24 h in light (cyan and blue points, respectively). Points indicate the means of two biological replicates. Values were normalized against those of DMSO (0.5%) vehicle-treated opto-PKR cells in light. Differences in cell viability are highlighted in purple.

(F) Ratios of pGCN2 Thr899 to total GCN2 levels in opto-PKR cells treated with the indicated compounds for the indicated durations in light (blue and cyan bars) and in dark (gray and black bars), as measured by AlphaLISA. Values are normalized to those of DMSO (0.5%) vehicle and represented in $\log_{10}$. Results are representative of one of two independent experiments performed on different occasions.

(G) Proposed mechanism of action of IBX-200 and IBX-204 (as well as cyclized forms of IBX-202 resulting in IBX-200 analogs). Additional mechanisms may contribute to the observed activity.

See also Figure S4.

IBX-202 treatment as well, consistent with IBX-202's conversion into an IBX-200 analog. Importantly, in GCN2-KO cells, all compounds continued to enhance cell death compared with light and vehicle-only treatment but only at higher concentrations (>1 μM). This observation suggests that residual GCN2 levels, compensatory or cooperative activation of other stress sensor kinases,[2] or other uncharacterized targets might contribute to cell death, especially at higher compound concentrations. Indeed, consistent with these possibilities, we found that ATF4 and CHOP levels were still increased in GCN2-KO cells after compound treatment (Figure S4M). Additional kinase binding panels and the observation of no differential change in cell viability in PKR/GCN2 double-KO opto-PKR H4 cells relative to GCN2-KO cells further support that IBX-200 and IBX-204 act selectively on GCN2 (Figures S4N and S4O).

Building on our observations, we directly measured levels of GCN2 phosphorylated at Thr899 (pGCN2 Thr899) in opto-PKR cells treated with each of IBX-200, IBX-202, and IBX-204 (Figure 5F). These measurements indicated that GCN2 was activated in opto-PKR cells treated with varying concentrations (0.4–40 μM) of compound, with ~2- to 6-fold increased ratios of pGCN2 Thr899 to total GCN2 levels 3 h post treatment and higher ratios observed in cells co-treated with blue light. Importantly, these results demonstrate that compound treatment at sub-K_d concentrations activates GCN2, consistent with the low cell-based EC_{50} values observed in our opto-PKR experiments. To further test the role of activated GCN2 independently of opto-PKR, we co-treated chem-PKR cells with GCN2iB (10 μM) in the presence of B/B homodimerizer (1 nM) and IBX-200 or IBX-204. We observed rescue of cell death similar to co-treatment with

Please cite this article in press as: Wong et al., Optogenetics-enabled discovery of integrated stress response modulators, Cell (2025), https://doi.org/10.1016/j.cell.2025.06.024

2BAct (10 μM; Figure S4P), supporting that GCN2 is a functional target of IBX-200 and IBX-204.

Together, our results suggest a proposed mechanism in which IBX-200 and IBX-204 (as well as cyclized forms of IBX-202 resulting in IBX-200 analogs) potentiate the ISR in part by increasing the active form of GCN2 (Figure 5G). Compound binding proximal to the C-lobe of GCN2 may contribute to activation of GCN2, as measured by trans-autophosphorylation at Thr899. This is consistent with the observation that a single amino acid mutation (R794G) in GCN2 has been shown to make it hyperactive by ~75-fold,[54] suggesting that pharmacologic modulation may sustain GCN2 activation at low compound concentrations. Canonically activated GCN2 (pGCN2 Thr899)[54,55] results in ISR signaling, leading to increases in ATF4 and CHOP expression.[1–3] In the presence of ISR stress, the compounds increase ATF4 expression to potentiate terminal ISR signaling, thereby decreasing cell viability; in the absence of stress, increases in ATF4 lead to an adaptive ISR, manifesting in no substantive decrease in cell viability. It is also important to underscore that cell viability decreases are observed in GCN2-KO cells incubated in light. Given that IBX-200 and IBX-204 heighten oxidative stress, which is also known to activate HRI and PERK[1–3] and potentially ATF4,[57] it is possible that compound treatment alters phenotypes (including cellular redox state) sensed by ISR components to indirectly and further activate the ISR, and GCN2 may be redundant for sensing the stress imparted by the compounds.

Broad-spectrum antiviral activity

Viral stress is detected by PKR.[2,3] Small-molecule activators of the ISR, including salubrinal and Sephin1, have been shown to decrease viral replication,[16,58] and viral infection has been shown to increase ATF4 signaling.[59] Building on these observations, we hypothesized that ISR potentiators could inhibit viral replication without collateral cytotoxicity. To investigate this hypothesis, we focused on herpes simplex virus type 1 (HSV-1) strain KOS, Zika virus (ZKV) strain MR766, and respiratory syncytial virus (RSV) strain B WV/14617/85. These viral strains were chosen as a starting point to sample diverse viruses: HSV-1 is a double-stranded DNA (dsDNA) virus, whereas ZKV and RSV represent different positive-sense and negative-sense families of single-stranded RNA (ssRNA) viruses.

We infected host cells with each virus and treated the infected cells with varying concentrations of compound, finding that, across all viruses, compound treatment largely decreased viral plaque-forming units (PFUs). Most antiviral IC_{50} values were between ~1 and ~100 μM, indicating that these compounds maintain selectivity against viruses relative to their mammalian cell CC_{50} values (Figures 6A and S5A–S5D). For HSV-1, plaques formed in the presence of compound were consistently smaller than untreated controls, indicating that the compounds specifically impair viral replication rather than initial host cell entry (Figure S5A). IBX-204 decreased HSV-1 titers less effectively than IBX-200 and IBX-202 and failed to decrease RSV titers at concentrations as high as 100 μM. This reduced antiviral effect may stem from IBX-204's weaker ability to elevate ATF4 levels at early incubation times, as supported by our immunofluorescence data (Figures 4A–4C). In contrast, all compounds were similarly effective and more potent (IC_{50} values < 10 μM) against ZKV (and for IBX-200 and IBX-202 against RSV) than HSV-1. This overall difference in potency might be explained in part by PKR's sensing of dsRNA and the fact that dsRNA intermediates are generated as part of the replication process of ssRNA viruses (as opposed to being generated by a different mechanism thought to involve bidirectional transcription in the case of dsDNA viruses[60]). Although further work is needed clarify how the replication of different viruses is affected by ISR potentiation, these findings consistently suggest that IBX-200, IBX-202, and IBX-204 represent structural classes of compounds with selective and broad-spectrum antiviral activity.

In vivo efficacy in a mouse model of ocular herpesvirus infection

We next tested for efficacy in treating viral infections *in vivo*. For our initial experiments, we focused on testing the most potently antiviral compound, IBX-200, in a mouse model of ocular herpesvirus infection[16] (Figure 6B), a well-established viral infection model.[61,62] C57BL/6J mice were treated topically with vehicle, IBX-200 (10 mM), or acyclovir (10 mM) eyedrops daily, starting after infection. On the day of infection, scars were inflicted on the right corneas and each eye was infected with ~10^5 PFU of HSV-1 strain KOS. Overall disease burden was not severe in this model, consistent with previous work[61]; nevertheless, we found that mice treated with IBX-200 exhibited improved disease scores compared with vehicle treatment, similar to treatment with acyclovir (Figure 6C). We titered viral PFUs from tear swabs collected at 3 days post infection and found that, despite variability in PFU/mL values, IBX-200 treatment significantly reduced the average viral titer by approximately 5-fold (Figure 6D). Acyclovir treatment also resulted in similar mean decreases in PFU/mL relative to vehicle. Additionally, we observed mean decreases of ~20% in the levels of CXCL10/IP-10, a chemokine expressed during HSV-1 infection,[63] in the eye homogenates of IBX-200 and acyclovir-treated mice as compared with vehicle-treated mice, consistent with potentially decreased inflammation and the lower mean disease scores in these mice (Figure S5E). These results indicate that IBX-200 is effective at decreasing HSV-1 titers *in vivo* and suggest that the discovered compounds may be further developed for the therapeutic treatment of viral infections.

Toxicology and structure-activity relationship analyses

As a preliminary step toward further development, we characterized hemolysis, iron chelation, genotoxicity, and liver damage markers induced by IBX-200, IBX-202, and IBX-204 treatment, finding favorable toxicity profiles for all compounds (Figures S6A–S6E; STAR Methods). We next performed structure-activity relationship (SAR) analyses of the three scaffolds shown in Figures 7A–7C, which generalize the three structural classes of compounds identified in this study. By varying the functional groups of the 1-(3-aminothieno[2,3-b]pyridin-2-yl)ethanone, nicotinonitrile, and quinoline/1,2,4-oxadiazole-containing scaffolds as shown, we procured and tested 95, 72, and 36 chemical analogs of IBX-200, IBX-202, and IBX-204, respectively (Data S2). In dose-response experiments measuring the selective killing of opto-PKR H4 cells incubated in light as opposed to dark, we found that 14, 6, and 13 compounds in each respective structural group

Please cite this article in press as: Wong et al., Optogenetics-enabled discovery of integrated stress response modulators, Cell (2025), https://doi.org/10.1016/j.cell.2025.06.024

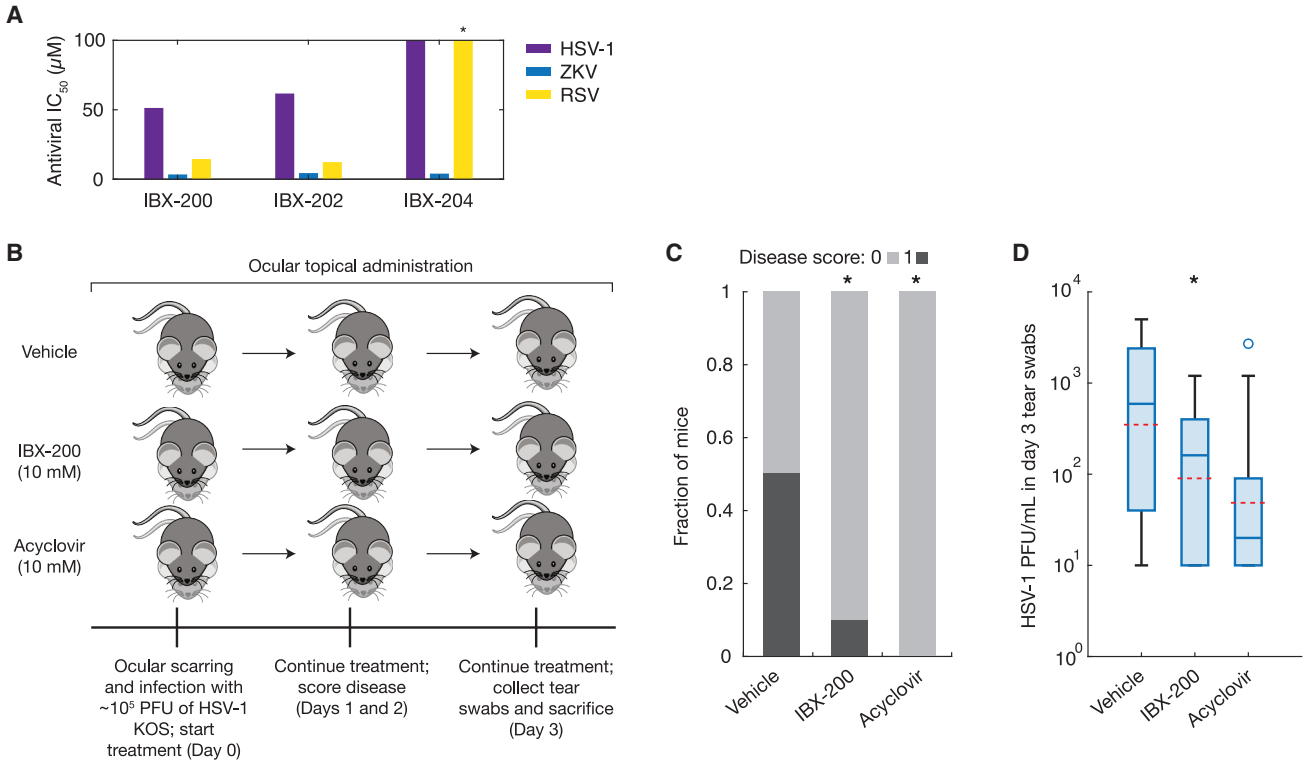

Figure 6. Antiviral activity of compounds

(A) Antiviral IC_{50} values for IBX-200, IBX-202, and IBX-204 against three viruses. Values were inferred by curve fitting for data generated from two biological replicates (Figures S5B–S5D). Asterisks indicate values ≥100 μM.

(B) Schematic of the *in vivo* study. Mice were ocularly infected with ~10^5 PFU of HSV-1 strain KOS, then treated with vehicle (70% DMSO:30% PBS), IBX-200, or acyclovir eyedrops daily after infection. Thirty mice (10 for vehicle, 10 for IBX-200, and 10 for acyclovir) were used in the study.

(C) Distribution of disease scores 2 days post infection for all mice, where scores of 1 indicate symptomatic viral infections (see STAR Methods for details). Two-sample exact permutation test for lower mean disease score relative to vehicle: $^*p < 0.05$.

(D) Distribution of viral PFU/mL in tear swabs 3 days post infection for all mice. Boxplots indicate 25th percentile, median, and 75th percentile values, whiskers indicate minimum and maximum values, and points indicate outliers. Red dashed lines indicate mean values. Two-sample exact permutation test for lower mean PFU/mL relative to vehicle: $^*p < 0.05$.

See also Figures S5, S6, and S7.

exhibited high potency against cells incubated in light (EC_{50} < 1 μM) as opposed to dark (CC_{50} > 50 μM; Figures 7D–7F; Data S2). Several compounds exhibited lower EC_{50} values against cells in light than did IBX-200, IBX-202, and IBX-204, respectively (Figure S7A). Notably, IBX-210, IBX-211, and IBX-212 (Figures 7G–7I) were chemically diverse and highly selective analogs, with corresponding EC_{50} values between 200 and 500 nM. Furthermore, we tested the antiviral activity of multiple selective structural analogs representing each scaffold and found that these analogs were also effective at reducing HSV-1 replication *in vitro* (Figure S7B). Taken together, these results indicate that the chemical series described in this study can be further optimized for higher potency, increased efficacy in disease models, and potentially other favorable medicinal chemistry properties.

DISCUSSION

Dysregulation of the ISR contributes to numerous diseases, and the ISR has been viewed as a rheostat important to fundamental processes, including cellular homeostasis and long-term memory formation.[3] The compounds discovered here may be applicable to diseases driven by loss of homeostasis, which, in addition to viral infections, may include cancer, metabolic disorders, and neurodegeneration. Inhibition of the ISR transforms mouse fibroblasts and increases tumor formation in immunodeficient mice,[3] while oncogenic stress also activates the ISR.[64] ATF4 is frequently upregulated in cancer cells[57] and has context-dependent pro-survival and pro-apoptotic effects. Using ISR potentiators to selectively trigger apoptosis of these stressed cells may permit a disease-modifying approach to cancer. Additionally, the ISR regulates amino acid metabolism and oxidative stress responses,[1,3,65] and aberrant ISR phenotypes have been shown to lead to neurodegeneration.[66,67] Selectively targeting stressed cells in these contexts may help to ameliorate disease pathology.

Our findings indicate that putative ISR potentiators are effective against different viruses, including HSV-1, ZKV, and RSV. In contrast to cancer, metabolic disorders, and neurodegeneration, viral infections can be acute, and developing drug candidates capable of treating systemic viral infections, including

Please cite this article in press as: Wong et al., Optogenetics-enabled discovery of integrated stress response modulators, Cell (2025), https://doi.org/10.1016/j.cell.2025.06.024

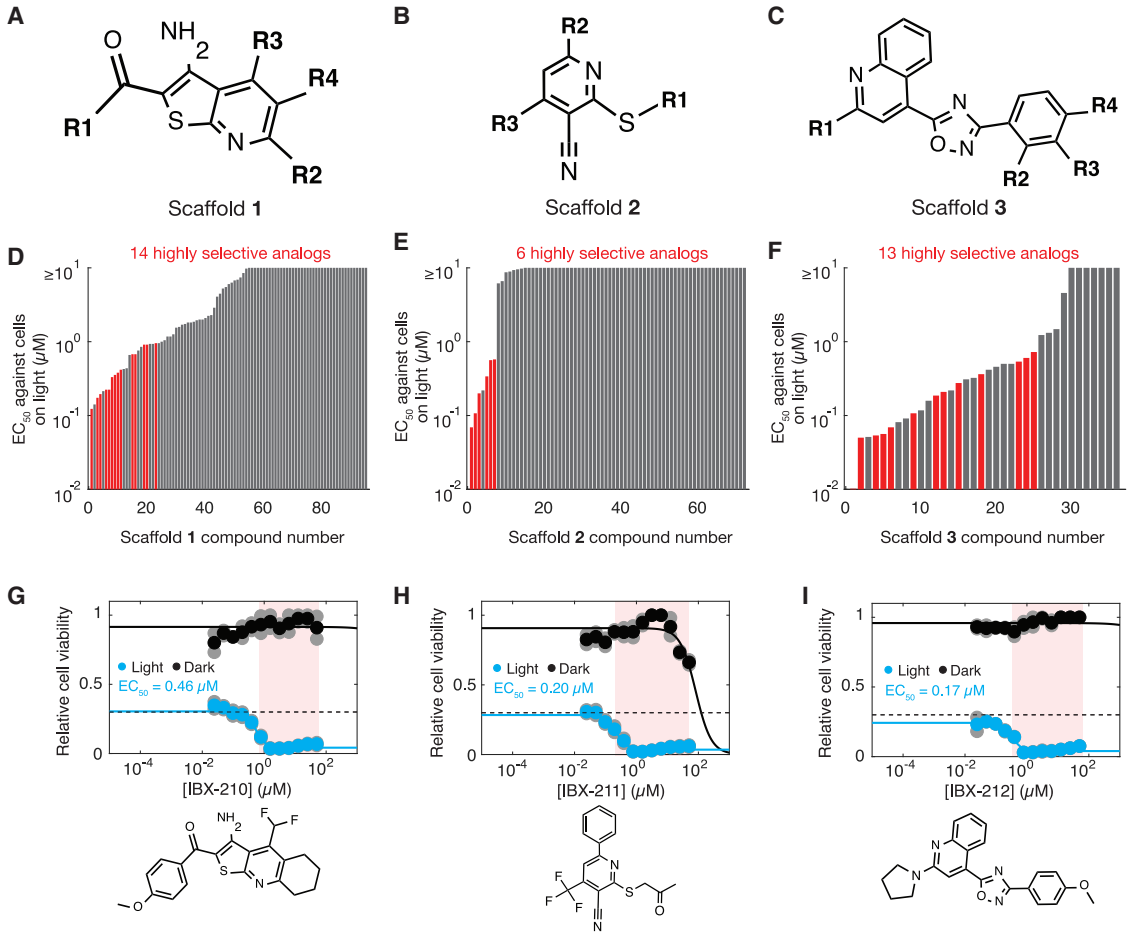

Figure 7. Structure-activity relationship analyses

(A–C) Functional group modifications (R1–R4) to three scaffolds considered in our analyses.

(D–F) Rank-ordered EC_{50} values for all tested structural analogs against opto-PKR cells incubated in light in the presence of compound for 24 h. Red bars indicate selective compounds for which EC_{50} < 1 μM in light and CC_{50} > 50 μM in dark. Results are representative of one biological replicate.

(G–I) Cell viability dose-response curves for opto-PKR cells treated with selective and structurally diverse compounds from each of (D)–(F). Cells were incubated for 24 h in light or in dark (cyan and black points, respectively). Colored points represent the means of two biological replicates (gray points). Values were normalized against those of DMSO (0.5%) vehicle-treated cells in dark, and the dashed line indicates the baseline cell viability value of vehicle-treated cells in light. Decoupled cell viability decreases are highlighted in red.

See also Figure S7.

those leading to viral encephalitis, remains a challenge. Targeting the ISR as a highly conserved host cell stress response to viral infection offers an attractive avenue toward developing broad-spectrum antiviral compounds. Because they modulate host cell phenotypes without collateral cytotoxicity and do not directly target viral nucleic acid replication, ISR potentiators can promote organismal homeostasis and avoid antiviral resistance. Indeed, due to these features, host-directed antiviral compounds have been a long sought-after modality of drug candidates.[68,69] We anticipate that further studies of ISR potentiators as antiviral drug candidates will lead to additional insights on the phenotypic effects of these compounds and how these effects translate to disease modification.

More broadly, the structural dissimilarity and mechanisms of action of the compounds identified here, as compared with known compounds that modulate the ISR, suggest that vast chemical spaces of ISR modulators remain to be discovered. These compounds may exhibit less cytotoxicity and fewer pleiotropic effects than known small-molecule modulators of the ISR, several of which have been appreciated to have questionable mechanisms of action.[70,71] The optogenetic platform developed in this study allows us to activate and target the ISR in an on-pathway, tunable, and time-resolved manner, overcoming the disadvantages of administering small-molecule stressors to cells. Although we have not leveraged this feature as part of our screening, our platform also enables dynamic control of the ISR, which may be relevant to simulating the chronic stress that underlies neurodegenerative and other diseases.[2,72,73] Due to their selectivity against stressed cells, the compounds discovered here might be efficacious when administered at low doses chronically, similar to previously considered "hit-and-run" dosing regimens for senolytics, for which selectively killing a subpopulation of senescent cells suffices

to be disease modifying.[74,75] Thus, optogenetic manipulation offers a broadly applicable approach for precisely controlling cellular stress states *in vitro*, significantly enhancing the identification of therapeutic agents.

Our optogenetic platform is phenotypic by design: this enables the discovery of previously unknown mechanisms of action but requires downstream target deconvolution. Although we have characterized GCN2 activation as a factor relevant to the mechanism(s) of action of the identified compounds, detailed studies are needed to fully elucidate the specificity of target engagement. Crystal structures of IBX-200 and IBX-204 in complex with GCN2 would further support our proposed model of GCN2 binding proximal to the C-lobe, and GCN2 agonism and hyperactive mutant studies could enable more detailed explorations of compound effects. Functional CRISPR screens[76] incorporating measures of ISR pathway activation as readouts may identify alternative targets. More recent technologies, such as photocatalytic proximity labeling,[77] could enhance target deconvolution sensitivity, further clarifying the mechanisms of action of the compounds identified here.

Overall, our findings suggest that optogenetics, a technique still nascent for many biological applications,[23,78–84] can be leveraged to identify classes of ISR-modifying compounds. We anticipate that compounds modulating other pathways (for instance, Wnt/β-catenin and Ras/Erk signaling) in unexpected ways remain to be discovered using similar optogenetic approaches.[78,85–87] These pathways are known for their molecular complexity, context-dependent activity, and rich temporal dynamics. Traditional activation methods often involve compounds with pleiotropic effects (e.g., lithium for Wnt/β-catenin signaling), but optogenetics provides unique advantages—such as enhanced specificity, precise timing, and spatial control—which could address these challenges. Additionally, the use of optogenetics to simultaneously activate multiple signaling pathways would be an attractive approach to studying the crosstalk and combinatorial effects of these pathways, and leveraging orthogonal light-responsive systems (e.g., PhyB and Cry2) would allow for the precise control of different pathways with distinct wavelengths of light.[88] Elegant advances in engineering phytochrome-based optogenetic tools, including ΔPhyA (REDMAP)[83] and Fn-/Pn-BphP (REDLIP),[89] have demonstrated high (>150-fold) induction of target genes, rapid response times (seconds), deep tissue penetration, long-duration stimulus memory (tens of hours), and reduced phototoxicity. Such systems could enhance the discovery of selective molecules against intended signaling pathways, reducing potential confounding factors (such as blue light phototoxicity or unintended off-target effects) and enabling precise spatiotemporal and *in vivo* analysis.

Recent works have emphasized the importance of generating high-quality on-pathway data, free of confounding variables, for productive drug discovery efforts, especially those leveraging machine-learning approaches and recent screening modalities.[90–92] Optogenetics—and, more broadly, synthetic biology—enables control over biological systems that will help to generate accurate phenotypic data. As a field originating from the phenotypic control of bacteria over two decades ago,[93,94] synthetic biology may be particularly well-suited to enabling next-generation phenotypic approaches to drug discovery.

Limitations of the study

Although our engineered optogenetic construct, opto-PKR, responds specifically to blue light and our approach identifies ISR modulators, it is possible that blue light can activate other cellular pathways, induce cell cytotoxic effects, or generate ROS to contribute to ISR signaling.[95–98] Although the intensity of light required to activate opto-PKR is relatively low, at ∼100 μW/cm^2 (three to four orders of magnitude lower than required for typical confocal imaging of fluorescent proteins), we cannot completely discount the possibility of these and other off-target effects caused by light exposure. These possibilities emphasize the importance of performing detailed control experiments to validate any optogenetic tool before deploying it in large screens and of mechanistically validating any identified hit compound. Our construct also relies on clustering of PKR, and how well optogenetic control generalizes to other proteins and pathways will vary depending on how well optogenetic induction can mimic physiological activation. For many proteins, we anticipate that the development and characterization of specific optogenetic constructs is needed to address this issue. Finally, the ISR has been implicated in many diseases due to its role as a highly conserved and central cellular stress response,[2,3] but drug candidates that modulate the ISR should be tested for efficacy on a disease-by-disease basis to further support this hypothesis.

RESOURCE AVAILABILITY

Lead contact

Further information and requests for resources should be directed to, and will be fulfilled by, the lead contact, James J. Collins (jimjc@mit.edu).

Materials availability

Cell lines generated in this study are available on request, but we may require a materials transfer agreement and/or payment if there is potential for commercial application.

Data and code availability

- All data reported in this paper will be shared by the lead contact upon request. Data from single-cell RNA sequencing reads have been deposited on BioProject under accession PRJNA1213751 (BioSample accessions SAMN46345881, SAMN46345882, SAMN46345883, and SAMN46345884).
- This paper does not report original code.
- Any additional information required to reanalyze the data reported in this paper is available from the lead contact upon request.

ACKNOWLEDGMENTS

We thank Neosome Life Sciences for assistance with *in vivo* experiments, MBC BioLabs for assistance with instrumentation, and Shannon Bryant for assistance with SPR experiments. J.M.U.V. was supported by the BioPACIFIC Materials Innovation Platform of the National Science Foundation under award no. DMR-1933487. J.J.C. was supported by the Defense Threat Reduction Agency (grant number HDTRA12210032). M.Z.W. was supported by the US Army Research Office under contract W911NF-19-D-0001 and cooperative agreement W911NF-19-2-0026 for the Institute for Collaborative Biotechnologies.

AUTHOR CONTRIBUTIONS

F.W. conceived research, performed or directed all experiments, wrote the paper, and supervised research. A.L., S.O., R.S.L., J.N., Y.R., and S.P.B.

conceived research and performed experiments. V.S. performed data analysis. B.R.L., T.B., E.D., and J.R.R.R. performed experiments. J.M.U.V. contributed to the design of the optogenetic illumination system. S.W. assisted with experiments. H.K. contributed to conceiving research and experiments. J.J.C. supervised research. M.Z.W. conceived research, directed experiments, and supervised research. All authors assisted with manuscript editing.

DECLARATION OF INTERESTS

F.W. and M.Z.W. are co-founders of Integrated Biosciences. J.J.C. is the founding scientific advisory board chair of Integrated Biosciences and an academic co-founder and board member of Cellarity. F.W., A.L., S.O., R.S.L., Y.R., S.P.B., V.S., B.R.L., H.K., J.J.C., and M.Z.W. may hold equity interest in Integrated Biosciences. S.W. is an employee of Illumina Ventures. F.W., A.L., S.O., R.S.L., S.P.B., B.R.L., and M.Z.W. have filed a patent based on the results of this work.

STAR★METHODS

Detailed methods are provided in the online version of this paper and include the following:

SUPPLEMENTAL INFORMATION

Supplemental information can be found online at https://doi.org/10.1016/j.cell.2025.06.024.

Received: March 25, 2024
Revised: January 21, 2025
Accepted: June 17, 2025

REFERENCES

1. Harding, H.P., Zhang, Y., Zeng, H., Novoa, I., Lu, P.D., Calfon, M., Sadri, N., Yun, C., Popko, B., Paules, R., et al. (2003). An integrated stress response regulates amino acid metabolism and resistance to oxidative stress. Mol. Cell *11*, 619–633. https://doi.org/10.1016/s1097-2765(03)00105-9.
2. Pakos-Zebrucka, K., Koryga, I., Mnich, K., Ljujic, M., Samali, A., and Gorman, A.M. (2016). The integrated stress response. EMBO Rep. *17*, 1374–1395. https://doi.org/10.15252/embr.201642195.
3. Costa-Mattioli, M., and Walter, P. (2020). The integrated stress response: From mechanism to disease. Science *368*, eaat5314. https://doi.org/10.1126/science.aat5314.
4. Hetz, C., Zhang, K., and Kaufman, R.J. (2020). Mechanisms, regulation and functions of the unfolded protein response. Nat. Rev. Mol. Cell Biol. *21*, 421–438. https://doi.org/10.1038/s41580-020-0250-z.
5. Rabouw, H.H., Visser, L.J., Passchier, T.C., Langereis, M.A., Liu, F., Giansanti, P., van Vliet, A.L.W., Dekker, J.G., van der Grein, S.G., Saucedo, J.G., et al. (2020). Inhibition of the integrated stress response by viral proteins that block p-eIF2-eIF2B association. Nat. Microbiol. *5*, 1361–1373. https://doi.org/10.1038/s41564-020-0759-0.
6. Ruggieri, A., Dazert, E., Metz, P., Hofmann, S., Bergeest, J.P., Mazur, J., Bankhead, P., Hiet, M.S., Kallis, S., Alvisi, G., et al. (2012). Dynamic oscillation of translation and stress granule formation mark the cellular response to virus infection. Cell Host Microbe *12*, 71–85. https://doi.org/10.1016/j.chom.2012.05.013.
7. Emanuelli, G., Nassehzadeh-Tabriz, N., Morrell, N.W., and Marciniak, S.J. (2020). The integrated stress response in pulmonary disease. Eur. Respir. Rev. *29*, 200184. https://doi.org/10.1183/16000617.0184-2020.
8. Watanabe, S., Markov, N.S., Lu, Z., Piseaux Aillon, R., Soberanes, S., Runyan, C.E., Ren, Z., Grant, R.A., Maciel, M., Abdala-Valencia, H., et al. (2021). Resetting proteostasis with ISRIB promotes epithelial differentiation to attenuate pulmonary fibrosis. Proc. Natl. Acad. Sci. USA *118*, e2101100118. https://doi.org/10.1073/pnas.2101100118.
9. Chou, A., Krukowski, K., Jopson, T., Zhu, P.J., Costa-Mattioli, M., Walter, P., and Rosi, S. (2017). Inhibition of the integrated stress response reverses cognitive deficits after traumatic brain injury. Proc. Natl. Acad. Sci. USA *114*, E6420–E6426. https://doi.org/10.1073/pnas.1707661114.
10. Krukowski, K., Nolan, A., Frias, E.S., Boone, M., Ureta, G., Grue, K., Paladini, M.S., Elizarraras, E., Delgado, L., Bernales, S., et al. (2020). Small molecule cognitive enhancer reverses age-related memory decline in mice. eLife *9*, e62048. https://doi.org/10.7554/eLife.62048.
11. Moreno, J.A., Radford, H., Peretti, D., Steinert, J.R., Verity, N., Martin, M.G., Halliday, M., Morgan, J., Dinsdale, D., Ortori, C.A., et al. (2012). Sustained translational repression by eIF2α-P mediates prion neurodegeneration. Nature *485*, 507–511. https://doi.org/10.1038/nature11058.
12. Tribouillard-Tanvier, D., Béringue, V., Desban, N., Gug, F., Bach, S., Voisset, C., Galons, H., Laude, H., Vilette, D., and Blondel, M. (2008). Antihypertensive drug guanabenz is active in vivo against both yeast and mammalian prions. PLoS One *3*, e1981. https://doi.org/10.1371/journal.pone.0001981.

13. Tsaytler, P., Harding, H.P., Ron, D., and Bertolotti, A. (2011). Selective inhibition of a regulatory subunit of protein phosphatase 1 restores proteostasis. Science *332*, 91–94. https://doi.org/10.1126/science.1201396.

14. Das, I., Krzyzosiak, A., Schneider, K., Wrabetz, L., D'Antonio, M., Barry, N., Sigurdardottir, A., and Bertolotti, A. (2015). Preventing proteostasis diseases by selective inhibition of a phosphatase regulatory subunit. Science *348*, 239–242. https://doi.org/10.1126/science.aaa4484.

15. Jammi, N.V., Whitby, L.R., and Beal, P.A. (2003). Small molecule inhibitors of the RNA-dependent protein kinase. Biochem. Biophys. Res. Commun. *308*, 50–57. https://doi.org/10.1016/s0006-291x(03)01318-4.

16. Boyce, M., Bryant, K.F., Jousse, C., Long, K., Harding, H.P., Scheuner, D., Kaufman, R.J., Ma, D., Coen, D.M., Ron, D., et al. (2005). A selective inhibitor of eIF2alpha dephosphorylation protects cells from ER stress. Science *307*, 935–939. https://doi.org/10.1126/science.1101902.

17. Sidrauski, C., McGeachy, A.M., Ingolia, N.T., and Walter, P. (2015). The small molecule ISRIB reverses the effects of eIF2α phosphorylation on translation and stress granule assembly. eLife *4*, e05033. https://doi.org/10.7554/eLife.05033.

18. Bakunts, A., Orsi, A., Vitale, M., Cattaneo, A., Lari, F., Tadè, L., Sitia, R., Raimondi, A., Bachi, A., and van Anken, E. (2017). Ratiometric sensing of BiP-client versus BiP levels by the unfolded protein response determines its signaling amplitude. eLife *6*, e27518. https://doi.org/10.7554/eLife.27518.

19. Wong, Y.L., LeBon, L., Basso, A.M., Kohlhaas, K.L., Nikkel, A.L., Robb, H.M., Donnelly-Roberts, D.L., Prakash, J., Swensen, A.M., Rubinstein, N.D., et al. (2019). eIF2B activator prevents neurological defects caused by a chronic integrated stress response. eLife *8*, e42940. https://doi.org/10.7554/eLife.42940.

20. Halliday, M., Radford, H., Zents, K.A.M., Molloy, C., Moreno, J.A., Verity, N.C., Smith, E., Ortori, C.A., Barrett, D.A., Bushell, M., et al. (2017). Repurposed drugs targeting eIF2α-P-mediated translational repression prevent neurodegeneration in mice. Brain *140*, 1768–1783. https://doi.org/10.1093/brain/awx074.

21. Zhou, Z., Liu, Y., Feng, Y., Klepin, S., Tsimring, L.S., Pillus, L., Hasty, J., and Hao, N. (2023). Engineering longevity-design of a synthetic gene oscillator to slow cellular aging. Science *380*, 376–381. https://doi.org/10.1126/science.add7631.

22. Batjargal, T., Zappa, F., Grant, R.J., Piscopio, R.A., Chialastri, A., Dey, S. S., Acosta-Alvear, D., and Wilson, M.Z. (2023). Optogenetic control of the integrated stress response reveals proportional encoding and the stress memory landscape. Cell Syst. *14*, 551–562.e5. https://doi.org/10.1016/j.cels.2023.06.001.

23. Zhang, H., and Cohen, A.E. (2017). Optogenetic approaches to drug discovery in neuroscience and beyond. Trends Biotechnol. *35*, 625–639. https://doi.org/10.1016/j.tibtech.2017.04.002.

24. Zappa, F., Muniozguren, N.L., Wilson, M.Z., Costello, M.S., Ponce-Rojas, J.C., and Acosta-Alvear, D. (2022). Signaling by the integrated stress response kinase PKR is fine-tuned by dynamic clustering. J. Cell Biol. *221*, e202111100. https://doi.org/10.1083/jcb.202111100.

25. Mayo, C.B., Erlandsen, H., Mouser, D.J., Feinstein, A.G., Robinson, V.L., May, E.R., and Cole, J.L. (2019). Structural basis of protein kinase R autophosphorylation. Biochemistry *58*, 2967–2977. https://doi.org/10.1021/acs.biochem.9b00161.

26. Corbet, G.A., Burke, J.M., Bublitz, G.R., Tay, J.W., and Parker, R. (2022). dsRNA-induced condensation of antiviral proteins modulates PKR activity. Proc. Natl. Acad. Sci. USA *119*, e2204235119. https://doi.org/10.1073/pnas.2204235119.

27. Liu, J., Xu, Y., Stoleru, D., and Salic, A. (2012). Imaging protein synthesis in cells and tissues with an alkyne analog of puromycin. Proc. Natl. Acad. Sci. USA *109*, 413–418. https://doi.org/10.1073/pnas.1111561108.

28. Oyadomari, S., and Mori, M. (2004). Roles of CHOP/GADD153 in endoplasmic reticulum stress. Cell Death Differ. *11*, 381–389. https://doi.org/10.1038/sj.cdd.4401373.

29. Hu, H., Tian, M., Ding, C., and Yu, S. (2018). The C/EBP Homologous Protein (CHOP) transcription factor functions in endoplasmic reticulum stress-induced apoptosis and microbial infection. Front. Immunol. *9*, 3083. https://doi.org/10.3389/fimmu.2018.03083.

30. Bennett, B.L., Sasaki, D.T., Murray, B.W., O'Leary, E.C., Sakata, S.T., Xu, W., Leisten, J.C., Motiwala, A., Pierce, S., Satoh, Y., et al. (2001). SP600125, an anthrapyrazolone inhibitor of Jun N-terminal kinase. Proc. Natl. Acad. Sci. USA *98*, 13681–13686. https://doi.org/10.1073/pnas.251194298.

31. Stokes, J.M., Yang, K., Swanson, K., Jin, W., Cubillos-Ruiz, A., Donghia, N.M., MacNair, C.R., French, S., Carfrae, L.A., Bloom-Ackermann, Z., et al. (2020). A deep learning approach to antibiotic discovery. Cell *180*, 688–702.e13. https://doi.org/10.1016/j.cell.2020.01.021.

32. Wong, F., Omori, S., Donghia, N.M., Zheng, E.J., and Collins, J.J. (2023). Discovering small-molecule senolytics with deep neural networks. Nat. Aging *3*, 734–750. https://doi.org/10.1038/s43587-023-00415-z.

33. Wong, F., Zheng, E.J., Valeri, J.A., Donghia, N.M., Anahtar, M.N., Omori, S., Li, A., Cubillos-Ruiz, A., Krishnan, A., Jin, W., et al. (2024). Discovery of a structural class of antibiotics with explainable deep learning. Nature *626*, 177–185. https://doi.org/10.1038/s41586-023-06887-8.

34. Wong, F., Omori, S., Li, A., Krishnan, A., Lach, R.S., Rufo, J., Wilson, M. Z., and Collins, J.J. (2025). An explainable deep learning platform for molecular discovery. Nat. Protoc. *20*, 1020–1056. https://doi.org/10.1038/s41596-024-01084-x.

35. Lipinski, C.A., Lombardo, F., Dominy, B.W., and Feeney, P.J. (2001). Experimental and computational approaches to estimate solubility and permeability in drug discovery and development settings. Adv. Drug Deliv. Rev. *46*, 3–26. https://doi.org/10.1016/s0169-409x(00)00129-0.

36. Pajouhesh, H., and Lenz, G.R. (2005). Medicinal chemical properties of successful central nervous system drugs. Neurorx *2*, 541–553. https://doi.org/10.1602/neurorx.2.4.541.

37. Baell, J.B., and Holloway, G.A. (2010). New substructure filters for removal of pan assay interference compounds (PAINS) from screening libraries and for their exclusion in bioassays. J. Med. Chem. *53*, 2719–2740. https://doi.org/10.1021/jm901137j.

38. Brenk, R., Schipani, A., James, D., Krasowski, A., Gilbert, I.H., Frearson, J., and Wyatt, P.G. (2008). Lessons learnt from assembling screening libraries for drug discovery for neglected diseases. ChemMedChem *3*, 435–444. https://doi.org/10.1002/cmdc.200700139.

39. Belyy, V., Zuazo-Gaztelu, I., Alamban, A., Ashkenazi, A., and Walter, P. (2022). Endoplasmic reticulum stress activates human IRE1α through reversible assembly of inactive dimers into small oligomers. eLife *11*, e74342. https://doi.org/10.7554/eLife.74342.

40. Lu, L., Han, A.P., and Chen, J.J. (2001). Translation initiation control by heme-regulated eukaryotic initiation factor 2alpha kinase in erythroid cells under cytoplasmic stresses. Mol. Cell. Biol. *21*, 7971–7980. https://doi.org/10.1128/MCB.21.23.7971-7980.2001.

41. McEwen, E., Kedersha, N., Song, B., Scheuner, D., Gilks, N., Han, A., Chen, J.J., Anderson, P., and Kaufman, R.J. (2005). Heme-regulated inhibitor kinase-mediated phosphorylation of eukaryotic translation initiation factor 2 inhibits translation, induces stress granule formation, and mediates survival upon arsenite exposure. J. Biol. Chem. *280*, 16925–16933. https://doi.org/10.1074/jbc.M412882200.

42. Rabouw, H.H., Langereis, M.A., Anand, A.A., Visser, L.J., de Groot, R.J., Walter, P., and van Kuppeveld, F.J.M. (2019). Small molecule ISRIB suppresses the integrated stress response within a defined window of activation. Proc. Natl. Acad. Sci. USA *116*, 2097–2102. https://doi.org/10.1073/pnas.1815767116.

43. Je, H.S., Lu, Y., Yang, F., Nagappan, G., Zhou, J., Jiang, Z., Nakazawa, K., and Lu, B. (2009). Chemically inducible inactivation of protein synthesis in genetically targeted neurons. J. Neurosci. *29*, 6761–6766. https://doi.org/10.1523/JNEUROSCI.1280-09.2009.

44. Han, J., Back, S.H., Hur, J., Lin, Y.H., Gildersleeve, R., Shan, J., Yuan, C. L., Krokowski, D., Wang, S., Hatzoglou, M., et al. (2013). ER-stress-induced transcriptional regulation increases protein synthesis leading to cell death. Nat. Cell Biol. *15*, 481–490. https://doi.org/10.1038/ncb2738.

45. Tian, F., Zhao, J., Bu, S., Teng, H., Yang, J., Zhang, X., Li, X., and Dong, L. (2020). KLF6 induces apoptosis in human lens epithelial cells through the ATF4-ATF3-CHOP axis. Drug Des. Devel. Ther. *14*, 1041–1055. https://doi.org/10.2147/DDDT.S218467.

46. Masson, G.R. (2019). Towards a model of GCN2 activation. Biochem. Soc. Trans. *47*, 1481–1488. https://doi.org/10.1042/BST20190331.

47. Dong, J., Qiu, H., Garcia-Barrio, M., Anderson, J., and Hinnebusch, A.G. (2000). Uncharged tRNA activates GCN2 by displacing the protein kinase moiety from a bipartite tRNA-binding domain. Mol. Cell *6*, 269–279. https://doi.org/10.1016/s1097-2765(00)00028-9.

48. Wek, S.A., Zhu, S., and Wek, R.C. (1995). The histidyl-tRNA synthetase-related sequence in the eIF-2 alpha protein kinase GCN2 interacts with tRNA and is required for activation in response to starvation for different amino acids. Mol. Cell. Biol. *15*, 4497–4506. https://doi.org/10.1128/MCB.15.8.4497.

49. Carlson, K.R., Georgiadis, M.M., Tameire, F., Staschke, K.A., and Wek, R.C. (2023). Activation of Gcn2 by small molecules designed to be inhibitors. J. Biol. Chem. *299*, 104595. https://doi.org/10.1016/j.jbc.2023.104595.

50. Piecyk, M., Ferraro-Peyret, C., Laville, D., Perros, F., and Chaveroux, C. (2024). Novel insights into the GCN2 pathway and its targeting. Therapeutic value in cancer and lessons from lung fibrosis development. FEBS J. *291*, 4867–4889. https://doi.org/10.1111/febs.17203.

51. Szaruga, M., Janssen, D.A., de Miguel, C., Hodgson, G., Fatalska, A., Pitera, A.P., Andreeva, A., and Bertolotti, A. (2023). Activation of the integrated stress response by inhibitors of its kinases. Nat. Commun. *14*, 5535. https://doi.org/10.1038/s41467-023-40823-8.

52. Eberhardt, J., Santos-Martins, D., Tillack, A.F., and Forli, S. (2021). AutoDock Vina 1.2.0: New docking methods, expanded force field, and Python bindings. J. Chem. Inf. Model. *61*, 3891–3898. https://doi.org/10.1021/acs.jcim.1c00203.

53. Abramson, J., Adler, J., Dunger, J., Evans, R., Green, T., Pritzel, A., Ronneberger, O., Willmore, L., Ballard, A.J., Bambrick, J., et al. (2024). Accurate structure prediction of biomolecular interactions with AlphaFold 3. Nature *630*, 493–500. https://doi.org/10.1038/s41586-024-07487-w.

54. Padyana, A.K., Qiu, H., Roll-Mecak, A., Hinnebusch, A.G., and Burley, S. K. (2005). Structural basis for autoinhibition and mutational activation of eukaryotic initiation factor 2alpha protein kinase GCN2. J. Biol. Chem. *280*, 29289–29299. https://doi.org/10.1074/jbc.M504096200.

55. Romano, P.R., Garcia-Barrio, M.T., Zhang, X., Wang, Q., Taylor, D.R., Zhang, F., Herring, C., Mathews, M.B., Qin, J., and Hinnebusch, A.G. (1998). Autophosphorylation in the activation loop is required for full kinase activity in vivo of human and yeast eukaryotic initiation factor 2α kinases PKR and GCN2. Mol. Cell. Biol. *18*, 2282–2297. https://doi.org/10.1128/MCB.18.4.2282.

56. Jiang, J., Srivastava, S., Seim, G., Pavlova, N.N., King, B., Zou, L., Zhang, C., Zhong, M., Feng, H., Kapur, R., et al. (2019). Promoter demethylation of the asparagine synthetase gene is required for ATF4-dependent adaptation to asparagine depletion. J. Biol. Chem. *294*, 18674–18684. https://doi.org/10.1074/jbc.RA119.010447.

57. Wortel, I.M.N., van der Meer, L.T., Kilberg, M.S., and van Leeuwen, F.N. (2017). Surviving Stress: Modulation of ATF4-mediated stress responses in normal and malignant cells. Trends Endocrinol. Metab. *28*, 794–806. https://doi.org/10.1016/j.tem.2017.07.003.

58. Fusade-Boyer, M., Dupré, G., Bessière, P., Khiar, S., Quentin-Froignant, C., Beck, C., Lecollinet, S., Rameix-Welti, M.A., Eléouët, J.F., Tangy, F., et al. (2019). Evaluation of the antiviral activity of Sephin1 treatment and its consequences on eIF2α phosphorylation in response to viral infections. Front. Immunol. *10*, 134. https://doi.org/10.3389/fimmu.2019.00134.

59. Burnett, H.F., Audas, T.E., Liang, G., and Lu, R.R. (2012). Herpes simplex virus-1 disarms the unfolded protein response in the early stages of infection. Cell Stress Chaperones *17*, 473–483. https://doi.org/10.1007/s12192-012-0324-8.

60. Chen, Y.G., and Hur, S. (2022). Cellular origins of dsRNA, their recognition and consequences. Nat. Rev. Mol. Cell Biol. *23*, 286–301. https://doi.org/10.1038/s41580-021-00430-1.

61. Halford, W.P., Balliet, J.W., and Gebhardt, B.M. (2004). Re-evaluating natural resistance to herpes simplex virus type 1. J. Virol. *78*, 10086–10095. https://doi.org/10.1128/JVI.78.18.10086-10095.2004.

62. Aoki, H., Akaike, T., Abe, K., Kuroda, M., Arai, S., Okamura, R., Negi, A., and Maeda, H. (1995). Antiviral effect of oryzacystatin, a proteinase inhibitor in rice, against herpes simplex virus type 1 in vitro and in vivo. Antimicrob. Agents Chemother. *39*, 846–849. https://doi.org/10.1128/AAC.39.4.846.

63. Carr, D.J.J., Chodosh, J., Ash, J., and Lane, T.E. (2003). Effect of anti-CXCL10 monoclonal antibody on herpes simplex virus type 1 keratitis and retinal infection. J. Virol. *77*, 10037–10046. https://doi.org/10.1128/jvi.77.18.10037-10046.2003.

64. Ghaddar, N., Wang, S., Woodvine, B., Krishnamoorthy, J., van Hoef, V., Darini, C., Kazimierczak, U., Ah-Son, N., Popper, H., Johnson, M., et al. (2021). The integrated stress response is tumorigenic and constitutes a therapeutic liability in KRAS-driven lung cancer. Nat. Commun. *12*, 4651. https://doi.org/10.1038/s41467-021-24661-0.

65. Hetz, C. (2012). The unfolded protein response: controlling cell fate decisions under ER stress and beyond. Nat. Rev. Mol. Cell Biol. *13*, 89–102. https://doi.org/10.1038/nrm3270.

66. Chen, D., Fan, Z., Rauh, M., Buchfelder, M., Eyupoglu, I.Y., and Savaskan, N. (2017). ATF4 promotes angiogenesis and neuronal cell death and confers ferroptosis in a xCT-dependent manner. Oncogene *36*, 5593–5608. https://doi.org/10.1038/onc.2017.146.

67. Baleriola, J., Walker, C.A., Jean, Y.Y., Crary, J.F., Troy, C.M., Nagy, P.L., and Hengst, U. (2014). Axonally synthesized ATF4 transmits a neurodegenerative signal across brain regions. Cell *158*, 1159–1172. https://doi.org/10.1016/j.cell.2014.07.001.

68. Kaufmann, S.H.E., Dorhoi, A., Hotchkiss, R.S., and Bartenschlager, R. (2018). Host-directed therapies for bacterial and viral infections. Nat. Rev. Drug Discov. *17*, 35–56. https://doi.org/10.1038/nrd.2017.162.

69. Kumar, N., Sharma, S., Kumar, R., Tripathi, B.N., Barua, S., Ly, H., and Rouse, B.T. (2020). Host-Directed Antiviral Therapy. Clin. Microbiol. Rev. *33*, e00168-19. https://doi.org/10.1128/CMR.00168-19.

70. Crespillo-Casado, A., Chambers, J.E., Fischer, P.M., Marciniak, S.J., and Ron, D. (2017). PPP1R15A-mediated dephosphorylation of eIF2α is unaffected by Sephin1 or Guanabenz. eLife *6*, e26109. https://doi.org/10.7554/eLife.26109.

71. Drexler, H.C.A. (2009). Synergistic apoptosis induction in leukemic cells by the phosphatase inhibitor salubrinal and proteasome inhibitors. PLoS One *4*, e4161. https://doi.org/10.1371/journal.pone.0004161.

72. Guan, B.J., van Hoef, V., Jobava, R., Elroy-Stein, O., Valasek, L.S., Cargnello, M., Gao, X.H., Krokowski, D., Merrick, W.C., Kimball, S.R., et al. (2017). A unique ISR program determines cellular responses to chronic stress. Mol. Cell *68*, 885–900.e6. https://doi.org/10.1016/j.molcel.2017.11.007.

73. Martinez, N.W., Gómez, F.E., and Matus, S. (2021). The potential role of protein kinase R as a regulator of age-related neurodegeneration. Front. Aging Neurosci. *13*, 638208. https://doi.org/10.3389/fnagi.2021.638208.

74. Kirkland, J.L., and Tchkonia, T. (2020). Senolytic drugs: from discovery to translation. J. Intern. Med. *288*, 518–536. https://doi.org/10.1111/joim.13141.

75. Chaib, S., Tchkonia, T., and Kirkland, J.L. (2022). Cellular senescence and senolytics: the path to the clinic. Nat. Med. *28*, 1556–1568. https://doi.org/10.1038/s41591-022-01923-y.

76. Jost, M., and Weissman, J.S. (2018). CRISPR approaches to small molecule target identification. ACS Chem. Biol. *13*, 366–375. https://doi.org/10.1021/acschembio.7b00965.

77. Knutson, S.D., Buksh, B.F., Huth, S.W., Morgan, D.C., and MacMillan, D.W.C. (2024). Current advances in photocatalytic proximity labeling. Cell Chem. Biol. *31*, 1145–1161. https://doi.org/10.1016/j.chembiol.2024.03.012.

78. Goglia, A.G., Wilson, M.Z., Jena, S.G., Silbert, J., Basta, L.P., Devenport, D., and Toettcher, J.E. (2020). A live-cell screen for altered Erk dynamics reveals principles of proliferative control. Cell Syst. *10*, 240–253.e6. https://doi.org/10.1016/j.cels.2020.02.005.

79. Inglés-Prieto, Á., Reichhart, E., Muellner, M.K., Nowak, M., Nijman, S.M.B., Grusch, M., and Janovjak, H. (2015). Light-assisted small-molecule screening against protein kinases. Nat. Chem. Biol. *11*, 952–954. https://doi.org/10.1038/nchembio.1933.

80. Agus, V., and Janovjak, H. (2017). Optogenetic methods in drug screening: technologies and applications. Curr. Opin. Biotechnol. *48*, 8–14. https://doi.org/10.1016/j.copbio.2017.02.006.

81. Zhao, E.M., Zhang, Y., Mehl, J., Park, H., Lalwani, M.A., Toettcher, J.E., and Avalos, J.L. (2018). Optogenetic regulation of engineered cellular metabolism for microbial chemical production. Nature *555*, 683–687. https://doi.org/10.1038/nature26141.

82. Zhao, E.M., Suek, N., Wilson, M.Z., Dine, E., Pannucci, N.L., Gitai, Z., Avalos, J.L., and Toettcher, J.E. (2019). Light-based control of metabolic flux through assembly of synthetic organelles. Nat. Chem. Biol. *15*, 589–597. https://doi.org/10.1038/s41589-019-0284-8.

83. Zhou, Y., Kong, D., Wang, X., Yu, G., Wu, X., Guan, N., Weber, W., and Ye, H. (2022). A small and highly sensitive red/far-red optogenetic switch for applications in mammals. Nat. Biotechnol. *40*, 262–272. https://doi.org/10.1038/s41587-021-01036-w.

84. Shao, J., Wang, M., Yu, G., Zhu, S., Yu, Y., Heng, B.C., Wu, J., and Ye, H. (2018). Synthetic far-red light-mediated CRISPR-dCas9 device for inducing functional neuronal differentiation. Proc. Natl. Acad. Sci. USA *115*, E6722–E6730. https://doi.org/10.1073/pnas.1802448115.

85. Rosenbloom, A.B., Tarczyński, M., Lam, N., Kane, R.S., Bugaj, L.J., and Schaffer, D.V. (2020). β-Catenin signaling dynamics regulate cell fate in differentiating neural stem cells. Proc. Natl. Acad. Sci. USA *117*, 28828–28837. https://doi.org/10.1073/pnas.2008509117.

86. Lach, R.S., Qiu, C., Kajbaf, E.Z., Baxter, N., Han, D., Wang, A., Lock, H., Chirikian, O., Pruitt, B., and Wilson, M.Z. (2022). Nucleation of the destruction complex on the centrosome accelerates degradation of β-catenin and regulates Wnt signal transmission. Proc. Natl. Acad. Sci. USA *119*, e2204688119. https://doi.org/10.1073/pnas.2204688119.

87. Wilson, M.Z., Ravindran, P.T., Lim, W.A., and Toettcher, J.E. (2017). Tracing information flow from Erk to target gene induction reveals mechanisms of dynamic and combinatorial control. Mol. Cell *67*, 757–769.e5. https://doi.org/10.1016/j.molcel.2017.07.016.

88. Tischer, D., and Weiner, O.D. (2014). Illuminating cell signalling with optogenetic tools. Nat. Rev. Mol. Cell Biol. *15*, 551–558. https://doi.org/10.1038/nrm3837.

89. Qiao, L., Niu, L., Wang, M., Wang, Z., Kong, D., Yu, G., and Ye, H. (2024). A sensitive red/far-red photoswitch for controllable gene therapy in mouse models of metabolic diseases. Nat. Commun. *15*, 10310. https://doi.org/10.1038/s41467-024-54781-2.

90. Wong, F., de la Fuente-Nunez, C., and Collins, J.J. (2023). Leveraging artificial intelligence in the fight against infectious diseases. Science *381*, 164–170. https://doi.org/10.1126/science.adh1114.

91. Wong, F., Krishnan, A., Zheng, E.J., Stärk, H., Manson, A.L., Earl, A.M., Jaakkola, T., and Collins, J.J. (2022). Benchmarking AlphaFold-enabled molecular docking predictions for antibiotic discovery. Mol. Syst. Biol. *18*, e11081. https://doi.org/10.15252/msb.202211081.

92. Sadybekov, A.V., and Katritch, V. (2023). Computational approaches streamlining drug discovery. Nature *616*, 673–685. https://doi.org/10.1038/s41586-023-05905-z.

93. Gardner, T.S., Cantor, C.R., and Collins, J.J. (2000). Construction of a genetic toggle switch in *Escherichia coli*. Nature *403*, 339–342. https://doi.org/10.1038/35002131.

94. Elowitz, M.B., and Leibler, S. (2000). A synthetic oscillatory network of transcriptional regulators. Nature *403*, 335–338. https://doi.org/10.1038/35002125.

95. Nakashima, Y., Ohta, S., and Wolf, A.M. (2017). Blue light-induced oxidative stress in live skin. Free Radic. Biol. Med. *108*, 300–310. https://doi.org/10.1016/j.freeradbiomed.2017.03.010.

96. Ooe, E., Tsuruma, K., Kuse, Y., Kobayashi, S., Shimazawa, M., and Hara, H. (2017). The involvement of ATF4 and S-opsin in retinal photoreceptor cell damage induced by blue LED light. Mol. Vis. *23*, 52–59.

97. Kuse, Y., Ogawa, K., Tsuruma, K., Shimazawa, M., and Hara, H. (2014). Damage of photoreceptor-derived cells in culture induced by light emitting diode-derived blue light. Sci. Rep. *4*, 5223. https://doi.org/10.1038/srep05223.

98. Zhu, S., Li, X., Wu, F., Cao, X., Gou, K., Wang, C., and Lin, C. (2022). Blue light induces skin apoptosis and degeneration through activation of the endoplasmic reticulum stress-autophagy apoptosis axis: Protective role of hydrogen sulfide. J. Photochem. Photobiol. B *229*, 112426. https://doi.org/10.1016/j.jphotobiol.2022.112426.

99. Stringer, C., Wang, T., Michaelos, M., and Pachitariu, M. (2021). Cellpose: a generalist algorithm for cellular segmentation. Nat. Methods *18*, 100–106. https://doi.org/10.1038/s41592-020-01018-x.

100. Hao, Y., Stuart, T., Kowalski, M.H., Choudhary, S., Hoffman, P., Hartman, A., Srivastava, A., Molla, G., Madad, S., Fernandez-Granda, C., et al. (2024). Dictionary learning for integrative, multimodal and scalable single-cell analysis. Nat. Biotechnol. *42*, 293–304. https://doi.org/10.1038/s41587-023-01767-y.

101. Krol, L.R. (2017). Permutation Test. https://github.com/lrkrol/permutationTest.

102. McGinnis, C.S., Patterson, D.M., Winkler, J., Conrad, D.N., Hein, M.Y., Srivastava, V., Hu, J.L., Murrow, L.M., Weissman, J.S., Werb, Z., et al. (2019). MULTI-seq: sample multiplexing for single-cell RNA sequencing using lipid-tagged indices. Nat. Methods *16*, 619–626. https://doi.org/10.1038/s41592-019-0433-8.

103. Martinez Molina, D., Jafari, R., Ignatushchenko, M., Seki, T., Larsson, E.A., Dan, C., Sreekumar, L., Cao, Y., and Nordlund, P. (2013). Monitoring drug target engagement in cells and tissues using the cellular thermal shift assay. Science *341*, 84–87. https://doi.org/10.1126/science.1233606.

104. Ritchie, M.E., Phipson, B., Wu, D., Hu, Y., Law, C.W., Shi, W., and Smyth, G.K. (2015). limma powers differential expression analyses for RNA-sequencing and microarray studies. Nucleic Acids Res. *43*, e47. https://doi.org/10.1093/nar/gkv007.

105. Grøftehauge, M.K., Hajizadeh, N.R., Swann, M.J., and Pohl, E. (2015). Protein-ligand interactions investigated by thermal shift assays (TSA) and dual polarization interferometry (DPI). Acta Crystallogr. D Biol. Crystallogr. *71*, 36–44. https://doi.org/10.1107/S1399004714016617.

106. Wu, T., Hornsby, M., Zhu, L., Yu, J.C., Shokat, K.M., and Gestwicki, J.E. (2023). Protocol for performing and optimizing differential scanning fluorimetry experiments. Star Protoc. *4*, 102688. https://doi.org/10.1016/j.xpro.2023.102688.

107. Sishtla, K., Lambert-Cheatham, N., Lee, B., Han, D.H., Park, J., Sardar Pasha, S.P.B., Lee, S., Kwon, S., Muniyandi, A., Park, B., et al. (2022). Small-molecule inhibitors of ferrochelatase are antiangiogenic agents. Cell Chem. Biol. *29*, 1010–1023.e14. https://doi.org/10.1016/j.chembiol.2022.01.001.

108. Morris, G.M., Huey, R., Lindstrom, W., Sanner, M.F., Belew, R.K., Goodsell, D.S., and Olson, A.J. (2009). AutoDock4 and AutoDockTools4: Automated docking with selective receptor flexibility. J. Comput. Chem. *30*, 2785–2791. https://doi.org/10.1002/jcc.21256.

109. Fujimoto, J., Kurasawa, O., Takagi, T., Liu, X., Banno, H., Kojima, T., Asano, Y., Nakamura, A., Nambu, T., Hata, A., et al. (2019). Identification of novel, potent, and orally available GCN2 inhibitors with type I half binding mode. ACS Med. Chem. Lett. *10*, 1498–1503. https://doi.org/10.1021/acsmedchemlett.9b00400.

Please cite this article in press as: Wong et al., Optogenetics-enabled discovery of integrated stress response modulators, Cell (2025), https://doi.org/10.1016/j.cell.2025.06.024

STAR★METHODS

KEY RESOURCES TABLE

REAGENT or RESOURCE	SOURCE	IDENTIFIER
Antibodies		
Rabbit anti-ATF4	Cell Signaling Technology	11815; RRID: AB_2616025
Mouse anti-ATF4	Cell Signaling Technology	97038; RRID: AB_3698388
Mouse anti-CHOP	Cell Signaling Technology	2895; RRID: AB_2089254
Rabbit anti-peIF2α	Abcam	ab32157; RRID: AB_732117
Goat anti-rabbit 633 IgG	Invitrogen	A21070; RRID: AB_10562894
Goat anti-mouse 555 IgG	Invitrogen	A28180; RRID: AB_2536164
Bacterial and virus strains		
Herpes simplex virus type 1 (HSV-1) strain KOS	ATCC	VR-1493
Zika virus (ZKV) strain MR766	ATCC	VR-1838
Respiratory syncytial virus (RSV) strain B WV/14617/85	ATCC	VR-1400
NEB® Stable Competent *E. coli*	New England Biolabs	C3040H
Salmonella typhimurium	Environmental Bio-Detection Products, Inc.	TA100
Biological samples		
Whole human blood containing EDTA	Innovative Research	IWB1K2E
Chemicals, peptides, and recombinant proteins		
trans-ISRIB	Cayman Chemical Company	16258
2BAct	Cayman Chemical Company	37788
Thapsigargin	Cayman Chemical Company	10522
Sodium (meta)arsenite	MilliporeSigma	S7400
Salubrinal	MedChemExpress	HY-15486
GCN2iB	MedChemExpress	HY-112654
B/B homodimerizer	Takara Bio	635058
Resazurin	MilliporeSigma	R7017
IBX-200	Specs	AQ-750/42050411
IBX-201	Life Chemicals	F3394-0752
IBX-202	Specs	AG-205/33143033
IBX-203	Specs	AM-807/43366104
IBX-204	ChemDiv	L759-0883
IBX-205	ChemDiv	L759-0059
IBX-206	ChemDiv	L759-0764
IBX-207	ChemDiv	L759-0208
IBX-210	Vitas-M	STK694918
IBX-211	ChemBridge	6080233
IBX-212	ChemDiv	L759-0201
EIF2AK3 Recombinant Protein (Human)	Aviva Systems Biology	OPED00115
SMAD3 Protein, Human (Flag-His)	MedChemExpress	HY-P71323
Protein Phosphatase-1 (PP1) Catalytic Subunit, α-Isoform from rabbit	MilliporeSigma	P7937
Human EIF2AK4 (aa192-1024)	MilliporeSigma	14-934
Critical commercial assays		
Click-&-Go Plus 647 OPP kit	VectorLabs	CCT-1496
ROS detection kit	Cayman Chemical Company	601520

(*Continued on next page*)

Please cite this article in press as: Wong et al., Optogenetics-enabled discovery of integrated stress response modulators, Cell (2025), https://doi.org/10.1016/j.cell.2025.06.024

Continued

REAGENT or RESOURCE	SOURCE	IDENTIFIER
ATP detection kit	Cayman Chemical Company	700410
PIPseq 3' Single Cell 3' RNA kit	Fluent Biosciences	T20
NEBNext Library Quant Kit for Illumina	New England Biolabs	E7630S
EIF2AK1 (HRI) Kinase Enzyme System	Promega	VA7132
EIF2AK2 kinase assay kit	BPS Biosciences	78433
EIF2AK4 Kinase Enzyme System	Promega	VA7438
CETSA	Pelago Biosciences	Standard Selectivity Profiling
Protein Thermal Shift Starter Kit	Applied Biosystems	4462263
CRISPRMAX Cas9 PLUS reagent	Invitrogen	CMAX00001
AlphaLISA SureFire Ultra Human Phospho-GCN2 (Thr899) Detection Kit	Revvity	ALSU-PGCN2-A500
AlphaLISA SureFire Ultra Human Total GCN2 Detection Kit	Revvity	ALSU-TGCN2-A500
AlphaLISA SureFire Ultra Human Total PKR Detection Kit	Revvity	ALSU-TPKR-A500
Mouse IP-10 (CXCL10) ELISA Kit	Invitrogen	BMS6018
5041 Modified Ames ISO kit	Environmental Bio-Detection Products, Inc.	5041
Alanine Transaminase Colorimetric Activity Assay Kit	Cayman Chemical Company	700260
Aspartate Aminotransferase Colorimetric Activity Assay Kit	Cayman Chemical Company	701640
Experimental models: Cell lines		
Human: H4 cells	ATCC	HTB-148
Human: H4 Cry2Olig-PKR cells	Batjargal et al.[22]	Opto-PKR
Human: H4 mCherry-DmrB-PKR cells	This work	Chem-PKR
Human: IMR-90 cells	ATCC	CCL-186
Monkey: Vero cells	ATCC	CCL-81
Experimental models: Organisms/strains		
Mouse: C57BL/6J	The Jackson Laboratory	000664
Mouse: C57BL/6J	Charles River Laboratories	027C57BL/6
Software and algorithms		
RDKit ver. 2023.09.1	GitHub	https://rdkit.org/
MATLAB R2023b	Mathworks	https://www.mathworks.com/products/matlab.html
Cellpose	Stringer et al.[99]	https://www.cellpose.org/
BaseSpace	Illumina	https://basespace.illumina.com/
PIPSeeker	Fluent Biosciences	https://www.fluentbio.com/products/pipseeker-software-for-data-analysis/
R ver. 4.4.2	The R Project for Statistical Computing	https://www.r-project.org/
Seurat ver. 5	Hao et al.[100]	https://satijalab.org/seurat/
AutoDock Vina ver. 1.2.0	Eberhardt et al.[52]	https://github.com/ccsb-scripps/AutoDock-Vina
PyMOL ver. 2.5.7	Schrödinger	https://www.pymol.org/
Permutation test	Krol[101]	https://github.com/lrkrol/permutationTest

EXPERIMENTAL MODEL AND STUDY PARTICIPANT DETAILS

Cell culture

Opto-PKR H4, H4 (ATCC HTB-148; human epithelial cells from the brain of a 37-year-old, White male with neuroglioma), IMR-90 (ATCC CCL-186; human fibroblasts from the normal lung tissue of a 16-week-old female), and Vero (ATCC CCL-81; epithelial cells

from the kidney of a female African green monkey) cells, passaged <10 times, were grown to log phase in complete media comprising high-glucose Dulbecco's Modified Eagle Medium (DMEM; Corning 10-013-CV) supplemented with 10% fetal bovine serum (ThermoFisher 16140071) and 1% penicillin-streptomycin (ThermoFisher 15070063). Cells were authenticated by the supplier, ATCC, using STR profiling. Cells were cultured at 37°C and 5% CO_2 in humidity-controlled incubators.

Viral culture

Herpes simplex virus type 1 (HSV-1) strain KOS, Zika virus (ZKV) strain MR766, and respiratory syncytial virus (RSV) strain B WV/14617/85 were from ATCC (VR-1493, VR-1838, and VR-1400). These viruses were authenticated by the supplier, ATCC, using next-generation sequencing or Sanger sequencing. Viruses were propagated using Vero cells in T-75 flasks. Cells were infected by adding 0.5 mL of virus to 4 mL of complete growth media and incubating for 1.5 to 2 h, with shaking every 20 to 30 min. Complete growth media was then added to the viral supernatant for a total volume of 15 mL per flask. HSV-1- and ZKV-infected cells were incubated for 3 d at 37°C and 5% CO_2 and RSV-infected cells were incubated for 9 d at 37°C and 5% CO_2 before virus collection. On the day of collection, the supernatant was collected, centrifuged at 150*g* for 10 min to remove cellular debris, aliquoted, and stored at -80°C before further use.

Mouse models

The in vivo portion of the herpesvirus mouse model was performed at NeoSome Life Sciences, approved by the NeoSome IACUC, and according to NeoSome IACUC policies and guidelines as well as OLAW standards. Female C57BL/6J mice, 8-12 weeks old, 19-24 g, and received from The Jackson Laboratory (strain 000664), were acclimated for 5 days prior to the start of study. Animals were housed 5 per cage with free access to food and water and in a temperature- and humidity-controlled room with a 12-hour light cycle. Mice were individually identified through tail marking prior to weighing and dosing and were randomly assigned to experimental groups. The in vivo portion of the mouse experiment measuring AST/ALT was performed at Integrated Biosciences' Charles River Laboratories facilities, approved by the Charles River IACUC, and according to Charles River IACUC policies and guidelines as well as OLAW standards. Female C57BL/6J mice, 8-12 weeks old, 19-24 g, and received from Charles River Laboratories, were acclimated for at least 5 days prior to the start of study. Animals were housed 5 per cage with free access to food and water and in a temperature- and humidity-controlled room with a 12-hour light cycle. Mice were randomly assigned to experimental groups.

METHOD DETAILS

Construction of opto-PKR cells

Opto-PKR-bearing H4 neuroglioma cells were constructed, sorted, and characterized using Cry2Olig-PKR as previously described.[22] Cells were validated to contain opto-PKR by observing that citrine fluorescent clusters formed when cells were exposed to blue light for time intervals >30 min, using the illumination and imaging systems described below. Of note, we previously reported the generation and characterization of several stable, sorted cell lines expressing different optogenetic tools, including variants of Cry2 (e.g., Cry2Olig, Cry2Olig-clust, and Cry2Olig-drop).[22] Of these, we previously found that Cry2Olig-bearing cells exhibited high expression levels and the largest size and number of opto-PKR condensates per cell.[22] In the present study, we have leveraged the Cry2Olig construct due to its high expression and effectiveness at inducing opto-PKR condensates.

Illumination system for optogenetics

To enable the high-throughput screen described in the main text, blue light-emitting illumination rigs were custom-fabricated. Aluminum sheet metal was cut and fitted to house 15" × 15" × 1.5" 22-watt blue LED panels (Yescom). White acrylic sheets (KlearStand) were used as diffusers, and electrical input was controlled using a Korad KD3005D digital-control DC power supply. An LT45 LED light meter (Extech Instruments) was used to measure and calibrate the intensity of the light output. For our experiments, ~10 lux was used.

Chemical compounds

Known ISR modulators were compiled from a literature search, as tabulated in Data S1, and sourced from commercial vendors including MedChemExpress and Cayman Chemical Company. The screening library of 370,830 compounds was custom assembled at Integrated Biosciences, Inc., and includes previously described libraries[32–34,91] as well as commercially available compounds. Anonymous graphs for high-throughput screening hits that putatively potentiate the ISR, as described in this work, are provided in Data S1. All compounds were solubilized in DMSO (MilliporeSigma D2650) at concentrations ≥2 mM, and final DMSO concentrations across all experiments were ≤1%.

Immunofluorescence staining and imaging

Protein synthesis was measured using a Click-&-Go Plus 647 kit (VectorLabs CCT-1496). Briefly, black glass-bottom plates (Cellvis) were coated with fibronectin (ThermoFisher 33010018) in DPBS at 10 μg/cm^2, and cells were plated, allowed to adhere overnight, and treated using the indicated compounds for the indicated times, after which o-propargyl-puromycin (OPP) reagent was added to a final concentration of 20 μM. Cells were then incubated with OPP reagent for an additional 30 min, washed once with DPBS, fixed

Please cite this article in press as: Wong et al., Optogenetics-enabled discovery of integrated stress response modulators, Cell (2025), https://doi.org/10.1016/j.cell.2025.06.024

in 4% paraformaldehyde (pH 7.4 in DPBS) for 20 min, washed once with DPBS, and permeabilized for 1 hour at room temperature with blocking buffer comprising 0.05% saponin (MilliporeSigma 47036), 0.5% bovine serum albumin (MilliporeSigma A7030), 50 mM ammonium chloride (MilliporeSigma A9434), and 0.02% sodium azide (MilliporeSigma S2002) in DPBS (pH 7.4). The blocking buffer was then aspirated, and where relevant, cells were incubated with primary antibodies overnight (18-24 h) in blocking buffer, then washed three times in DPBS. Cells were next incubated for 1 hour in blocking buffer containing DAPI (1 μg/mL) and, where relevant, secondary antibodies. Cells were then washed twice in DPBS and stained for 45 min in the dark at room temperature with OPP staining cocktail comprising OPP reaction buffer, copper catalyst, AZDye Azide Plus solution, and reducing agent (sodium ascorbate). Finally, cells were washed once in OPP wash buffer and twice in DPBS and kept in PBS-T in the dark for subsequent imaging. Experiments involving only immunofluorescence staining and not OPP staining (as shown in Figures 1, 4, S1, S3, and S4) were performed as described above, but without the OPP steps. Imaging was performed using a Yokogawa CQ1 confocal quantitative image cytometer. Antibodies used include rabbit anti-ATF4 (Cell Signaling 118155), mouse anti-CHOP (Cell Signaling 2895), rabbit anti-peIF2α (Abcam ab32157), goat anti-rabbit 633 IgG (Invitrogen A21070), and goat anti-mouse 555 IgG (Invitrogen A28180). Primary antibodies were used at 1:400 final dilution; secondary antibodies were used at 1:800 final dilution.

Image analysis and quantification

Fluorescent images were acquired using a Yokogawa CQ1 confocal quantitative image cytometer equipped with 10×, 20×, and 40× objectives. All analyzed images were segmented, measured, processed, and plotted using context-specific Python and MATLAB-based pipelines. Briefly, raw images containing segmentation markers (DAPI) were segmented using Cellpose,[99] and information from the resulting objects was used to measure indicated signals of interest from orthogonal channels. Unless otherwise noted, each individual cell measurement is a raw mean fluorescent intensity value of all foreground pixels for the segmented object and channel. Population statistics (mean, standard error of the mean, and number of cells) were calculated from object mean fluorescent intensity values, and final measurements were compiled using MATLAB.

Cheminformatics, t-SNE, and similarity

RDKit, a Python package for chemical analysis, was used for all computational analyses in this work, including calculation of the chemical properties shown in Table S1. The anonymous graphs provided in Data S1 were calculated using RDKit's Chem.rdMolHash.MolHash function; each anonymous graph refers to the canonical SMILES string for a molecule after setting all of its atoms to asterisks and its bonds to single bonds. t-SNE and Tanimoto similarity analyses were performed on Morgan fingerprints using 2048 as the number of bits and 2 as the fingerprint radius. For t-SNE, PCA initialization and a perplexity parameter of 30 were used. Ninety-one compounds from the screening library, including peptide-like compounds and compounds with no available SMILES, were excluded from the visualization.

High-throughput screening

Cells were plated into either (1) 96-well clear flat-bottom black tissue-culture-treated plates (Corning 3603) at a density of 10^4 cells/well using 100 μL working volumes or (2) 384-well clear flat-bottom black tissue-culture-treated plates (Corning 3764) at a density of 5,000 cells/well using 30 to 80 μL working volumes, where each plate contained a pre-aliquoted volume of test compounds such that the final concentration of compound was 10 μM (final DMSO concentration of 0.5%). Cells were then incubated at 37°C with 5% CO_2 for 24 hours using the optogenetic illumination system (H4 cells) or for 72 hours without optogenetic illumination (IMR-90 cells), after which cytotoxicity was assayed using a resazurin (alamarBlue) assay. Resazurin (MilliporeSigma R7017) was added to each well to a final concentration of 0.15 mM. After an additional 24 hours of incubation, the fluorescence excitation/emission at 520/580-640 nm or 550/590 nm was read using a Promega GloMax plate reader or an EnVision plate reader (PerkinElmer), respectively. For IMR-90 cytotoxicity, data for a subset of 39,312 compounds, corresponding to the library used to screen for growth inhibition against *Staphylococcus aureus* in previous work from our lab,[33] have previously been generated by us; as the experimental conditions of the screen are similar to those considered here, these data were used and expanded upon for the current IMR-90 dataset in lieu of screening the same subset of compounds again. All other compounds were screened for cytotoxicity against IMR-90 cells as described above. Plate data were normalized by the interquartile mean of each plate to calculate relative cell viability. All screens were performed once (i.e., no biological replicates). After defining hit criteria as described in the main text, 3,599 shortlisted compounds were validated by repeating the above experiment in biological duplicate for opto-PKR H4 cells.

Cellular viability assay

Opto-PKR H4 cells were cultured as described above and seeded at a density of ~1×10^4 cells/well into 96-well clear flat-bottom black tissue-culture-treated plates. For each compound, 0.5 or 1 μL of two-fold serial dilutions in DMSO was added to 99.5 or 99 μL of medium containing cells. Matched plates were separately incubated in light (using the optogenetic illumination system described above) or in complete dark (wrapped in aluminum foil) at 37°C with 5% CO_2 for 24 h. Cellular viability was then determined similarly to the above, with resazurin incubation for 4 to 24 h, and viability values were normalized by the average of at least two DMSO vehicle-treated values to calculate relative cell viability. For compound dose-response experiments, we used nonlinear least-squares fitting (the lsqcurvefit function in MATLAB, ver. R2023b) to fit relative cellular viability values to Hill functions of the form

$$H(x) = b_0 + \frac{mx^{\beta}}{x_{0.5}^{\beta} + x^{\beta}}.$$

EC_{50} values were determined by numerically solving the best-fit Hill function for x given that $H(x)$ is equal to the half-maximal value. Cellular viability assays determining the CC_{50} values of compounds against other cell types were performed similarly, but with all cells incubated under ambient light conditions (i.e., without optogenetic illumination or wrapping in aluminum foil) for 3 days.

Halofuginone with light pre-exposure

Opto-PKR cells were plated on 96-well clear flat-bottom black tissue-culture-treated plates as above and incubated in light (using the optogenetic illumination system described above) or in complete dark (wrapped in aluminum foil) at 37°C with 5% CO_2 for 24 h. Halofuginone was then added to the final concentrations indicated, and cells were again incubated in light or in complete dark at 37°C with 5% CO_2 for another 24 h. Cellular viability was then determined similarly to the above, with resazurin incubation for 24 h, and viability values were normalized by DMSO vehicle-treated values to calculate relative cell viability.

True stressor experiments

Wild-type H4 cells (not containing opto-PKR) were plated on black 96-well clear-bottom plates and treated with the indicated compounds at the indicated concentrations. Stock solutions of compounds were prepared such that the final concentration of DMSO in all experiments was 1%, a concentration small enough to not confound decreases in cell viability. Cells were incubated at 37°C with 5% CO_2 under ambient light conditions (i.e., without optogenetic illumination or wrapping in aluminum foil). After 24 hours of incubation, resazurin was added, and cell viability was measured as described above. Cell viability values were normalized with respect to values from treatment with vehicle only (no compound and no stressor).

Construction of chem-PKR cells

To generate the Chem-PKR construct, we first obtained the DNA encoding the C-terminal PKR linker and kinase domain, excluding the dsRNA binding domains (dsRBD1 and dsRBD2) from the previously published vector pHR-Citrine-Cry2Olig-PKR.[22] Briefly, total plasmid DNA from pHR-Citrine-Cry2Olig-PKR was isolated using a midi-prep kit (Qiagen 12143), and the PKR linker and kinase domain sequence was amplified by PCR with primers containing suitable restriction sites for downstream cloning. The amplified fragment was then purified, digested, stitched to an mCherry-tagged DmrB homodimerization domain in-frame with the PKR kinase domain using Gibson assembly, so that the DmrB doman is N-terminal to the PKR kinase domain. DmrB was chosen for its ability to dimerize upon addition of the B/B homodimerizer AP20187. After Gibson Assembly, the resultant construct was transformed into chemically competent *E. coli* (NEB Stable Competent *E. coli*, New England Biolabs C3040H). Positive clones were selected on antibiotic-containing plates and verified by restriction digest analysis. Plasmids from positive clones were further confirmed by whole-plasmid nanopore sequencing (Plasmidsaurus) to ensure fidelity of the PKR linker and kinase domain, as well as correct insertion of mCherry and the DmrB homodimerization domain.

Lentiviral particles were generated following a standard second- or third-generation packaging system. Briefly, Lenti-X 293T cells were seeded in 10-cm dishes and co-transfected with the following plasmids using a calcium phosphate or lipid-based reagent (Lipofectamine 2000; ThermoFisher 11668027):

1 Transfer plasmid: mCherry-DmrB-PKR (chem-PKR) construct.
2 Packaging plasmid: psPAX2 (for viral gag/pol genes).
3 Envelope plasmid: pMD2.G (encoding VSV-G envelope protein).

Forty-eight hours post-transfection, the lentiviral-containing supernatant was collected, clarified by low-speed centrifugation (500*g* for 5 minutes), and filtered through a 0.45-μm filter to remove debris. The viral supernatant was either used immediately or concentrated (via a commercial Lenti-X concentrator kit from Takara Bio) before transduction.

To establish stable Chem-PKR cell lines, cells (wild-type H4 cells) were seeded at ~30-40% confluence in 6-well plates. Viral supernatant containing the chem-PKR construct was added to the cells at the desired multiplicity of infection. Polybrene (8 μg/mL) was included to improve infection efficiency. Plates were gently agitated to ensure even distribution of viral particles and then incubated at 37°C with 5% CO_2 for 16-24 hours. After viral transduction, fresh complete growth medium was added. Approximately 48 hours post-transduction, selection for stably transduced cells was initiated via addition of 2 μg/ml puromycin for 5 days. Cells that exhibited positive mCherry fluorescence were expanded to generate stable pseudo-clonal populations. Expression of the chem-PKR fusion protein was confirmed by fluorescence microscopy (using the mCherry signal).

Chem-PKR activation

To induce dimerization of the DmrB domain and activate the PKR kinase domain in stably transduced cells, the B/B homodimerizer AP20187 (Takara Bio 635058) was added to the culture medium at the indicated concentration. This small molecule drives the dimerization of DmrB domains, bringing the PKR kinase domains into proximity. The resulting autophosphorylation event on PKR leads to phosphorylation of eIF2α and subsequent activation of the ISR.

Please cite this article in press as: Wong et al., Optogenetics-enabled discovery of integrated stress response modulators, Cell (2025), https://doi.org/10.1016/j.cell.2025.06.024

Reactive oxygen species detection

Wild-type H4 cells were plated on black 96-well clear-bottom plates and treated with the indicated compounds at the indicated concentrations. Cells were incubated as described above in "True stressor experiments," after which ROS was detected using a 2,7-dichlorofluoroscin diacetate-based ROS detection kit from Cayman Chemical Company (product 601520) following the manufacturer's instructions. Fluorescence excitation/emission at 520/580-640 nm was read using a Promega GloMax plate reader, and values were inferred by linear interpolation with respect to the provided positive and negative controls. Values were normalized by corresponding total protein concentrations, as described below.

Cellular ATP detection

Wild-type H4 cells were plated on black 96-well clear-bottom plates and treated with the indicated compounds at the indicated concentrations. Cells were incubated as described above in "True stressor experiments," after which cells were lysed and ATP was detected using a firefly luciferase-based ATP detection kit from Cayman Chemical Company (product 700410) following the manufacturer's instructions. Luminescence was read using a Promega GloMax plate reader, and ATP values were inferred by linear interpolation with respect to the provided standard curve. The ATP value of each sample was normalized by the sample's protein concentration. Protein concentrations were determined using a Coomassie Plus protein quantification assay (ThermoFisher 1856210) following the manufacturer's instructions, and by interpolating absorbance (optical density at 600 nm) values with respect to those from the standard curve. Absorbance values were measured using a Promega GloMax plate reader.

Single-cell transcriptomics

Single-cell transcriptomic measurements were collected using a combination of MULTI-seq cell hashing[102] and the PIPseq T20 3' Single Cell 3' RNA kit (Fluent Biosciences) according to the manufacturer's instructions. Briefly, cells were seeded at 1.0×10^4 cells/well, allowed to adhere overnight, and treated with compounds for the indicated durations at the indicated final concentrations the following morning. Prior to pooling, arrayed hashing oligonucleotides were added to live cells on ice and washed three times while adhered. Cells were then trypsinized, pooled, and counted to obtain the desired concentration of input sample for library preparation. Sequencing-ready libraries generated using the PIPseq protocol were assessed for quality and concentration using automated electrophoresis run on a 4200 TapeStation (Agilent); qPCR was performed using the NEBNext Library Quant Kit for Illumina (New England Biolabs E7630S). Libraries were considered high quality if TapeStation traces showed normal distributions centered at ~400 bp and ~250 bp for gene expression and hashtag oligonucleotide fractions, respectively. Dual-indexed libraries were pooled and sequenced using an Illumina NextSeq 2000. Initial sample demultiplexing was done using Illumina BaseSpace, while cell hashing demultiplexing was performed using the PIPSeeker software (Fluent Biosciences). Raw demultiplexed matrices were subsequently processed to generate plots and perform statistical tests using custom R (ver. 4.4.2) pipelines and Seurat ver. 5.[100]

HRI kinase assay

Measurements of reconstituted PERK, PKR, HRI, and protein phosphatase 1 (PP1) enzymatic activity suggested that the compounds did not target these proteins (Figures S4A–S4D). Briefly, compounds were tested for binding activity against purified recombinant HRI using the EIF2AK1 (HRI) Kinase Enzyme System from Promega (product number VA7132) and following the manufacturer's instructions. Standard curves were generated from wells with 1× protein, 0.5× protein, 0.25× protein, and 0× protein. Rottlerin was included as a positive control for inhibition, and DMSO vehicle was used as a negative control. Following manufacturer's instructions, 5 ng protein, 10 μM ATP, and 0.2 μg/μL RS repeat peptide were used per well of a white opaque flat-bottom 384-well plate, and reaction plates were incubated at room temperature for 40 min followed by addition of ADP-Glo, a subsequent incubation at room temperature for 40 min, addition of kinase detection reagent, and a final incubation at room temperature for 30 min. Luminescence was read using a Promega GloMax plate reader, and relative activity values were calculated by linear interpolation with respect to standards.

PKR kinase assay

Compounds were tested for binding activity against purified recombinant PKR using the EIF2AK2 kinase assay kit from BPS Biosciences (product number 78433) and following the manufacturer's instructions. Standard curves were generated from wells with 1× protein, 0.5× protein, 0.25× protein, and 0× protein. C16 was included as a positive control for inhibition, and DMSO vehicle was used as a negative control. Following manufacturer's instructions, 12.5 ng protein was used per well of a white opaque flat-bottom 384-well plate, and reaction plates were incubated at room temperature for 45 min followed by addition of ADP-Glo, a subsequent incubation at room temperature for 45 min, addition of kinase detection reagent, and a final incubation at room temperature for 45 min. Luminescence was read using a Promega GloMax plate reader, and relative activity values were calculated by linear interpolation with respect to standards.

PERK kinase assay

Compounds were tested for binding activity against purified recombinant PERK using EIF2AK3 Recombinant Protein (Human) from Aviva Systems Biology (product number OPED00115), SMAD3 protein, and ADP-Glo from Promega (product number V6930). Briefly, recombinant protein was resuspended in PBS containing 50% glycerol and 0.09% sodium azide. SMAD3 protein was diluted in

50 mM Tris-HCl (pH 7.5), 150 mM NaCl, 10 mM glutathione, 0.1 mM EDTA, 0.25 mM DTT, 0.1 mM PMSF, and 25% glycerol. Kinase buffer comprising 40 mM Tris-HCl (pH 7.5), 20 mM $MgCl_2$, 0.1 mg/mL BSA, and 50 μM of fresh DTT was used. Standard curves were generated from wells with 1× protein, 0.5× protein, 0.25× protein, and 0× protein. DMSO vehicle was used as a negative control. Here, 50 ng protein, 10 μM ATP, and 125 ng SMAD3 protein were used in 5 μL reaction volumes per well of a white opaque flat-bottom 384-well plate, and reaction plates were incubated at room temperature for 40 min followed by addition of 5 μL ADP-Glo, a subsequent incubation at room temperature for 40 min, addition of 10 μL kinase detection reagent, and a final incubation at room temperature for 30 min. Luminescence was read using a Promega GloMax plate reader, and relative activity values were calculated by linear interpolation with respect to standards.

GCN2 kinase assay

Compounds were tested for binding activity against purified recombinant GCN2 using the EIF2AK4 Kinase Enzyme System from Promega (product number VA7438) and following the manufacturer's instructions. Standard curves were generated from wells with 1× protein, 0.5× protein, 0.25× protein, and 0× protein. GCN2iB was used as a positive control for inhibition, and DMSO vehicle was used as a negative control. Following manufacturer's instructions, 50 ng protein, 10 μM ATP, and 0.2 μg/μL RS repeat peptide were used per well of a white opaque flat-bottom 384-well plate, and reaction plates were incubated at room temperature for 40 min followed by addition of ADP-Glo, a subsequent incubation at room temperature for 40 min, addition of kinase detection reagent, and a final incubation at room temperature for 30 min. Luminescence was read using a Promega GloMax plate reader, and relative activity values were calculated by linear interpolation with respect to standards.

PP1 enzymatic assay

Protein Phosphatase-1 (PP1) Catalytic Subunit, α-Isoform from rabbit from MilliporeSigma (product number P7937) and 4-nitrophenyl phosphate (pNPP) di(tris) salt (MilliporeSigma N3254) were combined in phosphatase buffer comprising 100 mM Tris-HCl (pH 7.5), 4 mM DTT, 0.2 mM EDTA, 0.5 mL $MnCl_2$, and 0.4 mg/mL BSA. One hundred μL of reaction volume were used per well of a flat, clear-bottom 96-well plate, with final concentrations of ~1 U/mL PP1 and 40 mM pNPP. Reactions were incubated in the dark at room temperature for 30 minutes, after which absorbance at 405 nm was read using a Promega GloMax plate reader. Standard curves were generated from wells with 1× PP1, 0.5× PP1, 0.25× PP1, and 0× PP1 concentrations, and relative activity values were calculated by linear interpolation with respect to standards. Here, the highest tested concentration of compounds was 50 μM in order to prevent the confounding effects of absorbance interference.

CETSA selectivity profiling assay

The assay was performed by Pelago Biosciences. Briefly, stock solutions of 50 μL in DMSO at 10 mM of IBX-200, IBX-202, and IBX-204 were provided to Pelago Biosciences. Compounds and DMSO vehicle were incubated with proprietary lysates stemming from a human suspension cancer cell line. After CETSA,[103] the supernatant was subjected to quantitative MS analysis. Compound-induced changes in apparent thermal stability on the global proteomes were reported, with each compound treatment performed in triplicate. Shifts in protein abundance were $\log_2$-transformed and normalized across treatments and replicates. For every treatment, apparent thermal stability shifts (ΔS) were estimated as $\log_2$-transformed fold changes relative to the average vehicle control. The moderated *t*-test implemented in the limma R package[104] was used to estimate significance (*p*- and *q*-value) of observed thermal stability changes. These experiments suggested only GPX4, NQO1, GOLGA2, and FECH as potential binding interactions for IBX-200, no potential binding interactions for IBX-202, and only GPX4 and FECH for IBX-204. As IBX-202 chemically converts into an IBX-200 analog and IBX-200 and IBX-204 induced similar ISR-related phenotypes, we focused on the two shared potential binding interactions of IBX-200 and IBX-204 with GPX4 and FECH.

Differential scanning fluorimetry

Thermal shift assays were performed to evaluate the binding of IBX-200, IBX-202, and IBX-204 to GPX4, FECH, and GCN2 using the Applied Biosystems Protein Thermal Shift kit (ThermoFisher 4462263). Since small molecule binding may affect protein stability, changes in the protein unfolding temperature in the presence versus absence of ligands can be used to assess binding affinity.[105,106] Human GPX4 (BPS Biosciences), EIF2AK4 (GCN2 aa192-1024; MilliporeSigma 14-934), and FECH (aa55-423; LS Bio LS-G24888) were freshly solubilized in aqueous buffer. Compounds were added to wells at the indicated final concentrations. FECH and GPX4 were used at a final concentration of 2 μM, while GCN2 was used at 0.4 μM. Five μL of buffer, 12.5 μL of the protein-ligand mixture (at final concentrations as above), and 2.5 μL of dye were added to each well of a 384-well PCR plate, and the resulting solution was mixed thoroughly. Plates were centrifuged at 800 *g* for 1 min, after which the assay was run on a QuantStudio 7 Pro PCR system (ThermoFisher). The following manufacturer-recommended thermal profile was used: step 1: ramp at 1.6 °C/s to 25 °C and hold for 2 min; step 2: ramp at 0.05 °C/s to 99 °C, then hold at 99 °C for 2 min. Fluorescence was recorded during the run, and data analysis was performed using a custom MATLAB script. Thermal shift curves (plots of fluorescence intensity vs. temperature) and their first derivatives vs. temperature were plotted to determine the melting temperatures (T_m), defined here as the temperatures where the first derivatives of fluorescence vs. temperature are maximal. FECH curves were degenerate and did not show increases in fluorescence with temperature (Figure S4F). Protein-ligand pairs where the maximal absolute values of T_m across different compound concentrations were substantially <1°C, a typical hit threshold,[106] were deemed non-binding in this assay (IBX-200 and GPX4,

Please cite this article in press as: Wong et al., Optogenetics-enabled discovery of integrated stress response modulators, Cell (2025), https://doi.org/10.1016/j.cell.2025.06.024

IBX-204 and GPX4, and IBX-200 and GCN2). In particular, these results suggested lack of strong binding for IBX-200 and IBX-204 to GPX4 and are inconclusive for FECH.

GPX4 and FECH studies

A GPX4 Fluorogenic Assay Kit (BPS Biosciences 82165) was used to test enzymatic activity of GPX4 following manufacturer instructions. Compounds were added at the indicated final concentrations. A FECH enzymatic activity assay was performed following previous work.[107] Briefly, FECH protein was reconstituted in 100 mM Tris-HCl, pH 8.0, containing 0.05% octyl glucoside. Five μL of a 100 μM NiCl solution (MilliporeSigma 339350), 5 μL of a 100 μM mesoporphyrin IX solution (MedChemExpress HY-W073074) prepared in ammonium hydroxide, and 5 μL of a 0.75 μM FECH solution was incubated with the specified compounds at the specified final concentrations in buffer on clear, flat-bottom 384-well plates (Corning 3680). Reactions were incubated at room temperature, and FECH activity was monitored by the formation of Ni^{2+}-mesoporphyrin IX via absorbance at 550 nm. FECH activity was calculated based on linear interpolation with respect to a standard curve in which the concentration of FECH protein was titrated. For pharmacologic modulation experiments, four known GPX4 inhibitors—liproxstatin-1 (Cayman Chemical Company 17730), GPX4 inhibitor 26a (Cayman 35408), ML-210 (Cayman 23282), and ML-162 (Cayman 20455) and one known FECH inhibitor (ChemDiv D351-0141), were solubilized in DMSO and added in dose-reponse format to opto-PKR cells for determination of effects on cell viability, as described above in "Cellular viability assay." Hemin chloride (Cayman 16487) was solubilized in PBS and added to IBX-200- and IBX-204-treated opto-PKR cells for determination of effects on cell viability, as described above in "Cellular viability assay." DMSO or PBS vehicle treatment was included.

Chemical conversion of IBX-202

Upon further investigation of the chemical structure of IBX-202, we noticed the possibility of ring closure to form a bicyclic ring system resembling that of IBX-200 (Figure S4I). To validate this, we performed chemical analysis experiments in which IBX-202 was injected into mouse plasma, and both its decomposition and the formation of a conjectured IBX-200 analog was monitored. We found substantial chemical conversion after minutes of incubation into the IBX-200 analog, which we also validated to potentiate opto-PKR cell death in light (Figure S4I). Studies were performed at WuXi AppTec (China). IBX-202 and propantheline bromide (positive control) were added to CD-1 mouse plasma (BioIVT MSE00PLNHY2N) in separate wells of a 96-well plate and incubated at 37°C in a water bath. At the end of incubation, stop solution (acetonitrile containing tolbutamide and labetalol as internal standards) was added and mixed with each well, and the plate was centrifuged at 3220 *g* for 20 min. Samples were then put on Shimadzu LC-40D XD LC with a SCIEX Triple Quad 6500+ MS and CTC PAL3-RSI autosampler using an Acquity UPLC BEH C18 column and monitored for (1) the depletion of IBX-202 and formation of the corresponding IBX-200 analog or (2) the depletion of propantheline bromide.

Surface plasmon resonance

SPR was performed using a Biocore 8K+ system (Cytiva). pH scouting was performed to select appropriate buffers for each protein target. Human EIF2AK4 (GCN2 aa192-1024; MilliporeSigma 14-934) was tested in pH 4.75 buffer at a final concentration of 25 μg/mL. For binding, IBX-200, IBX-202, IBX-204, and GCN2iB (positive control) were tested at three-fold serial dilutions, with final compound concentrations decreasing from 100 μM, using the multi-cycle kinetics setting. Response curves and subsequent affinity analyses were performed using default Cytiva software settings.

Molecular docking simulations

To investigate the hypothesis that our compounds might engage different binding pockets of GCN2, we performed molecular docking simulations using AutoDock Vina and AlphaFold3's prediction of GCN2's tertiary structure.[52,53] In these simulations, we docked each of IBX-200, IBX-202, IBX-204, and GCN2iB to GCN2's predicted structure without specifying any binding site: all four compounds were predicted to adopt binding poses in the kinase subdomain around amino acids (aa) 590-600 (Figure 5C). IBX-202's binding pose suggested less interaction, consistent with the compound's predicted weaker binding affinity in SPR measurements and empirically observed inactivity in kinase inhibition measurements (Figures 5A and 5B). Additionally, IBX-200 and IBX-204 were predicted to form a hinge that engages with the same GCN2 kinase subdomain around aa900-905, whereas GCN2iB was not predicted to do so. This latter subdomain lies in the C-lobe of the kinase, which has been shown to contain amino acids implicated in catalysis, activation, and substrate recognition.[54] Notably, in these simulations IBX-200 and IBX-204 were predicted to partially bind the same kinase subdomain as GCN2iB, consistent with our kinase and SPR measurements. In contrast to GCN2iB, however, the ISR potentiation induced by treatment with IBX-200 and IBX-204 suggests that these compounds might increase, and not decrease, active forms of GCN2. Indeed, GCN2 phosphorylated at Thr899 (pGCN2 Thr899) is a canonical active form of GCN2,[55,56] and autophosphorylation occurs in the activation loop of GCN2, a process that is known to be required for, but not identical to, kinase activity.[54]

Specifically, AlphaFold 3[53] (https://alphafoldserver.com/) was used to predict the three-dimensional structure of GCN2 aa192-1024 using default settings. Compounds were then docked to this predicted structure using AutoDock Vina (ver. 1.2.0),[52] following previous work.[91] Briefly, SMILES were converted into SDF files using 'obabel' with the –gen3d flag. AutoDock Tools[108] was used to prepare the protein and compounds. mk_prepare_ligand.py and prepare_receptor were used with no additional arguments, and the bounding box coordinates of the predicted GCN2 protein structure were retrieved using PyMOL (ver. 2.5.7) to define the docking site.

The center of the active site was taken to be the center of the bounding box. Docking was performed with a default exhaustiveness of 32, which specifies the number of runs that start with a random ligand conformation, and a default n_poses of 20, which specifies the final number of ligand poses reported. All binding affinities are reported in Figure 5C. The predicted binding poses shown in Figure 5C were visualized using PyMOL. As decoys, ciprofloxacin (-7.5 kcal/mol), ISRIB (-7.7 kcal/mol), Sephin1 (-6.8 kcal/mol), and halofuginone (-6.8 kcal/mol) were used to sample ISR-inactive compounds, ISR inhibitors, and ISR activators. The docked pose and position of GCN2iB in our simulations were similar to those of GCN2iB in PDB 6N3O.[109]

Generation of GCN2 and PKR KO cell lines

Genome edits were designed to introduce insertion/deletion (indel) mutations using CRISPR-Cas9 editing. Prospective guide-RNAs targeting protospacer adjacent motifs (PAMs) within a 150 bp window downstream of the start codon of exons 1 and 3 of the human GCN2 (EIF2AK4) and PKR (EIF2AK2) genes, respectively, were designed using IDT's online gRNA design tool (https://www.idtdna.com/site/order/designtool/index/CRISPR_CUSTOM). This search for GCN2 returned only one protospacer with predicted on-target and off-target activity scores > 50:

GGAGAGCTACCCGCAACGAC. The final sgRNA of the following sequence was synthesized by IDT: mG*mG*mA* rGrArG rCrUrA rCrCrC rGrCrA rArCrG rArCrG rUrUrU rUrArG rArGrC rUrArG rArArA rUrArG rCrArA rGrUrU rArArA rArUrA rArGrG rCrUrA rGrUrC rCrGrU rUrArU rCrArA rCrUrU rGrArA rArArA rGrUrG rGrCrA rCrCrG rArGrU rCrGrG rUrGrC mU*mU*mU* rU. PKR KO gRNAs were designed as above, yielding the following crRNAs from IDT: 1: /AlTR1/rUrArArUrArCrArUrArCrCrGrUrCrArGrArArGrCrGrUrUrUrUrArGrArGrCrUrArUrGrCrU/AlTR2/; 2: /AlTR1/rArUrUrCrArGrGrArCrCrUrCrCrArCrArUrGrArUrGrUrUrUrUrArGrArGrCrUrArUrGrCrU/AlTR2/; 3:

/AlTR1/rUrCrArUrGrUrGrGrArGrGrUrCrCrUrGrArArUrUrGrUrUrUrUrArGrArGrCrUrArUrGrCrU/AlTR2/. Reconstitution, dilution and reverse-transfection of gRNA into cells were carried out according to manufacturer recommendations. Briefly, gRNA, Cas9 enzyme, and CRISPRMAX Cas9 PLUS reagent (Invitrogen CMAX00001) were combined in Opti-MEM (Gibco 31985062) to form ribonucleoprotein (RNP). RNPs were subsequently combined with CRISPRMAX transfection reagent to obtain a complete transfection mix. Cell suspensions were added to culture plates on top of transfection mix and incubated at 37°C and 5% CO_2 for 48 h before expansion and subsequent experimentation. Editing success and efficiency were determined via Sanger sequencing of genomic DNA extracted from gRNA-transfected cells. Editing efficiency was estimated via TIDE (http://shinyapps.datacurators.nl/tide/). Reduction in GCN2 and PKR levels were assessed using sandwich AlphaLISA assays via comparison to empty (no gRNA) transfection controls, as described below. As expected, indel penetrance was inversely correlated with target protein expression levels for each gRNA used. The most penetrant (lowest expressing) populations for each target gene were used for subsequent phenotypic KO comparison experiments.

Kinase panel experiments

Experiments were performed using the Promega Kinase Selectivity Profiling Systems—General Panel (V6928) kit following manufacturer instructions. Kinases were treated with the indicated compounds at the indicated concentrations, and luminescence was measured using an EnVision plate reader. For each kinase, standard curves containing 1× protein, 0.5× protein, 0.25× protein, and 0× protein were generated and used for quality control. Activity values were calculated by linear interpolation of the luminescence values from treated samples with respect to corresponding standard curve values.

Measurements of GCN2 and PKR protein level

Reduction in GCN2 and PKR levels in CRISPR KO cells was assessed using respective sandwich AlphaLISA assays (Revvity ALSU-TGCN2-A500 and ALSU-TPKR-A500), via comparison to empty (no gRNA) transfection controls. AlphaLISA signal was measured according to manufacturer-recommended settings using an EnVision plate reader. Relative activity values were calculated by linear interpolation with respect to wells with no lysate. To control for potential differences in total protein production between control and KO cells, GCN2 and PKR protein levels were normalized to the protein levels of each sample, as measured using a Bradford protein assay following the manufacturer's instructions and calculated by linear interpolation with respect to standard curves generated as recommended by the manufacturer (ThermoFisher 23246). Here, absorbance was read using a SpectraMax M5 plate reader (Molecular Devices).

Measurements of pGCN2 Thr899 protein levels

Opto-PKR cells plated in 96-well clear flat-bottom black tissue-culture-treated plates were treated with IBX-200, IBX-202, IBX-204, C16 (positive control), and DMSO (1% vehicle) at the indicated final concentrations and incubated at 37°C and 5% CO_2 for the indicated times under the indicated light settings. pGCN2 Thr899 and total GCN2 protein levels were then measured using respective sandwich AlphaLISA assays (Revvity ALSU-PGCN2-A500 and ALSU-TGCN2-A500). AlphaLISA signal was measured according to manufacturer-recommended settings using an EnVision plate reader. The normalized ratios of pGCN2 Thr899 to total GCN2 AlphaLISA signal are reported.

Please cite this article in press as: Wong et al., Optogenetics-enabled discovery of integrated stress response modulators, Cell (2025), https://doi.org/10.1016/j.cell.2025.06.024

GCN2iB pharmacologic antagonism experiments

GCN2iB and 2BAct were solubilized in DMSO and added to IBX-200- and IBX-204-treated chem-PKR cells in the presence of B/B homodimerizer for determination of effects on cell viability, as described above in "Cellular viability assay." DMSO vehicle treatment was included.

Viral plaque and proliferation assays

For viral plaque assays, Vero cells were plated and allowed to grow to 80-90% confluence in clear 6-well tissue culture plates. Viral stock solutions were titered by infecting each well of cells with 10-fold serial dilutions of the viral stock; otherwise, for compound dose-response experiments, a fixed dilution of viral stock solution, chosen to result typically in ~10-100 PFUs/well, was used across all wells. Cells were infected for 1.5 to 2 h, with shaking every 20-30 min, at 37°C with 5% CO_2. The viral supernatant was then removed and replaced with overlay media (complete growth media containing 1% methylcellulose). When applicable, compounds were added to the indicated concentrations to the overlay media in each respective well. After incubation at 37°C with 5% CO_2 for 3 days (HSV-1- and ZKV-infected cells) or 9 days (RSV-infected cells), the overlay media was aspirated, and cells were fixed and stained for 30 min using 10% paraformaldehyde and 1% crystal violet in 2% ethanol and PBS (pH 7.4). Plaques were quantified by manual counting: for HSV-1, plaques with diameter >2 mm were counted, and for ZKV and RSV, plaques with diameter >1 mm were counted. For compound dose-response experiments, PFU/mL values were fit to Hill functions to calculate IC_{50} values, as described above. For HSV-1, acyclovir treatment was used as a positive control, for which the IC_{50} value was found to be ~10 μM. For RSV, ribavirin treatment was used as a positive control, for which the IC_{50} value was found to be ~100 μM.

Mouse model of ocular herpesvirus infection

Test articles were solubilized in DMSO to 14.3 mM and stored at 4°C, protected from light. For each day of dosing, an aliquot was removed from 4°C and thawed, and a volume of PBS was added to the aliquot resulting in a 70% DMSO/30% PBS final composition (this composition was used as the vehicle). The formulation was vortexed and warmed slightly to improve solubility. Beginning 0 hours after viral inoculation (hpi) and at 24 and 48 hours thereafter, mice were treated with test article. Treatment involved manually restraining each mouse and pipetting 5 μL of freshly prepared solution directly onto the right eye. Mice were then returned to their home cage after dosing. For viral inoculation, mice were anesthetized with IP injections of ketamine/xylazine. Mice were confirmed to be asleep by toe pinch, and right eyes were scored using sterile, 26-gauge needles, with three 1 mm scratches performed in two directions to disrupt the corneal layer of each eye. Mice were inoculated with 5 μL of an HSV KOS-1 viral stock solution (5×10^7 PFU/mL stock concentration). The mice were then placed on a heating pad until they recovered from anesthesia and returned to their home cages. At 48 hpi, eye infection severity was scored daily by microscopic visual inspection using a disease scoring system where 0 = no disease and 1 = corneal cloudiness, iris visible, puffy eyelids, or white material around eye. At 72 hpi, tear films from mouse eyes were sampled using sterile, fiber-tipped swabs. Mice were manually restrained, and the right eye of each mouse was swabbed using a swiping/twisting motion to facilitate collection. Swabs were placed in complete DMEM media, and the shaft of each swab was cut off to allow closure of each sample vial. Sample vials were vortexed once, allowed to sit at room temperature for 15-30 min, and vortexed a second time before a 500 μL of the sample media was removed and decanted into a labeled tube. All sample aliquots were stored at -80°C before viral plaque titering on Vero cells, following the steps described above. As the sample aliquots were diluted at least 1:5 for infection of Vero cells, the lower limit of detection of the PFU assay for these samples was 10 PFU/mL. Samples with no visible PFUs were truncated to a value of 10 PFU/mL to reflect this lower limit of detection. Eye collection was performed after euthanasia at 72 hpi. Each right eye was aseptically excised, homogenized in 1 mL of complete DMEM, and stored at -80°C before the CXCL10/IP-10 measurements described below.

CXCL10/IP-10 measurements

A sandwich IP-10 (CXCL10) Mouse ELISA Kit (Invitrogen BMS6018) was used to measure CXCL10/IP-10 levels in eye homogenates following manufacturer instructions. Raw CXCL10/IP-10 values (pg/mL) were calculated by linear interpolation with respect to an eight-point standard curve, with all values falling within the standard curve range.

Toxicity studies

To further study their promise as drug candidates, we investigated IBX-200, IBX-202, and IBX-204 in a series of experiments measuring hemolysis, iron chelation, and genotoxicity. Hemolysis is a rare but severe side-effect of compounds that are administered via injection, especially ones that may be cytotoxic; iron chelation may suggest promiscuity; and genotoxicity is a significant liability. We found that all compounds were not hemolytic, did not chelate iron, and were not genotoxic at a final concentration of 200 μM, suggesting favorable preliminary toxicological properties (Figures S6A–S6C). Consistent with this favorable safety profile, we injected mice with each compound intraperitoneally at 50 mg/kg and performed blood AST and ALT measurements to test for *in vivo* systemic toxicity, especially against the liver. Treatment with IBX-200, IBX-202, and IBX-204 did not substantially affect AST and ALT (<40% change) compared to intraperitoneal treatment with doxorubicin at 5 mg/kg (>50% change; Figures S6D and S6E). Detailed experimental procedures are presented below.

Please cite this article in press as: Wong et al., Optogenetics-enabled discovery of integrated stress response modulators, Cell (2025), https://doi.org/10.1016/j.cell.2025.06.024

Hemolysis assay

Following previous work,[33] whole human blood containing EDTA (Innovative Research IWB1K2E) was centrifuged at 120*g* at 4°C for 5 min and resuspended in DPBS. Washing was repeated until the supernatant was clear (at least 10 times). Red blood cells were then resuspended in DPBS to a density of 5×10^8 cells/mL, and 99 μL of cells was plated into each well of a 96-well round-bottom clear plate (Corning 3788). One μL of each compound was added into each well to the indicated final concentrations, and DMSO was used as vehicle. Samples were incubated for 1 hour at 37°C without shaking, after which plates were centrifuged at 1500*g* at room temperature for 5 min to pellet cells. Next, 60 μL of the supernatant from each sample was transferred to a 96-well flat-bottom clear plate, and the optical density was read at 405 nm using a Promega GloMax plate reader to quantify the amount of soluble hemoglobin. Fractional hemolysis was determined by linearly interpolating absorbance values with respect to a positive control (10% Triton X-100) and a negative control (1% DMSO vehicle).

Iron chelation assay

Following previous work,[33] $FeSO_4$ stock solutions were prepared by adding 1.8 mL of ultrapure Milli-Q water to 5 mg $FeSO_4$. Ferrozine stock solution was prepared by adding 400 μL of ultrapure Milli-Q water to 5 mg ferrozine. Both stock solutions were diluted 100-fold in water, and 99 μL of working $FeSO_4$ solution was plated into each well of a 96-well flat-bottom clear plate. One μL of each compound or EDTA (MilliporeSigma E7889) was added into each well to the indicated final concentrations, and DMSO was used as vehicle. Wells were mixed using a pipette. After 10 min incubation at room temperature, 100 μL of working ferrozine solution was added to each well, and the plate was incubated again at room temperature for 10 min. The absorbance at 560 nm was then read using a Promega GloMax plate reader. Fractional ferrous iron chelating activity was determined by linearly interpolating absorbance values with respect to a positive control (128 μg/mL EDTA) and a negative control (1% DMSO vehicle).

Ames genotoxicity assay

Following previous work,[33] a 5041 Modified Ames ISO kit from Environmental Bio-Detection Products, Inc. was used according to the manufacturer's instructions. Briefly, *Salmonella typhimurium* TA100 was grown overnight (16 h) at 37°C with shaking at 300 rpm and treated with the provided exposure media and compound samples at the final concentrations indicated. Treatment with sodium azide was used as a positive control. Cells were added to the provided reversion solution, and each sample was aliquoted into 48 wells of 96-well plates. Plates were incubated at 37°C for 3 days, after which the number of revertant (yellow-colored) wells corresponding to each sample was counted by eye. In contrast to treatment with 5 μg/mL sodium azide, treatment with the tested compounds did not induce substantial reversion of bacterial cultures. Additionally, we verified that each test compound did not inhibit the growth of *S. typhimurium* TA100 at the concentrations tested. An overnight bacterial culture was diluted 1:10,000 in LB medium and plated using 99 μL working volumes into the wells of a 96-well flat-bottom clear plate. One μL of two-fold dilutions of each test compound in DMSO, starting from a final concentration of 100 μM, was added across wells, and plates were sealed and incubated overnight at 37°C to determine bacterial growth.

Mouse AST/ALT measurements

Mice were administered a single intraperitoneal injection with IBX-200, IBX-202, or IBX-204 at 50 mg/kg or doxorubicin hydrochloride at 5 mg/kg. Two days after injection, animals were euthanized by cervical dislocation and blood was obtained via cardiac puncture. AST and ALT levels were determined using the Alanine Transaminase Colorimetric Activity Assay Kit (Cayman 700260) or Aspartate Aminotransferase Colorimetric Activity Assay Kit (Cayman 701640) following manufacturer instructions. Absorbance was measured at 340 nm using a SpectraMax M5 plate reader.

Prior knowledge for identified compounds

IBX-200 to IBX-207 were searched for using catalog number identifiers, SMILES strings, and CAS RN numbers when available on PubChem, ChemSpider, and CAS SciFinder^n. For all compounds and across all sources, no active reported biological activity was found. In searching for chemical reactions, core structures relevant to those shown in Figure 2L in the main text were used. A relevant series of reactions (e.g., 31-344-CAS-3918455) was found indicating that the core structure relevant to IBX-202 could cyclize into core structures relevant to IBX-200 in the presence of catalysts including cellulose and sodium ethoxide.

Chemical analogs and synthesis

Compounds were procured from commercial vendors, including Specs, Vitas-M, ChemDiv, ChemBridge, Life Chemicals, and Otava, and solubilized in DMSO. All structural analogs were tested as described in "Cellular viability assay," and data for each are provided in Data S2.

QUANTIFICATION AND STATISTICAL ANALYSIS

No statistical method was used to predetermine sample sizes for the mouse experiments in this study, but our sample sizes are similar to those reported in previous publications (Boyce et al.,[16] Wong et al.,[32] Wong et al.,[33] Halford et al.,[61] and Aoki et al.[62]).

Please cite this article in press as: Wong et al., Optogenetics-enabled discovery of integrated stress response modulators, Cell (2025), https://doi.org/10.1016/j.cell.2025.06.024

We were not blinded to allocation during experiments and outcome assessment, and data collection and analysis were not performed blind to the conditions of the experiments. No data were excluded from the analyses in this study. One-sided, two-sample permutation tests for differences in mean value[101] were performed using MATLAB (Mathworks) to test the hypothesis that disease scores and HSV-1 strain KOS PFU/mL titers were different from vehicle values for mouse experiments. Exact permutation tests, in which all possible combinations were considered, were used for all comparisons.

CellPress

Supplemental figures

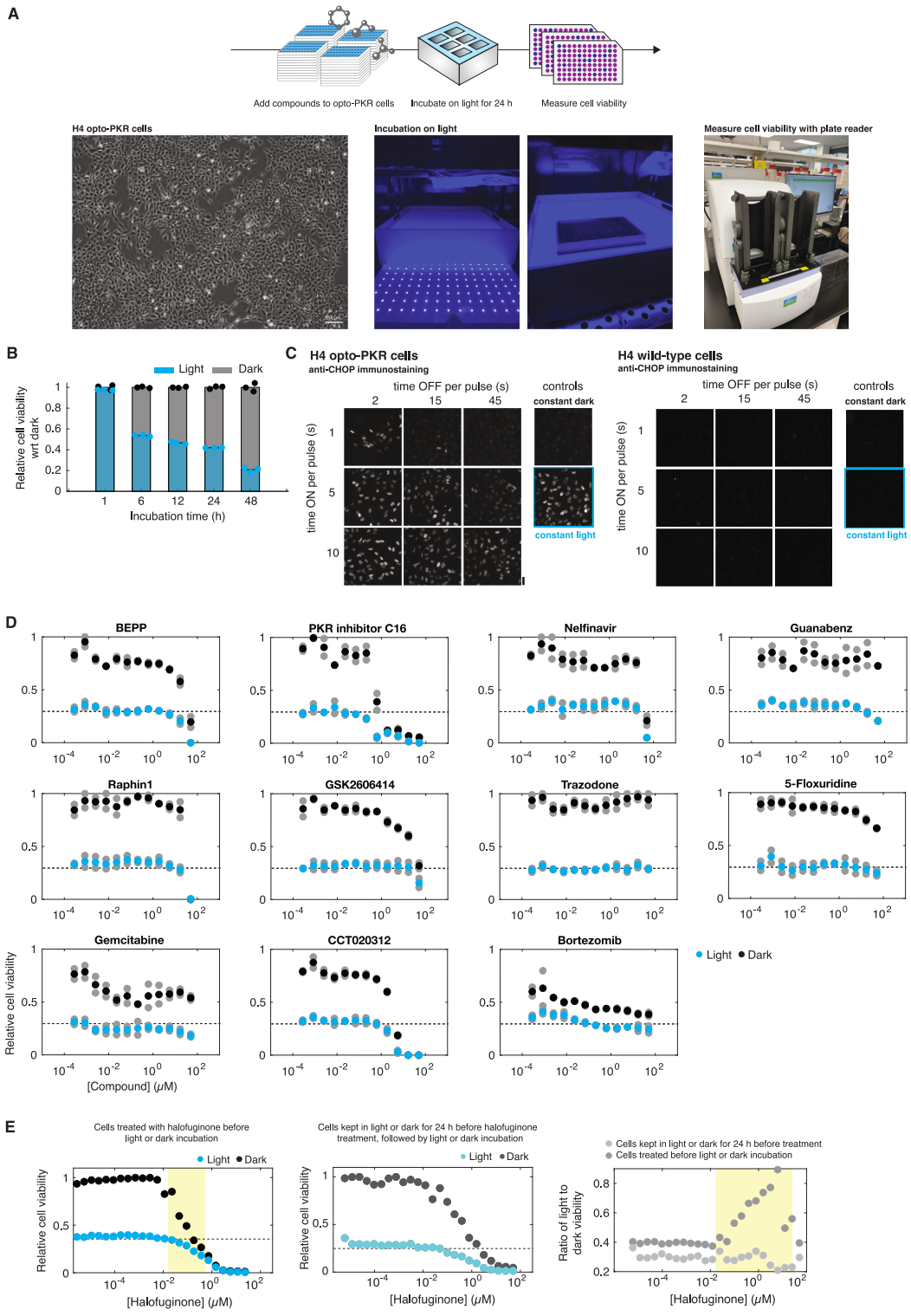

(legend on next page)

Figure S1. Dose-response viability studies and characterization of opto-PKR cells, related to Figure 1

(A) Pictorial elaboration of the screening approach combining opto-PKR cells, optogenetic illumination, and a high-throughput chemical library screen shown in Figure 1N.

(B) Cell viability measurements for opto-PKR cells incubated for different durations in the presence and absence of light (cyan and black points, respectively). Bars show means of three biological replicates in each group, and values are normalized against the mean values of cells in dark at each time point.

(C) Representative anti-CHOP fluorescence images of single opto-PKR (left) and wild-type (right) cells in response to pulsatile optogenetic illumination over 10 h. Results are representative of one biological replicate. For comparison, cells in the constant presence or absence of light (constant light and constant dark, respectively) are shown. Scale bar, 30 μm.

(D) Cell viability dose-response curves for opto-PKR cells treated with various known ISR modulators for 24 h in light and in dark (cyan and black points, respectively). Colored points represent the means of two biological replicates (gray points). Values were normalized against those of DMSO (0.5%) vehicle-treated cells in dark, and the dashed line indicates the baseline cell viability value of vehicle-treated cells in light.

(E) (Left) Similar to (D) but for treatment with halofuginone, as in Figure 1J of the main text. Points show the mean of two biological replicates. Decoupled cell viability decreases, in which cell viability decreases more in dark than in light for the same concentration of compound, are highlighted in yellow. (Center) Similar to (left) but for opto-PKR cells incubated in dark or in light for 24 h before halofuginone treatment for an additional 24 h under the same light conditions. Points show the mean of two biological replicates. (Right) Ratio of mean cell viability values for cells in light to cells in dark from the experiments shown in (left) and (center). Decoupled cell viability decreases are highlighted in yellow and are present only in cells treated with halofuginone before incubation in light or in dark; this effect was abrogated when cells were pretreated with light.

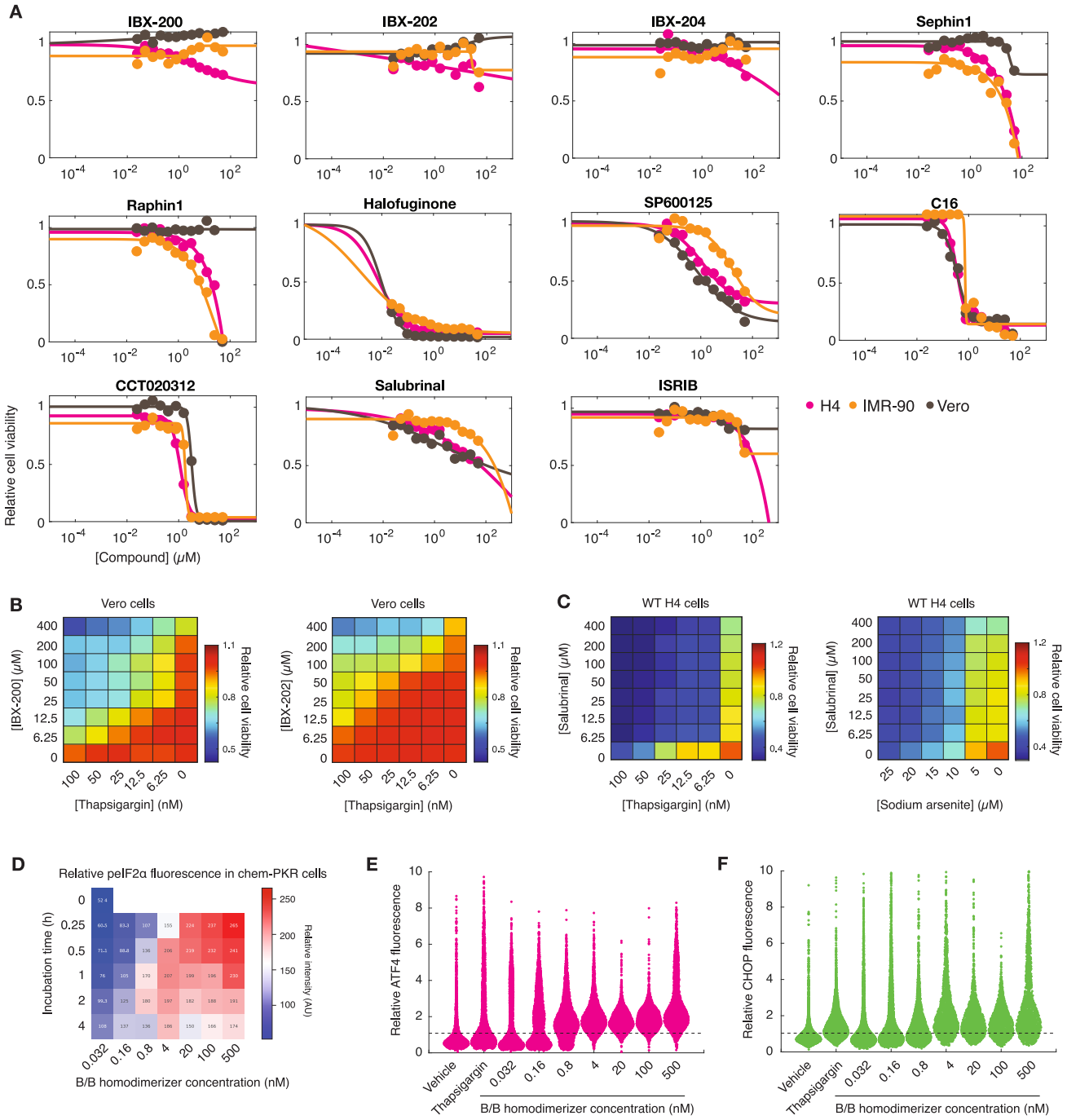

Figure S2. Cytotoxicity dose-response curves, true stressor experiments for different cell types, and characterization of chem-PKR cells, related to Figures 2 and 3

(A) Cell viability dose-response curves for various cell types treated with various compounds for 3 days in ambient lighting conditions. Colored points show values for one biological replicate. Values were normalized against those of DMSO (1%) vehicle-treated cells, and curves were generated by curve fitting.

(B) Checkerboard cell viability of Vero cells treated with IBX-200 and IBX-202, as representative compounds, in combination with thapsigargin for induction of ER stress. Cells were treated for 24 h in ambient lighting conditions. Values are normalized against those corresponding to vehicle treatment only (bottom-right value of each checkerboard). Results shown are representative of two biological replicates.

(C) Similar to (B) but for wild-type H4 cells treated with salubrinal in combination with thapsigargin and sodium arsenite.

(D) Anti-peIF2α fluorescence in chem-PKR cells in response to different durations and concentrations of B/B homodimerizer treatment. Mean fluorescence values in each condition are shown, and results are representative of two biological replicates where each condition includes at least 100 cells.

(legend continued on next page)

(E and F) Anti-ATF4 and CHOP fluorescence in chem-PKR cells in response to B/B homodimerizer treatment at various concentrations, DMSO vehicle treatment (negative control), and thapsigargin treatment (100 nM; positive control). Cells stained for ATF4 were treated for 5 h, and cells stained for CHOP were treated for 10 h. Results are representative of two biological replicates. Points indicate values for individual cells, and values are normalized to the mean value of cells treated with vehicle (dashed lines). Cell counts for each group, from left to right: ATF4, 3,147, 2,908, 3,444, 3,249, 3,079, 2,715, 2,814, 2,534, and 2,434; CHOP, 4,137, 3,588, 4,121, 3,474, 2,952, 1,656, 1,525, 1,470, and 1,745.

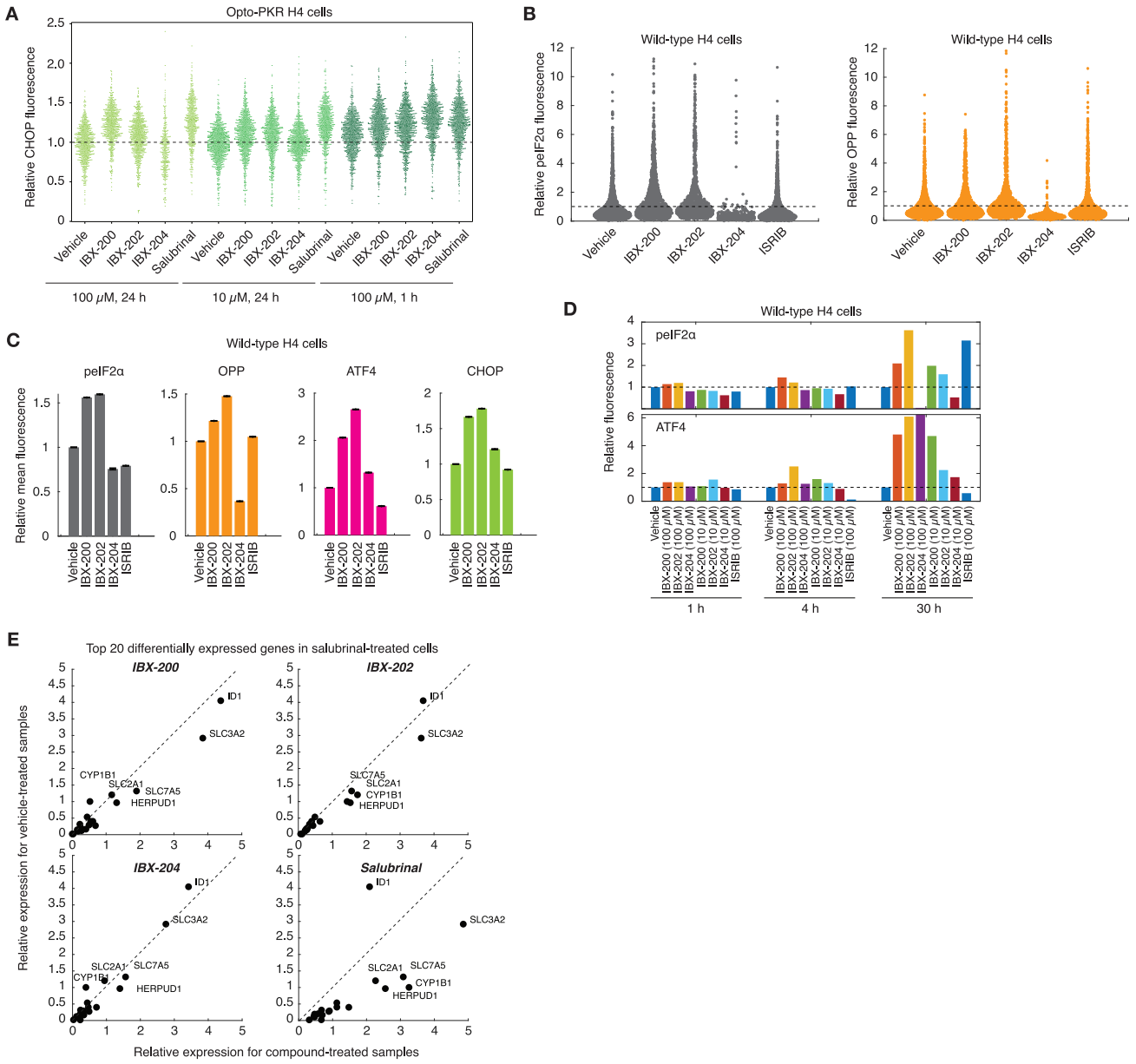

Figure S3. Phenotypic studies, related to Figure 4

(A) Anti-CHOP fluorescence in single opto-PKR H4 cells in response to compound treatment. Cells were treated with either DMSO (0.5%) vehicle or each indicated compound at the indicated concentration for the indicated treatment time and incubated in dark. Results are representative of two biological replicates. Points indicate values for individual cells, and values are normalized to the mean value of cells treated with vehicle for 24 h in the 100 μM group (dashed line). Cell counts for each group, from left to right: 735, 689, 756, 339, 559, 919, 876, 759, 814, 688, 927, 895, 963, 869, and 877.

(B) Anti-peIF2α and OPP fluorescence in the same single wild-type H4 cells, in response to compound treatment. Cells were treated with either DMSO (0.5%) vehicle or 100 μM of each indicated compound for 24 h, and results are representative of two biological replicates. Points indicate values for individual cells, and values are normalized to the mean value of cells treated with vehicle (dashed lines). Cell counts for each group, from left to right: 1,819, 1,423, 1,118, 448, and 1,661.

(C) Mean fluorescence across various stains, across single wild-type H4 cells treated with either DMSO (0.5%) vehicle or 100 μM of each indicated compound for 24 h. Results are representative of two biological replicates, and error bars indicate SEM for the cell population in one experiment. Data from (B) and Figures 4A and 4B. Note that, as wild-type H4 cells do not have optogenetically activated ISR, treatment with ISRIB results in less substantial changes to CHOP and OPP levels as compared with those shown in Figure 1.

(D) Mean anti-peIF2α and anti-ATF4 fluorescence across various time points, across single wild-type H4 cells treated with either DMSO (0.5%) vehicle or each indicated compound at the indicated concentrations. Values are normalized to the mean value of cells treated with vehicle (dashed lines). Results are representative of two biological replicates, and each bar is representative of at least 3,000 individual cells.

(E) Plots of relative mean expression for the top 20 differentially expressed genes in salubrinal-treated cells (10 μM) for 3 h in dark relative to vehicle-treated cells. For comparison, the same genes in IBX-200-, IBX-202-, and IBX-204-treated cells (10 μM of each compound) are shown. Dashed lines indicate no relative enrichment.

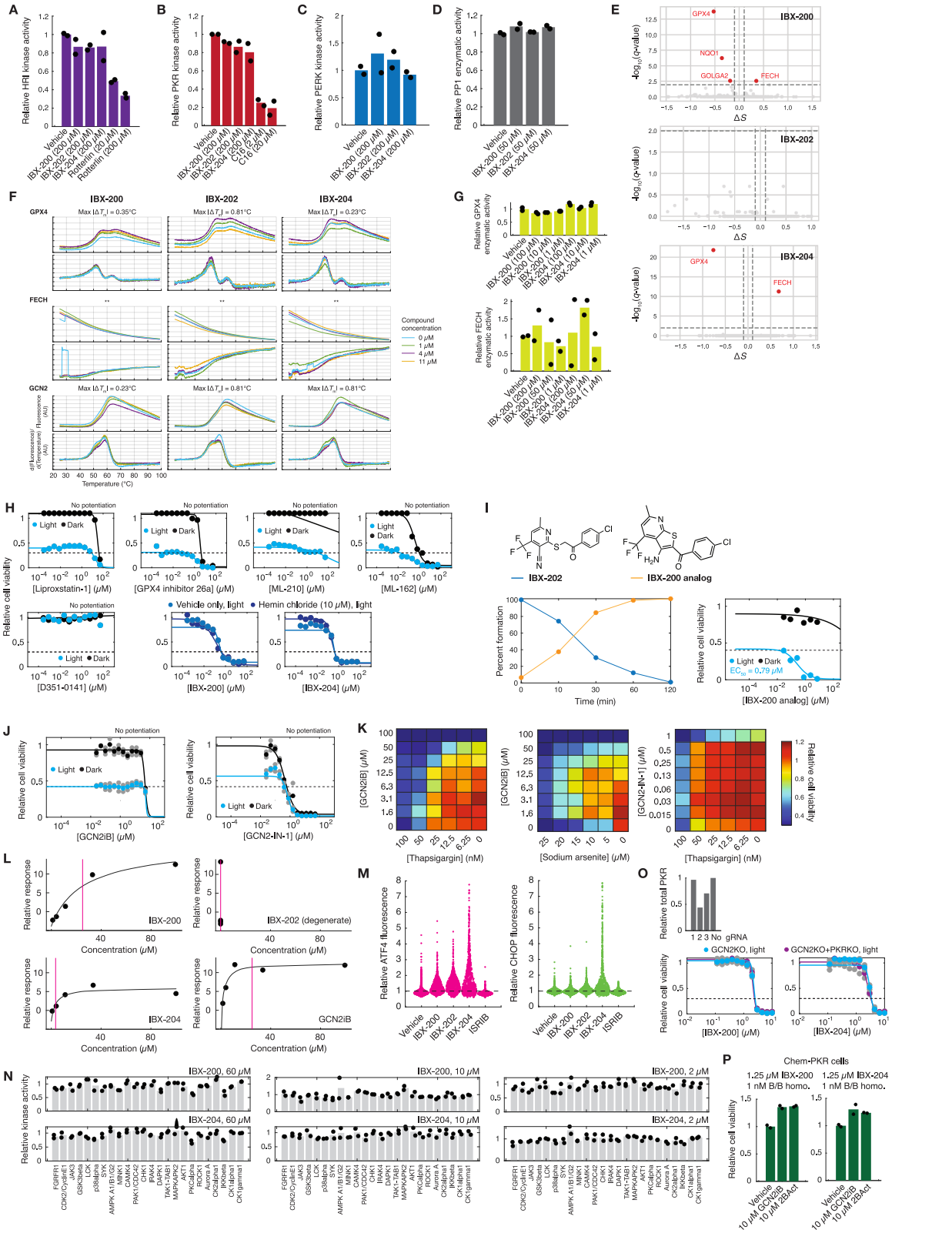

(legend on next page)

Figure S4. Mechanism of action studies, related to Figure 5

(A–D) HRI kinase (A), PKR kinase (B), PERK kinase (C), and PP1 enzymatic (D) activity of reconstituted proteins treated with each of the indicated compounds at the indicated final concentrations. Vehicle was 1% DMSO. Results are from two biological replicates (black points), and bars indicate mean values.

(E) Volcano plot of target proteins identified using CETSA selectivity profiling for IBX-200, IBX-202, and IBX-204. Apparent thermal stability shift values (ΔS) and q values from moderated t tests are shown. Potential target proteins with statistically significant changes are highlighted in red. Results are representative of one biological replicate.

(F) Differential scanning fluorimetry measurements for proteins treated with each of IBX-200, IBX-202, and IBX-204 at the indicated final concentrations. Both SYPRO orange fluorescence curves and their derivatives with temperature are shown. For each protein-ligand pair, the maximal absolute melting temperature shift across all tested compound concentrations is indicated by max $|\Delta T_m|$. Results shown are representative of one biological replicate. Asterisks indicate degenerate melting curves, and here no max $|\Delta T_m|$ values were computed.

(G) GPX4 and FECH enzymatic activity measurements for vehicle (0.5% DMSO) and compound treatment. Results show the mean (yellow bars) of two biological replicates (black points).

(H) Cell viability dose-response curves for opto-PKR cells treated with (1) GPX4 inhibitors (liproxstatin-1, GPX4 inhibitor 26a, ML-210, and ML-162) or FECH inhibitor (D351-0141) or (2) IBX-200 or IBX-204 in the presence of hemin chloride (10 μM) for 24 h in light and in dark (cyan and black points, respectively). Colored points represent one biological replicate. Values were normalized against those of DMSO (0.5%) vehicle-treated cells in dark, and the dashed line indicates the baseline cell viability value of vehicle-treated cells in light.

(I) Chemical conversion of IBX-202 into an IBX-200 analog. (Top) Chemical structures of IBX-202 and the hypothesized and measured IBX-200 analog. (Bottom left) Conversion as a function of time in mouse plasma. Results shown are the mean of two biological replicates. (Bottom right) Cell viability dose-response curves for opto-PKR cells treated with the IBX-200 analog for 24 h in light and in dark (cyan and black points, respectively). Colored points represent one biological replicate. Values were normalized against those of DMSO (0.5%) vehicle-treated cells in dark, and the dashed line indicates the baseline cell viability value of vehicle-treated cells in light.

(J) Cell viability dose-response curves for opto-PKR cells treated with GCN2iB and GCN2-IN-1 for 24 h in light and in dark (cyan and black points, respectively). Colored points represent the means of two biological replicates (gray points). Values were normalized against those of DMSO (0.5%) vehicle-treated cells in dark, and the dashed line indicates the baseline cell viability value of vehicle-treated cells in light.

(K) Checkerboard cell viability of wild-type H4 cells treated with GCN2iB and GCN2-IN-1 in combination with thapsigargin and sodium arsenite. Cells were treated for 24 h in ambient lighting conditions. Values are normalized against those corresponding to vehicle treatment only (bottom-right value of each checkerboard). Results shown are representative of two biological replicates.

(L) SPR relative response traces of GCN2 binding to each of the indicated compounds at the indicated concentrations. Values are from one biological replicate, and K_d values (vertical magenta lines) were inferred from curves of best fit (black curves).

(M) Anti-ATF4 and CHOP fluorescence in single opto-PKR GCN2-KO cells incubated in dark in response to compound treatment. Cells were treated with either DMSO (0.5%) vehicle or 100 μM of each indicated compound for 24 h, except ISRIB at 10 μM, and results are representative of two biological replicates. Points indicate values for individual cells, and values are normalized to the mean value of cells treated with vehicle (dashed lines). Cell counts for each group, from left to right: ATF4, 1,686, 1,695, 1,117, 864, and 962; CHOP, 1,560, 1,540, 1,177, 816, and 1,025.

(N) Kinase panel measurements for IBX-200 and IBX-204. The indicated kinases were treated with the indicated compounds at the indicated concentrations, and kinase activity was subsequently measured using ADP-Glo. Values are relative to those for vehicle treatment only. Gray bars indicate mean values of two biological replicates (black points).

(O) (Top) PKR protein levels in baseline (opto-PKR GCN2-KO) and opto-PKR PKR/GCN2 double-KO cells for the three different gRNAs used. Bars indicate values from one biological replicate. (Bottom) Cell viability dose-response curves for opto-PKR GCN2-KO and opto-PKR PKR/GCN2 double-KO cells treated with IBX-200 and IBX-204 for 24 h in light (cyan and purple points, respectively). Colored points indicate the means of two biological replicates (gray points). Values were normalized against the mean of DMSO (0.5%) vehicle-treated opto-PKR GCN2-KO cells in light.

(P) Measurements of cell viability of chem-PKR cells in the presence of GCN2iB and 2BAct. Chem-PKR cells were treated with the indicated compounds at the indicated concentrations and incubated for 24 h in dark. Green bars indicate the means of two biological replicates (black points). Values were normalized against the mean of DMSO (0.5%) vehicle-treated cells.

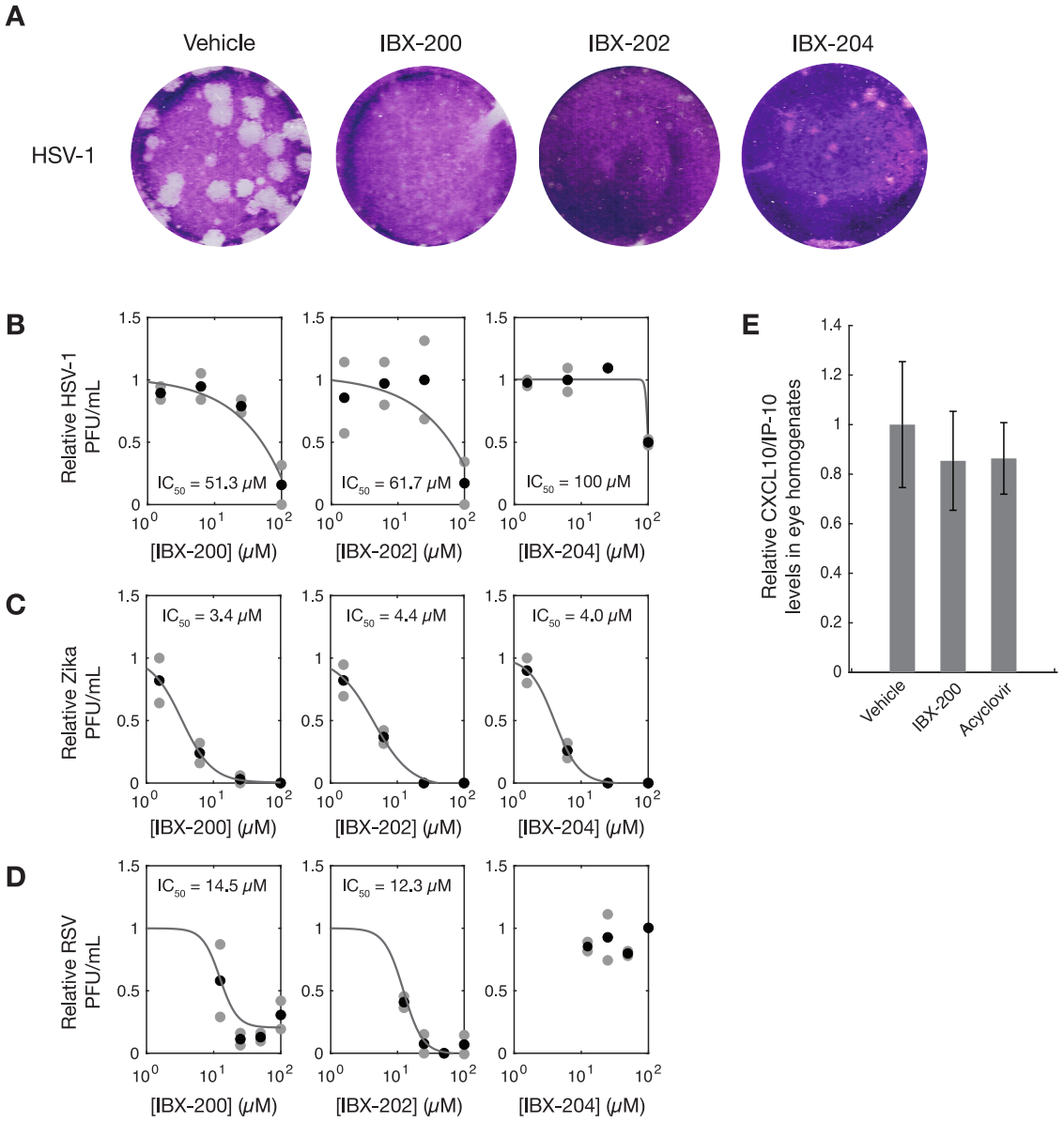

Figure S5. Antiviral studies, related to Figure 6

(A) Crystal violet staining images of cells infected with HSV-1 and treated with 0.5% DMSO vehicle, IBX-200 (100 μM), IBX-202 (100 μM), or IBX-204 (50 μM). Images are representative of two biological replicates.

(B–D) Viral titer dose-response curves for Vero cells infected with HSV-1 (B), ZKV (C), or RSV (D) and treated with varying concentrations of IBX-200, IBX-202, and IBX-204. Black points represent the means of two biological replicates, which are each shown using gray points. Values were normalized against those of DMSO (0.5%) vehicle-treated infected cells, corresponding to compound concentrations of 0 μM (points not shown on log scale). IC_{50} values were calculated by curve fitting; see STAR Methods.

(E) Measurements of eye homogenate CXCL10/IP-10 levels corresponding to the experiment shown in Figure 6B of the main text. Values were normalized against the mean for vehicle-treated mice. Bars indicate mean values for 10 mice each, and error bars indicate one standard error.

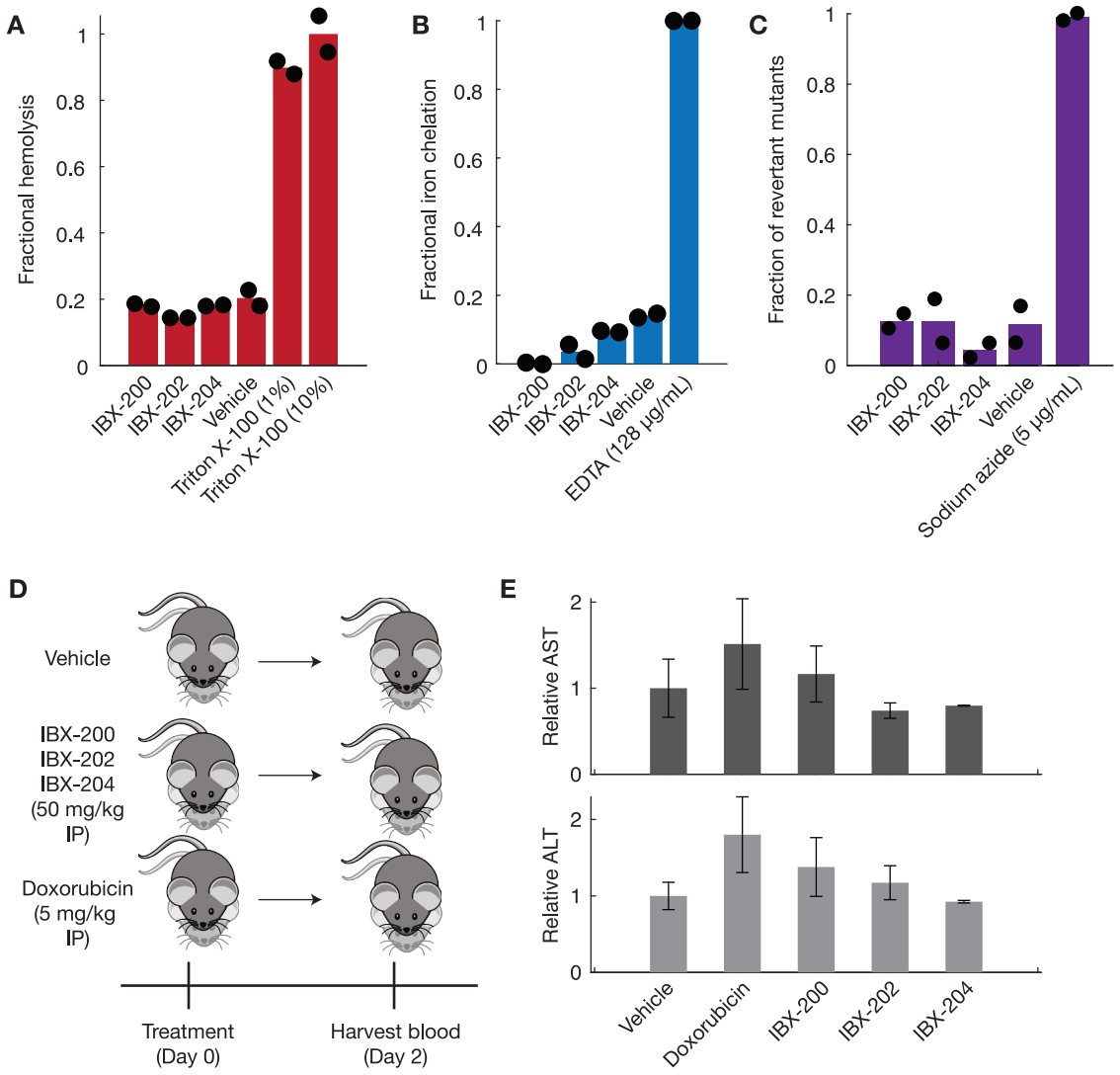

Figure S6. Toxicology studies, related to Figures 2 and 6

(A) Hemolysis measurements of human red blood cells treated with the indicated compounds. Final concentrations were 200 µM, unless otherwise indicated, and vehicle is 1% DMSO. Triton X-100 was used as a positive control. Black points indicate values from two biological replicates, and red bars indicate average values.

(B) Iron chelation measurements of ferrous iron samples treated with the indicated compounds. Final concentrations were 200 µM, unless otherwise indicated, and vehicle is 1% DMSO. EDTA was used as a positive control. Black points indicate values from two biological replicates, and blue bars indicate average values.

(C) Ames test mutagenesis measurements of the fractions of revertant *S. typhimurium* TA100 cultures treated with the indicated compounds. Final concentrations were 200 µM, unless otherwise indicated, and vehicle is 1% DMSO. Sodium azide was used as a positive control. Black points indicate values from two biological replicates, and purple bars indicate average values.

(D) Schematic of an *in vivo* study used to test AST and ALT levels in mice. Mice were intraperitoneally injected with the indicated compounds at the indicated concentrations, and blood was taken 2 days after treatment. Two mice per group were used in the study.

(E) Measurements of blood AST and ALT levels corresponding to the experiment shown in (D). Values were normalized against the mean for vehicle-treated mice. Bars indicate mean values for two mice each, and error bars indicate the full range of values.

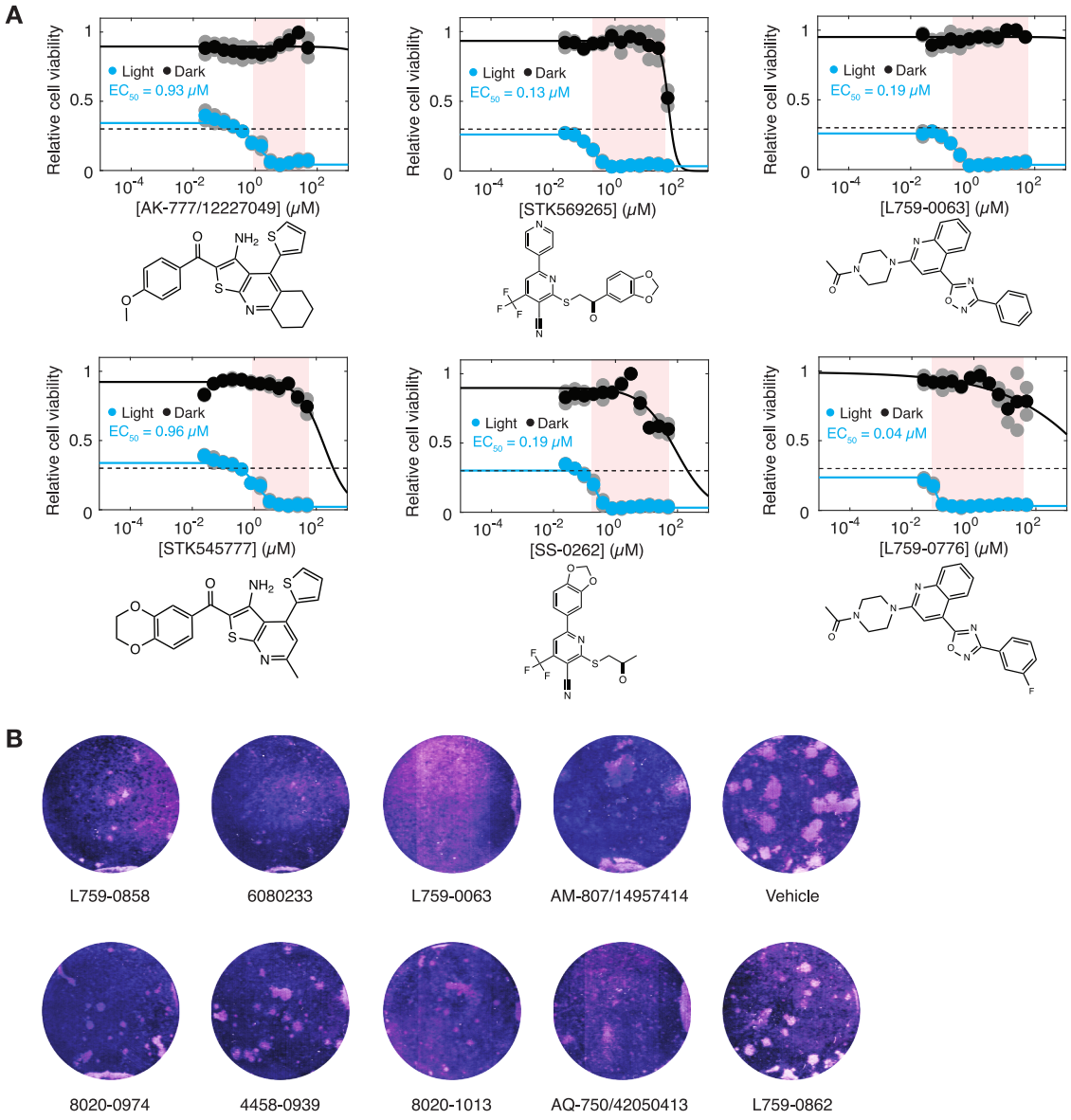

Figure S7. Dose-response viability and antiviral studies for additional SAR compounds, related to Figures 6 and 7

(A) Cell viability dose-response curves for opto-PKR cells treated with SAR analogs of IBX-200 to IBX-207 for 24 h in light and in dark (cyan and black points, respectively). Colored points represent the means of two biological replicates (gray points). Values were normalized against those of DMSO (0.5%) vehicle-treated cells in dark, and the dashed line indicates the baseline cell viability value of vehicle-treated cells in light. Decoupled cell viability decreases, in which cell viability decreases more in light than in dark for the same concentration of compound, are highlighted in red.

(B) Crystal violet staining images of Vero cells infected with HSV-1 and treated with 100 μM of the indicated compounds used to study SAR or DMSO (0.5%) vehicle (see also Data S2). Images are representative of at least one biological replicate.